DISSERTATION

MODELING AND PARAMETRIC STUDY OF END-GAS AUTOIGNITION TO ALLOW THE REALIZATION OF ULTRA-LOW EMISSIONS, HIGH-EFFICIENCY HEAVY-DUTY SPARK-IGNITED NATURAL GAS ENGINES

Submitted by

Diego Bernardi Bestel

Department of Mechanical Engineering

In partial fulfillment of the requirements

For the Degree of Doctor of Philosophy

Colorado State University

Fort Collins, Colorado

Fall 2022

Doctoral Committee:

Advisor: Bret Windom

Anthony Marchese
Daniel Olsen
Wolfgang Bangerth

Copyright by Diego Bernardi Bestel 2022

All Rights Reserved

ABSTRACT

MODELING AND PARAMETRIC STUDY OF END-GAS AUTOIGNITION TO ALLOW THE REALIZATION OF ULTRA-LOW EMISSIONS, HIGH-EFFICIENCY HEAVY-DUTY SPARK-IGNITED NATURAL GAS ENGINES

Engine knock and misfire are barriers to pathways leading to high-efficiency Spark-Ignited (SI) Natural Gas (NG) engines. The general tendency to knock is highly dependent on engine operating conditions and the fuel reactivity. The problem is further complicated by the low emission limits and the wide range of chemical reactivity in pipeline-quality natural gas. Depending on the region and the source of the natural gas, its reactivity, described by its Methane Number (MN), which is analogous to the Octane Number for liquid SI fuels, can span from 65 to 95. In order to realize diesel-like efficiencies, SI NG engines must be designed to operate at high Brake Mean Effective Pressures (BMEP), near or beyond knock limits, over a wide range of fuel reactivity. This requires a deep understanding of the combustion-engine interactions pertaining to flame propagation and End-Gas Autoignition (EGAI), i.e., the autoignition of the unburned gas (end gas) ahead of the flame front. However, EGAI, if controlled, provides an opportunity to increase SI NG engine efficiency by increasing the combustion rate and the total fraction of burned fuel, mitigating the effects of the slow flame speeds characteristic of natural gas fuels, which generally reduce BMEP and increase unburned hydrocarbon emissions. For this reason, to realize diesel-like efficiencies and ultra-low emissions on SI NG engines, this work proposes the study of the main parameters influencing the modeling and prediction of NG EGAI to allow for its control.

In this work, a novel EGAI detection and onset determination method was developed to reliably quantify EGAI for data analysis and engine control. The new method allowed the prediction of EGAI on SI NG engines without the need to use engine- and operating-condition-dependent thresholds and reduced the error in quantifying the fraction of the total energy released by the

EGAI event by up to 40%$_{pts}$. One- and three-dimensional engine models were then developed to study the engine/fuel interactions that lead to NG EGAI and its performance benefits. These models, although having decent agreement with experimental data, showed the need to account for NO_x chemistry when predicting NG EGAI due to a consistently later prediction of the EGAI onset ($\sim$1.65 crank-angle degrees) and thus, a new reduced chemical mechanism for real NG fuels was developed containing NO_x chemistry. The new reduced mechanism improved the EGAI onset prediction agreement to within $\pm$0.5 crank-angle degrees and decreased simulation time during combustion by nearly 50% when using the further reduced AREIS50NOx chemical mechanism. These models were then used to study the role of NG composition on EGAI, evaluate the engine/fuel interactions leading to NG EGAI, and perform engine optimization while leveraging EGAI to increase thermal efficiency. Piston design optimization combined with a Controlled EGAI (C-EGAI) combustion mode allowed a Heavy-Duty (HD) SI NG engine to operate at diesel-like efficiencies, i.e., Brake Thermal Efficiency (BTE) $\geq$44%. Experimental and modeling data analysis revealed that earlier and faster heat release increases combustion efficiency by an average of 1%$_{pts}$, increases work transferred to the piston resulting in a decrease in exhaust losses by 50% depending on the engine operating condition while slightly increasing heat losses. Finally, the simulation results revealed an opportunity to further enhance the BTE (up to 50%) by enabling C-EGAI combustion at leaner conditions, λ=1.4-1.6.

ACKNOWLEDGEMENTS

I could not start my acknowledgments other than by expressing my immense gratitude to the person who gave me the opportunity to one of the most life-changing experiences I've had: my Ph.D. advisor, Dr. Bret Windom. Throughout my Ph.D. program, Dr. Windom became more than an advisor; he became a mentor, someone I deeply admire professionally and personally, and a friend. His endless willingness to teach, guide, and discuss technical topics and his excitement for research have provided me with an invaluable learning experience. Dr. Windom has not only been a mentor on the technical aspect, but his positive and encouraging words always when I felt I was failing, his pieces of advice, and his support and prompt help even in personal matters have explicitly shown his excellent character and caused my deep admiration. Certainly, without him as my Ph.D. advisor, I would not have made it this far.

I also want to thank all my Powerhouse friends for sharing their time and knowledge with me. Especially, I would like to thank Miguel Valles and Siddesh Bhoite for always being willing to discuss modeling efforts and help me debug my models. I'm also thankful to have worked alongside Juan Felipe Rodriguez, whose patience in answering my endless questions and requests and his willingness to bounce off ideas gave an invaluable contribution to my research. I would like to also thank Dr. Daniel Olsen, Dr. Anthony Marchese, and Dr. Wolfgang Bangerth for their willingness to serve on my Ph.D. committee and for their insightful suggestions throughout the ARIES project.

I'm also grateful to my parents and sister, Zaqueu, Roseli and Daiana, for their constant prayers and for always supporting my decision to move out of my home country to pursue my career dreams. I know it has not been easy for them to stay so far away. Also, special thanks to the Sampsons for being a family for my wife and me in Fort Collins and for always supporting and caring for us.

And, of course, I could not be more grateful and blessed to have had the opportunity to have the love of my life, Ilara Bestel, my wife, alongside me throughout this journey. Her support,

motivation, ideas, and patience have helped me continue to pursue my dreams and ensure a future for our beautiful family. If it wasn't for her continuous encouragement, immense patience, and caring love to help me with my most stressful times, I wouldn't be able to make it to the end. "*An excellent wife who can find? She is far more precious than jewels.*" Prov. 31:10.

Finally, I praise and give thanks to God for blessing my life through these incredible people and sustaining me throughout these years. "*For from Him and through Him and to Him are all things. To Him be glory forever. Amen*." Romans 11:36.

TABLE OF CONTENTS

ABSTRACT ii
ACKNOWLEDGEMENTS iv
LIST OF TABLES viii
LIST OF FIGURES ix

Chapter 1 Introduction 1

Chapter 2 Literature Review 6
2.1 What is Natural Gas? 6
2.2 Combustion in SI Engines and End-Gas Autoignition 7
2.3 Engine Simulation and EGAI Modeling 10
2.3.1 0-D/1-D GT-Power Simulation 11
2.3.2 3-D CFD Engine Modeling 13
2.3.3 EGAI Modeling 19
2.4 Influence of NO_x Chemistry on EGAI 21
2.5 Piston Design for Increased Thermal Efficiency 22

Chapter 3 Experimental Methods 26
3.1 Cooperative Fuel Research (CFR) Engine 26
3.2 Cummins Single-Cylinder Engine 28
3.3 Rapid Compression Machine 30

Chapter 4 Detection and Quantification of EGAI in SI NG Engines 32
4.1 Experimental Setup and Operating Conditions 33
4.2 AHRR Curve Behavior under EGAI Conditions 33
4.3 EGAI Signal Description 37
4.4 EGAI Detection and Quantification Algorithm 38
4.5 Results and Discussion 40
4.6 CECL Method's Accuracy at Lower Resolutions 42
4.7 Summary 47

Chapter 5 CFR Engine Computational Modeling for NG Combustion and EGAI Investigation 50
5.1 Engine Operating Conditions 50
5.2 Computational Models 51
5.2.1 1-D Three Pressure Analysis Model 51
5.2.2 3-D CFD Model with Chemical Kinetics 52
5.2.3 3-D CFD Model with Level Set Approach 55
5.3 Modeling Results 55
5.3.1 1-D Three Pressure Analysis Model Results 55
5.3.2 3-D CONVERGE CFD Model Results 56

5.4 Discussion . . . 59
5.4.1 Comparison of the Different Modeling Approaches . . . 59
5.4.2 Natural Gas Combustion and EGAI Analysis . . . 61

Chapter 6 NO_x Chemistry Effects on End-Gas Autoignition . . . 64
6.1 Homogeneous Ignition Delay Data . . . 64
6.2 Reduced Chemical Mechanism Development . . . 66
6.3 Simulation Approach . . . 67
6.4 Results and Discussion . . . 68
6.4.1 Homogeneous Ignition Delay . . . 68
6.4.2 Sensitivity Analysis . . . 68
6.4.3 Laminar Flame Speed . . . 72
6.5 Impact on Multi-Dimensional Engine Simulations . . . 73

Chapter 7 Role of Natural Gas Composition on EGAI . . . 80
7.1 Modeling Approach . . . 80
7.2 Methane Rating Test Results . . . 81
7.3 Chemical and Thermodynamic Analysis . . . 83
7.4 Discussion and Conclusions . . . 87

Chapter 8 Piston Design Optimization to Realize Ultra-High Efficiency in SI NG Engines 88
8.1 0D/1D GT-Power Models . . . 88
8.2 Compression Ratio Optimization . . . 93
8.3 Piston Design Optimization . . . 95

Chapter 9 Controlled EGAI and Mechanisms for High Efficiency in SI NG Engines . . 99
9.1 0D/1D GT-Power Model Tuning . . . 99
9.2 C-EGAI Under a Wide Range of Operating Conditions . . . 101
9.3 Mechanisms for High Efficiencies . . . 107
9.4 Mechanisms Enabling C-EGAI . . . 112

Chapter 10 Conclusions and Future Work . . . 119
10.1 Conclusions . . . 119
10.2 Future Work . . . 122

Bibliography . . . 124

Appendix A . . . 138
A.1 Results and Discussion . . . 139

LIST OF TABLES

4.1 Tested CFR engine operating conditions. 33
4.2 NG compositions tested using the CFR Engine. 33
4.3 Tested Cummins X15 engine operating conditions. 34
4.4 NG compositions tested using the Cummins X15 Engine. 34
4.5 Error on the predicted onset of EGAI due to data coarsening for the representative cycle for each EGAI type. 47
4.6 Cycles undergoing EGAI out of the 1000 consecutive engine cycles recorded. 48

5.1 Range of Wall Temperatures used in the CFR Engine CFD Model. 58

6.1 Fuel Compositions for NO_x/HC Homogeneous Ignition Delay Modeling 65
6.2 Synthetic NO_x Compositions 65
6.3 EGR composition used in the CFD ICE simulations. 75
6.4 Simulated engine operating conditions. 76
6.5 Simulated KOCA results comparison between ARIES82 and ARIES82NOx. 78

7.1 NG and Reference Blends LFS and AI at 55 bar and 900 K 83
7.2 Experimental and 0-D Modeling KOCA and f-EGAI Results 85

8.1 Fuel composition (a) and engine operating conditions (b) used in the Cummins X15 GT-Power model calibration 91
8.2 Highest efficiency operating conditions for each EGR percentage 94
8.3 Knock-free Cases at BTE 44% or Higher 95
8.4 Cummins X15 Piston Design Optimization Results 97

9.1 Engine Control Variables' Ranges and Increments 103
9.2 Cummins X15 Engine operating conditions to trigger EGAI. 112
9.3 Minimum required end-gas Temperature and Pressure to trigger EGAI with simulated NG composition (MN=80). 114

A.1 Influence of Flow and Piston Design Parameters on ITE 143
A.2 Influence of Flow and Piston Design Parameters on Heat Flux 143
A.3 Influence of Flow and Piston Design Parameters on Ignition Delay 143
A.4 Influence of Flow and Piston Design Parameters on Burn Duration 143

LIST OF FIGURES

2.1 Premixed Flame Structure 8
2.2 Knock/EGAI Illustration 9
2.3 G-Equation Iso-Scalar Surface 17
2.4 Slope Change of Maximum KI from Yue et al. 20
2.5 Effect of NO Addition on Knock Prediction. 22
2.6 Organized in-Cylinder Flows 23
2.7 Piston Design with Reduced Squish Area 24

3.1 CFR Engine Assembly 27
3.2 Cummins SCE Pressure Measurement Locations 29
3.3 Cummins SCE cut-away 29
3.4 Cummins SCE Pistons 29
3.5 Rapid Compression Machine Setup 31

4.1 Four possible AHRR profiles depending on the presence and intensity of EGAI. AHRR profiles are from individual engine cycles 36
4.2 Comparison of EGAI Types 1 and 3. 37
4.3 LogP-LogV Diagram Illustrating EOC. 39
4.4 Comparison of EGAI Onset determined by the Third Derivative method and CECL method (Non-autoigniting and Type 1). 43
4.5 Comparison of EGAI Onset determined by the Third Derivative method and CECL method (Types 2 and 3). 44
4.6 Comparison of EGAI Onset determined by the CECL method in the Cummins X15 engine. 44
4.7 CECL method: coarser EGAI Type 1. 45
4.8 CECL method: coarser onset of EGAI points. 46
4.9 CECL method: coarser EGAI Type 2. 47
4.10 CECL method: coarser EGAI Type 3. 48

5.1 TPA Model of the CFR Engine 52
5.2 CFR Engine CFD Surface Mesh 53
5.3 Ignition Delay Comparison ARIES82 vs ARAMCO 3.0 54
5.4 TPA Model of the CFR Engine: Flow Rates Results 56
5.5 TPA Model of the CFR Engine: Combustion Results 57
5.6 TPA Model of the CFR Engine: Pressure Traces 57
5.7 Spark Modeling Comparison 59
5.8 CFR Engine CFD Modeling Results 60
5.9 CFR Engine KI versus f-EGAI 62
5.10 CFR Engine ITE versus f-EGAI 63
5.11 CFR Engine: CFD Analysis of EGAI 63

6.1 IDT Calculation Resutls 69

6.2 ARIES82NOx vs NUIG Mech1.2 Sensitivity Analysis: Promoting. 71
6.3 ARIES82NOx vs NUIG Mech1.2 Sensitivity Analysis: Inhibiting. 71
6.4 C1 vs C3 Reaction Pathway Flux Analysis. 72
6.5 ARIES82NOx Laminar Flame Speed Comparison with ARAMCO 3.0. 73
6.6 Influence of NO_x species on Laminar Flame Speeds. 74
6.7 Species Mass Fraction profiles at the Flame. 74
6.8 CFD Results with ARIES82NOx and ARIES50NOx. 77
6.9 Spatial distribution of CH_3, NO_2, NO, and OH. Highlighted locations show the onset of EGAI. 79

7.1 Methane Number Rating Test Results 82
7.2 Methane Number Rating Experimental Pressure Traces 82
7.3 Gamma Comparison Between NG and Reference Fuel 84
7.4 NG and Reference Blend CFD Results 86

8.1 0D/1D GT-Power model of the Cumming X15 Single-Cylinder engine 89
8.2 Simulated versus Experimental Fuel Flow Rates (a) and Brake Thermal Efficiency (b) for the Cummins X15 GT-Power model. 90
8.3 Simulated versus Experimental BMEP (a) and gIMEP (b) for the Cummins X15 GT-Power model. 90
8.4 Cylinder pressure and LogP-LogV diagram for a selected operating condition 92
8.5 Predicted versus experimental fuel flow rate, BMEP, and BTE. Slightly higher errors in the SITurb model, however, an excellent agreement with experimental data is still observed. 92
8.6 Calibrated induction-time correlation with ARIES82 mechanism predictions 93
8.7 Cummins X15 BTE versus CR 94
8.8 Piston designs varying squish areas to achieve various levels of turbulence and surface areas. 96
8.9 'Non-standard' piston designs to explore different bowl-to-squish region transition (left, Squish 57% Bowl) and tumble-inducing bowl (right, Squish 65% and 71% Tumble) 97

9.1 Updated Cummins X15 GT-Power Model 102
9.2 Predicted versus experimental for (a) Fuel Power and (b) Onset of EGAI. Good agreement with experimental data is again observed. Data shown contains both calibration and validation cases. 102
9.3 Predicted versus experimental for (a) nIMEP and (b) nITE. Excellent agreement with experimental data showcases the model suitability to perform studies for a wide range of operating conditions. 103
9.4 Effect of f-EGAI and EGR on BTE 105
9.5 Influence of engine control variables on f-EGAI. As expected, increasing EGR ratio, engine speed, and CA50 decreases f-EGAI. Conversely, increasing IMP increases f-EGAI 106
9.6 Influence of λ on f-EGAI. Leaning λ at constant BMEP leads to higher f-EGAI due increase IMPs. Sudden drop in f-EGAI and BTE beyond λ=1.6 is caused by misfire/poor combustion. 106

9.7 Effect of f-EGAI on Combustion Efficiency. Increase in Combustion Efficiency due to f-EGAI is significant but does not seem to be the sole mechanism responsible for the considerable increase in BTE. . . . 108
9.8 Influence of f-EGAI on the Average Heat Loss (a) and Total Energy Loss as a percentage of Fuel Energy (b). . . . 109
9.9 Influence of f-EGAI on the maximum in-cylinder Temperature (a) and Pressure (b). Increases in f-EGAI lead to higher in-cylinder temperatures and pressures. . . . 109
9.10 Effect of f-EGAI on Exhaust Losses. Exhaust Losses considerably decreases with increasing f-EGAI, indicating that work done increases with f-EGAI. . . . 110
9.11 Effect of f-EGAI on gIMEP. gIMEP, as a proxy for work done, considerably increases with increases in f-EGAI, agreeing with decrease in Exhuast Losses shown in Figure 9.10. . . . 111
9.12 Influence of f-EGAI on the crank-angle interval between 0-50% and 0-90% mass fraction burned. Sharp decrease in 0-90% interval shows that EGAI considerably decreases the second half of the combustion event. . . . 111
9.13 Unburned End-Gas Temperature (a) and Pressure (b) at the onset of EGAI. As expected, increasing EGR ratio requires higher temperatures and pressures to ignite the unburned gases. Minimum required temperature and pressure to ignite the end-gas is show in Table 9.3. . . . 113
9.14 f-EGAI shows to be sensitive to wall temperatures. A 50 K increase in the wall temperature might result in a 2.5% increase in f-EGAI. Due to reduced heat losses and increased f-EGAI, BTE is increased with wall temperatures. . . . 114
9.15 As expected, higher wall temperatures lead to higher unburned end-gas temperatures, causing an increase in f-EGAI. Legend temperatures are wall temperatures. . . . 115
9.16 S_L measured at TDC. As expected, increasing S_L causes a reduction in f-EGAI due to the reduced induction time for EGAI to take place. . . . 116
9.17 Fuel's Methane Number influence on f-EGAI. f-EGAI decreases by 0.6% for every 1 MN unit increase. More reactive NG fuels (lower MNs) result in higher BTE due to increased f-EGAI and, consequently, lower required fuel flow rates to achieve the same BMEP. . . . 117
9.18 Flow properties influence on f-EGAI. Swirl Ratio is defined as the ratio of the flow rotation speed to the Engine Speed (ω_f/ω_{engine}). Normalized Length Scale is defined as the ratio of the turbulent length scale to the engine bore diameter. . . . 118

A.1 Piston Designs for Improved ITE . . . 138
A.2 SCE CFD Model Axis Schematic . . . 139
A.3 Effects of Piston Designs on ITE: Constant CA50 . . . 140
A.4 ITE versus Heat Flux and Piston Surface Area . . . 141
A.5 Flow Parameters Effect on ITE . . . 141
A.6 Effect of Burn Duration on Heat Flux and ITE . . . 142

Chapter 1

Introduction

With increasing concern regarding green-house gas (GHG) emission and air pollution, environmental regulations have become stricter when it comes to emissions from internal combustion (IC) engines. According to [1, 2], the world's transportation fleet will be primarily powered by IC engines in the foreseeable future and will account for around 40% of energy demand by 2040 [3]. Additionally, the transportation sector is expected to increase by approximately 75%, with diesel fuel demand increasing by 85% [2]. For this reason, the study of alternative and cleaner fuels and high-efficiency IC engines is necessary to address issues such as human health problems caused by air pollution from tailpipe emissions.

In this context, Natural Gas (NG) is a compelling substitute for diesel fuel in the medium- and heavy-duty market since it offers advantages such as reduced emissions and reduced fuel costs [4]. Currently in the U.S., the cost of diesel fuel on an equivalent energy basis is approximately five times the cost of NG [4]. Additionally, lower capital and operating costs, vast domestic availability, lower particulate matter (PM) emissions, lower Carbon Dioxide (CO_2) emissions, and simpler and inexpensive aftertreatment systems offer further advantages for using NG over diesel. However, NG engines are typically less efficient than diesel engines, have less energy density, and have limited refueling infrastructure, reasons that have prevented the penetration of NG engines in the medium- and heavy-duty markets. Therefore, increasing NG engine efficiency is necessary to address some of these issues and accelerate market penetration of NG engines.

The demands of the medium- and heavy-duty markets require high-torque and high-power density outputs from their engines under a highly-transient operation, conditions at which diesel has an almost unrivaled advantage, and NG engines can struggle to achieve due to NG's slow flame speeds and long ignition delays [5] compared to diesel's. Different combustion modes using NG in IC engines have been researched in order to achieve the same levels of torque, power, and emissions. Strategies such as Stoichiometric Spark Ignited (SI), Lean Premixed SI, Lean Premixed Diesel

Pilot, and Direct Injection Diesel Pilot all offer advantages and disadvantages depending on the application. Among these, the Stoichiometric SI combustion mode seems to be the most promising for the on-road medium- and heavy-duty markets since it offers a good transient response (drivability), low PM emissions, and near-zero Nitrogen Oxides (NO_x) emissions by simply using readily available and proven Three-Way Catalyst (TWC) after-treatment systems [5]. The challenge is to achieve the same levels of Brake Mean Effective Pressure (BMEP) as in diesel engines without incurring engine knock while still maintaining high levels of thermal efficiency and low levels of emissions, especially unburned methane emissions.

SI NG engine efficiency can be enhanced by (1) increasing the compression ratio (CR) and/or boost pressure, (2) increasing charge density through the use of cooled Exhaust Gas Recirculation (EGR), and (3) enhancing the rate of combustion. Improvements in any of these parameters are challenging since they are limited by knock, misfire, and emissions. Knock, the autoignition of the unburned mixture ahead of the main propagating flame front, limits the improvements on efficiency since its occurrence is highly dependent on fuel reactivity and engine operating conditions. It is known that advanced spark timings, higher CR, and boosted intake pressures increase engine efficiency [6]; however, they also increase the tendency to knock and their tuning is limited in order to avoid unstable knocking combustion events [7]. In SI NG engines this problem is further complicated by the varying reactivity found in pipeline-quality NG, leading the same engine calibration to behave differently depending on the source of NG. To circumvent this variable reactivity, an active control, able to adapt to the varying NG reactivity, is required. An active control would not only be beneficial for the varying NG reactivity but could also allow an operation with controlled levels of knock below the damaging threshold, herein called End-Gas Autoignition (EGAI) to differ from the damaging-knocking combustion event. If this is achievable, a Controlled EGAI (C-EGAI) operation would offer an opportunity to mitigate the effects of variable NG reactivity and offer increased BMEP due to the fast combustion rates. Additionally to these benefits, a C-EGAI can potentially provide reduced UHC (including methane) emissions, since the end-gas,

near the walls and in crevice volumes, a source of Unburned Hydrocarbon (UHC) emissions, is ignited.

The main goal of this work is to investigate NG EGAI under engine relevant conditions and to understand the main variables influencing its modeling and prediction to allow for its control. This dissertation aims to answer the following research questions:

1. How does one properly detect the onset of EGAI in engine test data?
2. How does one properly predict EGAI in 1-D and 3-D engine computational models?
3. How does NO_x chemistry affect EGAI?
4. How does the change in NG composition impact EGAI and how does one properly characterize these differences?
5. How does combustion chamber design enhance burn rate, thermal efficiency, emissions, and EGAI?
6. How does a Controlled-EGAI (C-EGAI) operation perform under a wide speed-load range and what are the responsible mechanisms for increased thermal efficiency?

To answer these questions, experimental data from a Cooperative Fuel Research (CFR) engine and a Heavy-Duty (HD) Cummins X15 Diesel converted to single-cylinder SI NG operation have been used to provide data to support computational modeling. The computational models employed detailed chemical kinetics to facilitate the understanding of the underlying combustion phenomena responsible for EGAI.

The dissertation is organized as follows:

1. Chapter 2 presents a brief outlook of NG in the U.S. combined with a literature review of recent relevant work done on engine knock and EGAI, EGAI computational modeling, NO_x chemistry, and combustion chamber/piston design optimization for increased thermal efficiencies.

2. Chapter 3 presents the experimental and simulation methods utilized throughout this dissertation. In this dissertation work, data from the CFR and Cummins X15 engines were utilized for engine model development. Data from a Rapid Compression Machine (RCM) was utilized for chemical mechanism development. Models were developed using CONVERGE CFD and GT-Power software packages.

3. Chapter 4 discusses detection and quantification methods of EGAI and presents a new method to detect and quantify EGAI solely based on the Apparent Heat Release Rate (AHRR) curves.

4. Chapter 5 describes the computation modeling the CFR engine and presents a discussion of the different modeling approaches' strengths and weaknesses as well as presents the observed trends regarding EGAI combustion.

5. Chapter 6 describes the impact of NO_x on NG EGAI and how it affects the prediction of EGAI on multi-dimensional engine computational models. Chapter 6 also provides a new reduced chemical mechanism to capture real NG chemistry in the presence of NO_x species.

6. Chapter 7 focuses on the role of NG compositions on the their tendency to autoignite under the MN rating test conditions and provides a quick method to assess a fuel's propensity to autoignite based on available engine data and chemical kinetics.

7. Chapter 8 describes the optimization done on the Cummins X15 engine's combustion chamber to achieve diesel-like efficiencies when running on a C-EGAI combustion mode fueled with NG. Here, compression ratio and piston design were optimized to enable high efficiencies under NG C-EGAI combustion.

8. Chapter 9 presents a study on the C-EGAI behavior under a wide range of speed and load and a detailed analysis on the mechanisms that led to high efficiencies when operating with C-EGAI. Additionally, this chapter also provides a study on the mechanisms by which EGAI is triggered.

9. Finally, Chapter 10 presents the conclusions from this dissertation and outlines future work.

Chapter 2

Literature Review

2.1 What is Natural Gas?

Natural Gas (NG) is an odorless gaseous mixture of hydrocarbons primarily composed of methane (CH_4), ethane (C_2H_6), and propane (C_3H_8) with trace amounts of larger hydrocarbons, nitrogen (N_2), hydrogen (H_2), and carbon dioxide (CO_2). Although renewable NG is produced from landfills and livestock through anaerobic digestion, the vast majority of NG in the U.S. comes from non-renewable sources. According to the U.S. Department of Energy, NG accounts for about 30% of the energy used in the U.S., where about 40% is used for electric power production and the remaining is used for commercial and residential uses [8]. Although NG is a promising domestically available, cleaner, and low-cost fuel to replace high-cost, imported petroleum-based fuels, it only accounts for 0.14% of the fuel used by the transportation sector [9]. Limitations such as lower energy density and range, limited refueling infrastructure, and a wide range of chemical reactivity impose challenges in heavy-duty SI NG engine development and market penetration.

Among these limitations, the wide range of chemical reactivity imposes one of the most difficult challenges in designing on-road heavy-duty SI NG engines with diesel-like efficiencies due to engine knock and misfire. Natural gas chemical reactivity quality, or its tendency to knock/autoignite, is rated based on its Methane Number (MN), a measure that is analogous to the Octane Number of SI liquid fuels [10]. The MN is determined based on a similar metric to that of the ON, where an NG fuel composition is tested against a reference fuel composed of a mixture of CH_4 and H_2, where the percentage volume of CH_4 in the mixture determines its MN. Although some studies have proposed methods for the MN rating [11–13], there are still no standardized MN test procedures nor regulations setting reactivity quality standards, which results in a wider range of MN variability across the country when compared to SI liquid fuels (65-95 versus 85-95 for the ON), limiting, therefore, the maximum power density and efficiencies that can be harvested from

these engines since engines need to be designed for knock-free operation using the lowest MN, i.e. the fuel with the highest propensity to autoignite.

2.2 Combustion in SI Engines and End-Gas Autoignition

In order to have an understanding of how SI engines work and how its modeling is performed, it is important to first understand what a flame is. Formally, a flame is defined as "a self-sustaining propagation of localized combustion at subsonic velocities" [14]. This description has a couple of keywords worth highlighting:

- Self-sustaining: energy is released from chemical reactions faster than it is lost to the surroundings. This results in high gas temperatures at the flame location which, due to heat and mass transfer, heats up the gas immediately ahead of the flame to ignition temperatures, igniting it without a second energy source and leading the flame to move forward in the combustible mixture.

- Localized: due to very short chemistry timescales, combustion happens in a thin layer, which is called the inner layer and defines the flame location. This is in contrast to homogeneous combustion that happens simultaneously everywhere in the system.

Figure 2.1 [15] below illustrates a flame propagating from right to left, where two regions in the system are created: unburned region (preheat zone), with reactants, and burned region (oxidation layer) with combustion products. Note that the fuel consumption layer, the flame location, is thin and occupies only a small portion of the flow field. Additionally, S_L, which is the laminar flame speed, represents how fast unburned gases are approaching the flame normal to its surface in a laminar environment. This quantity is an important fuel property and will be utilized later in the computational models.

Under normal SI engine operation, air and fuel are mixed in the intake system and then inducted into the cylinder through the intake valves. After being mixed with the residual gases, i.e. burned gases that remained in the cylinder from the previous engine cycle, and compressed,

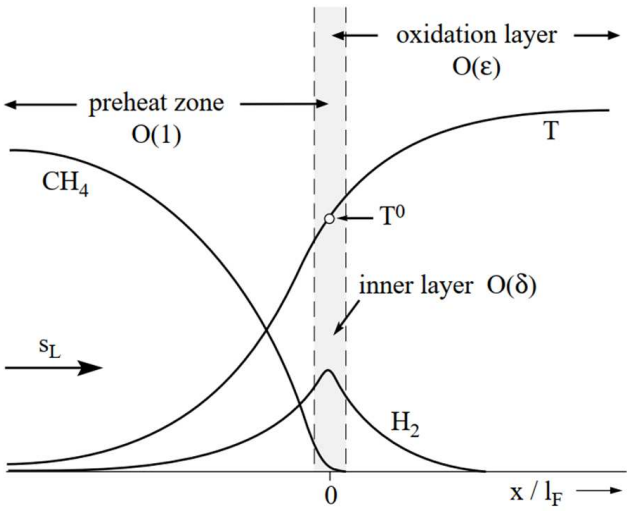

Figure 2.1: Premixed Flame Structure. Inner Layer identifies flame location. [15]

the mixture is ignited by a spark plug, initiating a flame. This flame propagates throughout the cylinder consuming all the air/fuel/residual gas mixture until it reaches the vicinity of the cylinder walls and/or piston top surface, losing more heat to the surroundings than it is releasing and thus, quenching. However, abnormal combustion, where the flame cannot steadily move across the combustion chamber, can occur, preventing this process from completely occurring. Among the various abnormal combustion events that can occur, knock is the most important abnormal combustion phenomenon [7].

According to Heywood [7], engine knock, the autoignition of the unburned (end gas) ahead of the main propagating flame front, is an undesirable abnormal combustion event in SI engines. It is undesirable since it can cause (1) damage to the engine hardware when in severe levels and (2) it is a source of noise to the vehicle operator. Knocking combustion can cause surface erosion, ring fracture, piston land cracking and fracture, and piston blow-by and seizure [16–18]. Thus, knocking combustion has been thought to be avoided to prevent damage to the engine hardware. Figure 2.2, taken from a CFD engine simulation, illustrates what happens inside the cylinder when a knocking combustion occurs.

It is well established that advanced spark timings, higher CR, higher boost pressures, and higher Exhaust Gas Recirculation (EGR) levels increase engine thermal efficiency [6, 7]. That is, if spark

timings are retarded, combustion will start too late, decreasing cylinder pressures and resulting in a reduced work transfer from the gas to the piston. Lower CRs and boost pressures have a similar effect, also affecting combustion rate and instability, heat losses, volumetric efficiencies, and propensity to knock. On the other hand, increased levels of EGR increase charge density and lower combustion temperatures by diluting the inlet mixture, increasing thermal efficiency while decreasing NO_x emissions and knock tendencies. However, high levels of EGR are limited by engine misfire [7].

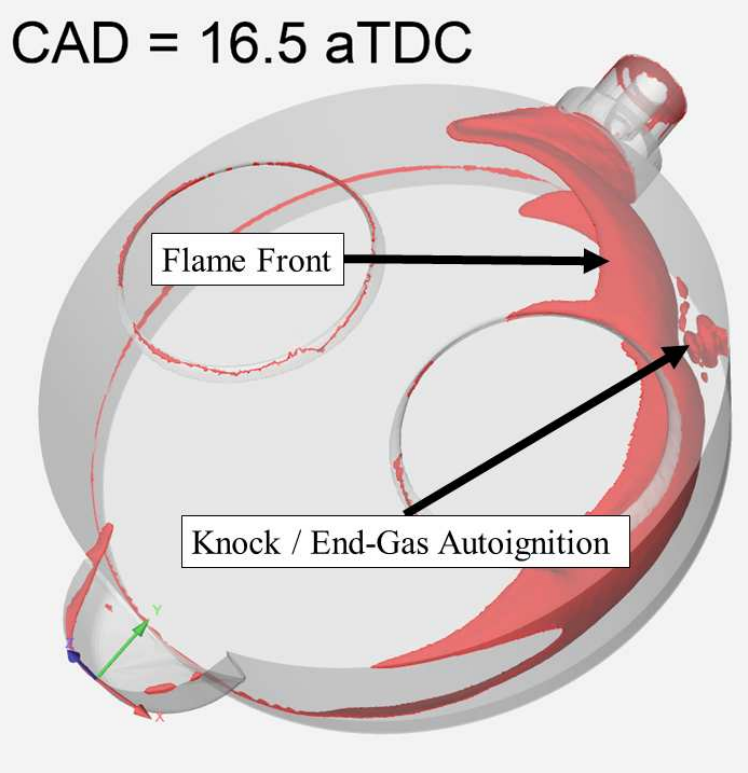

Figure 2.2: Knocking combustion event in a CFR engine CFD simulation. Larger red surface represents the main propagating flame front and smaller red surface represents the secondary flame front forming due to end-gas autoignition.

As one can see, there are limitations in increasing SI engine efficiency by optimizing any of the previously mentioned variables. On one hand, knock limits maximum cylinder pressures and, therefore, thermal efficiency and power density, while on the other, misfire limits the usable levels of EGR and/or dilution. However, if end-gas autoignition can be controlled at levels below

the damaging threshold for a given engine, it can expand the limits in the optimization variables, promoting higher gains in SI engine thermal efficiency. For this reason, Controlled End-Gas Autoignition (C-EGAI) combustion mode has been recently studied and shows promising experimental results [19–21].

In this combustion mode, controlled levels of EGAI occur at every engine cycle, increasing cylinder pressures. As a result, higher BMEPs, thermal efficiencies, and power densities are achieved compared to a pure SI operation. Particularly important for SI NG engines is the possibility of reduced UHC emissions. Since NG has slow flame speeds, a fraction of the air/fuel mixture will not be burned until the end of combustion, allowing UHC to escape to the atmosphere. EGAI mitigates the effects of slow flame speeds of NG by autoigniting the unburned air/fuel mixture that would not be burned otherwise, decreasing, therefore, UHC emissions.

The challenge with C-EGAI combustion is the timing and intensity prediction of the EGAI event for a wide variety of engine operating conditions and fuel compositions, once both factors influence its occurrence [19, 21, 22]. To this purpose, cylinder pressure feedback is critically necessary [23] once one of the most important metrics used to control EGAI in the present work is the EGAI fraction (f-EGAI) [24], which is the fraction of the total energy participating in the EGAI event. This requirement might be the most negative non-technical constraint of this approach once it can add a significant cost to the engine.

2.3 Engine Simulation and EGAI Modeling

In order to study fuel-engine interactions that lead to EGAI in SI engines, multidimensional Computational Fluid Dynamics (CFD) models are used to understand the underlying combustion phenomena to enable the optimization of the engine design parameters and develop control algorithms to expand EGAI, misfire, and emission limits. Multiple modeling approaches are available [25], such as 0-D combustion models, 1-D models, quasi-3-D, and 3-D CFD methods. In this work, modeling efforts will concentrate on 0-D/1-D GT-Power [26] models, employing two distinct approaches, and on CONVERGE CFD [27, 28] models employing detailed chemical ki-

netics and the Level Set Approach. These modeling approaches are described in the following sub-sections.

2.3.1 0-D/1-D GT-Power Simulation

GT-Power [26] is the industry-leading software for engine performance simulation. It is capable of predicting power, torque, airflow, volumetric efficiency, fuel consumption, turbocharger performance, etc. by solving the unsteady 1-D Navier-Stokes equations combined with several sub-models such as heat transfer, combustion, friction, etc. Among the various modeling approaches available in the software, the Three Pressure Analysis (TPA) and the Spark-Ignition Turbulent Flame models are the ones used in this work and thus, reviewed in this section.

The TPA model is a non-predictive modeling approach, where it cannot predict the change in burn rate behavior due to variations in engine operating parameters, but rather, it requires experimental data to calculate a crank-angle resolved burn rate on the simulation [26]. This model is useful for experimental-data assessment, boundary and initial conditions estimation for 3-D CFD models, and it is the starting point for the predictive Spark-Ignition Turbulent Flame model [21,26]. Knock Index, combustion phasing, BMEP, brake torque, brake power are some of the performance parameters possible to be analyzed using a TPA model. The main required inputs are the three crank-angle resolved pressures: intake, exhaust, and in-cylinder pressures, thus its name, and other relevant engine parameters such as EGR rate, spark timing, emissions, and fuel composition.

On the other hand, the SI Turbulent Flame model is a predictive model that can predict changes in burn rate, i.e. combustion behavior, for homogeneous charge SI engines due to variations in engine operating parameters. It is based on the works of Hires et al. [29], Blizard and Keck [30], and Morel et al. [31] and requires a fully calibrated TPA model for the proper estimation of volumetric efficiency, residual gas fraction, and burn rate. Since it uses correlations for ignition delay and energy release rates for 1-D engine modeling [29], its calibration process focuses on the tuning of four attributes:

1. Dilution Effect Multiplier (C_{DE}): takes into account the dilution effects on combustion performance.

2. Turbulent Flame Speed Multiplier (C_{TFS}): accounts for the effects of turbulence intensity on the flame propagation.

3. Taylor Length Scale Multiplier (C_{TLS}): accounts for the scale at which laminar flame propagation dominates.

4. Flame Kernel Growth Multiplier (C_{FKG}): accounts for the initial growth rate of the flame kernel.

Lastly, laminar flame speeds for each fuel are also required. GT-Power has in its library laminar flame speeds curve fitted to the equation developed by Metghalchi and Keck [32]. Natural gas flame speeds have their own curve fittings [33, 34]. Equations 2.1-2.4 are part of the SI Turbulent Flame model formulation and show the laminar flame speed equation developed by Metghalchi and Keck as well as the four adjustable attributes. For further details, the interested reader should refer to references [7, 26, 29–32].

$$S_L = (B_m + B_\phi(\phi - \phi_m)^2)\left(\frac{T_u}{T_{ref}}\right)^\alpha \left(\frac{p}{p_{ref}}\right)^\beta f(Dilution) \tag{2.1}$$

$$f(Dilution) = 1 - 0.75 * C_{DE} * (1 - (0.75 * C_{DE} * Dilution)^7) \tag{2.2}$$

$$S_T = C_{TFS} * u' * \left(1 - \frac{1}{1 + C_{FKG}\left(\frac{R_f}{L_i}\right)^2}\right) \tag{2.3}$$

$$\lambda = \frac{C_{TLS} L_i}{\sqrt{Re_t}} \tag{2.4}$$

Where

- S_L = Laminar Flame Speed
- B_m = Maximum Laminar Speed
- B_ϕ = Laminar Speed Roll-off Value

- ϕ_m = Equivalence Ratio at Maximum Speed
- T_u = Unburned Gas Temperature
- T_{ref} = Reference Temperature (298 K)
- p_{ref} = Reference Pressure (101,325 Pa)
- S_T = Turbulent Flame Speed
- u' = Turbulent Intensity
- R_f = Flame Radius
- L_i = Integral Length Scale
- Re_t = Turbulent Reynolds Number

2.3.2 3-D CFD Engine Modeling

CONVERGE [27, 28] is a general-purpose computational fluid dynamics (CFD) program capable of solving three-dimensional, compressible, chemically-reacting fluid flows in complex geometries with moving boundaries. It employs chemical kinetics solvers capable of handling chemical mechanisms with any number of species and reactions and a modified cut-cell Cartesian grid, which enables automatic mesh generation while still being able to precisely represent the true boundary shape [35].

Among other features, Adaptive Mesh Refinement (AMR) and fixed embedding are helpful features to make the mesh generation work easier. AMR automatically enables proper flame propagation calculations by refining the mesh where steep gradients of velocity and temperature are found. This feature helps mitigate under-resolved field errors, which lead to sub-grid effects and help yield better combustion results [36]. Also, the implementation of Fixed Embedding helps refine the mesh at specific locations, such as near walls or spark plug, where a finer mesh is required to properly compute the boundary layer and initial flame kernel development, respectively.

Additionally, CONVERGE features a variety of physical models, such as conjugate heat transfer, combustion, spray, emissions, etc., that helps one properly solve all physics involved in an IC engine simulation. In this review, only the most relevant equations and models to SI engine simulations will be reviewed.

Governing Equations

Conservation equation of mass, momentum, and energy describe the dynamics of fluid flow and, therefore, these equations need to be solved in an IC engine simulation. Additional equations are also necessary to describe turbulence, combustion, and the transport of properties. This section will describe the main equations being solved by CONVERGE and their assumptions. The mass and momentum conservation equations are respectively defined as:

$$\frac{\partial \rho}{\partial t} + \frac{\partial \rho u_i}{\partial x_i} = S \tag{2.5}$$

and

$$\frac{\partial \rho u_i}{\partial t} + \frac{\partial \rho u_i u_j}{\partial x_j} = -\frac{\partial P}{\partial x_i} + \frac{\partial \sigma_{ij}}{\partial x_j} + S_j \tag{2.6}$$

where the viscous stress tensor is given by

$$\sigma_{ij} = \mu \left(\frac{\partial u_i}{\partial x_j} + \frac{\partial u_j}{\partial x_i} \right) + \left(\mu' - \frac{2}{3}\mu \right) \left(\frac{\partial u_k}{\partial x_k} \delta_{ij} \right) \tag{2.7}$$

In equations 2.5 through 2.7, u is velocity, ρ is density, S is the source term, P is pressure, μ is viscosity, μ' is the dilatational viscosity, and δ_{ij} is the Kronecker delta. In the presence of a turbulence model, the viscosity is replaced by the following equation

$$\mu_{tot} = \mu_{mol} + C_\mu \rho \frac{k^2}{\epsilon} \tag{2.8}$$

Since the flow in an IC engine is compressible, an equation of state is necessary to couple density, pressure, and temperature. CONVERGE has several options such as ideal gas, Redlich-Kwong [37], Redlich-Kwong-Soave [38], and Peng-Robinson [39]. In this work, the Redlich-Kwong [37] was used and it is given by the following equation

$$P = \frac{RT}{v - b} - \frac{a}{v^2 + ubv + wb^2}, \tag{2.9}$$

where $u = 1$, $w = 0$, $b = \beta_{rk} v_c$, and $a = \alpha_{rk} \frac{p_c v_c^2}{\sqrt{T_r}}$. The additional terms with a "c" subscript define critical volume, critical temperature, and critical pressure. Alpha and beta terms represent attractive forces and volume of the molecules, respectively.

CONVERGE also solves the energy equation which is given by

$$\frac{\partial \rho e}{\partial t} + \frac{\partial u_j \rho e}{\partial x_j} = -P \frac{\partial u_j}{\partial x_j} + \sigma_{ij} \frac{\partial u_i}{\partial x_j} + \frac{\partial}{\partial x_j} \left(K \frac{\partial T}{\partial x_j} \right) + \frac{\partial}{\partial x_j} \left(\rho D \sum_m h_m \frac{\partial Y_m}{\partial x_j} \right) + S \quad (2.10)$$

where ρ is density, Y_m is the mass fraction of species m, D is the mass diffusion coefficient, S is the source term, P is the pressure, e is the specific internal energy, K is the conductivity, h_m is the species enthalpy, and T is the temperature. As can be seen in equation 2.10, there are four extra terms to be solved in the energy equation. The first term in the right-hand side (RHS) of equation 2.10 is a pressure work term that accounts for compression and expansion in a compressible flow problem. The second term in the RHS is the viscous dissipation term accounting for kinetic energy viscously dissipating into heat. The fourth term in the RHS accounts for energy transport due to species diffusion and the last term in the RHS accounts for user-specified energy sources such as a spark event.

As stated earlier, combustion is a phenomenon highly dependent on chemical reactions and mixing, where the latter implies that a turbulence model needs to properly estimate the rate of mixing of mass, momentum, energy, and species in order to have an accurate solution. Therefore, to account for the turbulence effects on the flow, Reynold-Averaged Navier-Stokes (RANS) Renormalization Group (RNG) k-ϵ turbulence model was used in this work and the interested reader is referred to Ref. [40] for more details on its formulation since it is beyond the scope of this work.

The last necessary model equations to simulate IC engines are the equations related to solving the chemistry occurring inside the cylinder. Among various available sub-models in CONVERGE for SI and Compression Ignition (CI) engines, SAGE and The Level Set approach using the G-Equation were used in this work and their formulations are presented in the next sections.

Chemical Kinetics Solver: SAGE

SAGE [41] is a detailed chemical kinetics solver that uses chemical mechanisms, which are a set of elementary reactions that describes the overall chemical reaction, to obtain the necessary system of ordinary differential equations that governs the consumption and production of species. This approach enables CONVERGE to model the combustion of any fuel under any engine operating mode.

The generalized ODE that governs the consumption or production of each species is [14]

$$\frac{d[C]}{dt} = k_{fr} \prod_i [X_i]^m - k_{rr} \prod_i [X_i]^n \tag{2.11}$$

where $\frac{d[C]}{dt}$ is the rate of change in molar concentration of species C, k_{fr} and k_{rr} are the forward and reverse rate coefficient, respectively, and X_i is the product species molar concentration. The forward rate coefficient is taken from the chemical mechanism and is defined as

$$k_{fr} = A_r T^{b_r} \exp \frac{-E_r}{R_u T} \tag{2.12}$$

and the reverse rate coefficient is defined as

$$k_{rr} = \frac{k_{fr}}{K_{cr}} \tag{2.13}$$

where

$$K_{cr} = k_{pr} \left(\frac{P_{atm}}{RT} \right)^{\sum_i \nu_{ir}} \tag{2.14}$$

$$K_{pr} = \exp \left(\frac{\Delta S_r^0}{R} - \frac{\Delta H_r^0}{RT} \right) \tag{2.15}$$

The Level Set Approach: G-Equation

Knowing that the inner layer defines the flame surface and location, one can define a non-reacting scalar G and derive an equation for it by considering an iso-scalar surface [42].

$$G(\mathbf{x}, t) = G_0 \tag{2.16}$$

As shown in Figure 2.3 [15], this iso-scalar surface divides the flow field into two regions, unburned and burned region, just as the flame does. By coinciding the location of the iso-scalar surface with the flame location and since G is a non-reacting scalar, the classical turbulent modeling can be applied and an equation for $G(\mathbf{x}, t)$ can be derived from 2.16, yielding an equation for the propagation of $G(\mathbf{x}, t)$ and, consequently, the flame propagation.

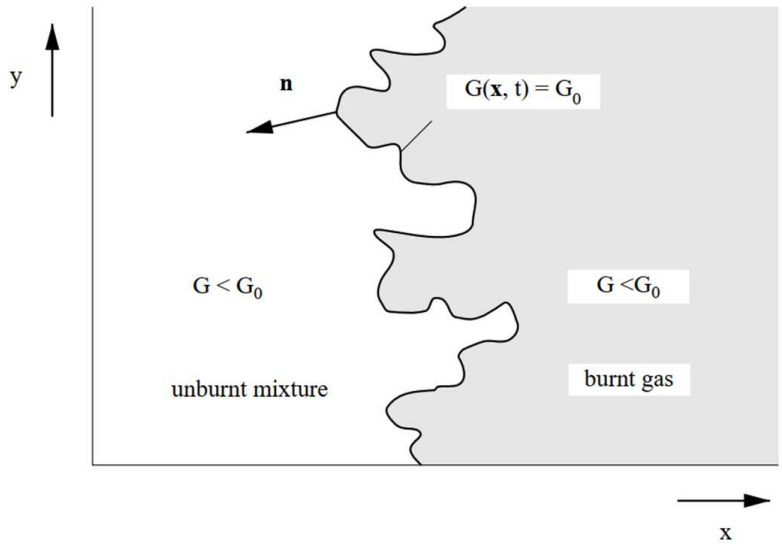

Figure 2.3: Iso-scalar surface generated by the G-Equation modeling approach. [15]

Introducing a normal vector to the flame front 2.17, a flow field propagation velocity 2.18, differentiating 2.16 with respect to time 2.19, and introducing 2.17 and 2.18 into 2.19 one obtains 2.20:

$$n = -\frac{\nabla G}{|\nabla G|} \tag{2.17}$$

$$\frac{d\mathbf{x}_f}{dt} = \mathbf{u}_f + nS_L \tag{2.18}$$

$$\frac{\partial G}{\partial t} + \nabla G \cdot \frac{d\mathbf{x}_f}{dt} = 0 \tag{2.19}$$

$$\frac{\partial G}{\partial t} + \mathbf{u}_f \cdot \nabla G = S_L |\nabla G| \tag{2.20}$$

which is the equation for the propagation of G. This is called the G-Equation in the combustion literature and is valid for the case where the inner layer length is smaller than the Kolmogorov length scale, η, since the flow is embedded in a quasi-laminar flow field.

Since a flame expands and stretches during propagation, Pelce and Clavin [43] performed two-scale asymptotic analyses, and Matalon and Matkowsky [44] derived first-order correction terms to account for small curvature and strain. The resulting expression for the laminar flame speed S_L is

$$S_L = S_L^0 - S_L^0 L\kappa - LS \tag{2.21}$$

where S_L is the laminar flame speed for the unstretched planar flame, κ the curvature, and S the strain rate. Introducing 2.21 into 2.20, the G-Equation can be written as

$$\frac{\partial G}{\partial t} + \mathbf{u}_f \cdot \nabla G = S_L^0 |\nabla G| - D_L \kappa |\nabla G| - LS|\nabla G| \tag{2.22}$$

where $D_L = S_L^0 L$.

A similar approach can be taken for the regime where the inner layer length is greater than the Kolmogorov length scale. In this case, eddies can enter the inner layer and cause unsteady perturbations, which enhances combustion by increasing mixing. The result of the formulation is the following equation for the propagation of G:

$$\frac{\partial G}{\partial t} + \mathbf{u}_f \cdot \nabla G = S_{L,s} |\nabla G| - D\kappa |\nabla G| \tag{2.23}$$

Now, in order to have an equation that is valid for both regimes of inner layer length relative to the Kolmogorov length scale, an order of magnitude analysis can be performed on the different terms of equations 2.22 and 2.23 based on combustion and turbulent flow arguments. This was done by Peters [42] and applied to a RANS context. The formulation yields the following equation for the location of the *mean* flame front

$$\bar{\rho}\frac{\partial \tilde{G}}{\partial t} + \bar{\rho}\tilde{u}_f \cdot \nabla \tilde{G} = (\bar{\rho} S_t) \left|\nabla \tilde{G}\right| - \bar{\rho} D_t \tilde{\kappa} |\nabla \tilde{G}| \tag{2.24}$$

and the variance of $\tilde{G}$, which physically is the turbulent flame brush thickness, is

$$\bar{\rho}\frac{\partial \tilde{G''^2}}{\partial t} + \bar{\rho}\tilde{u}_f \cdot \nabla \tilde{G''^2} = \nabla \cdot \left(\bar{\rho} D_t \nabla \tilde{G''^2}\right) + 2\bar{\rho} D_t \left(\nabla \tilde{G}\right)^2 - C_s \bar{\rho}\frac{\bar{\epsilon}}{\bar{k}}\tilde{G''^2} \tag{2.25}$$

The last parameter that needs to be defined is the turbulent flame speed, a quantity which is dependent on the flow field as well as on the laminar flame speed. Peters [42] derived an equation for the turbulent flame speed based on the flame surface area ratio, the ratio of the turbulent to the laminar flame surface areas, and a handful of DNS and experimental data. The resultant equation is

$$S_t = S_L + u' \left(-\frac{a_4 b_3^2}{2b_1} Da + \left[\left(\frac{a_4 b_3^2}{2b_1} Da \right)^2 + a_4 b_3^2 Da \right]^{1/2} \right) \tag{2.26}$$

where S_L is the laminar flame speed and b_1, b_3, and a_4 are modeling constants. As can be seen in equation 2.26, the laminar flame speed still needs to be supplied to the model and this is done by using correlations or a lookup table generated *before* any simulation is run.

2.3.3 EGAI Modeling

To accurately predict EGAI and its intensity, proper EGAI modeling is necessary in all the models described in the previous sections. The usual method to track end-gas chemistry is to divide the combustion chamber into two regions, burned and unburned, and solve chemical kinetics or empirically-derived induction time correlations in the unburned gas region. Figure 2.3 in the previous sub-section illustrates these regions as a flame propagates across the combustion chamber.

Recent computational work on this area has focused on multi-cycle CFD engine simulations to capture in-cylinder pressure fluctuations that are necessary to predict the knock intensity (KI) [45–47]. Pal et al. [45] were able to closely predict cycle-averaged combustion characteristics such as Peak Cylinder Pressure (PCP), crank-angle at 10% mass fraction burned (CA10), and crank-angle at 50% mass fraction burned (CA50) by running six consecutive cycles. Their work also agreed well with experimental data in terms of knock onset crank-angle (KOCA) and resonance energy. Yue et al. [47] were able to predict Knock-Limited Spark Advance by running ten consecutive

cycles and looking at the slope change point of the maximum KI across the cases (varying spark timing) as shown in Figure 2.4. Yue et al. also used a high Courant–Friedrichs–Lewy (CFL) Mach number which results in computational efficiency gain. Another work by Yue and Som [46] shows that the Livengood-Wu (L-W) integral can be used in multi-cycle simulations to predict KLSA. The L-W integral does not use detailed chemical kinetics in the end gas, but an ignition delay lookup table generated *apriori*. This method, although computationally efficient, cannot respond to changes in fuel composition.

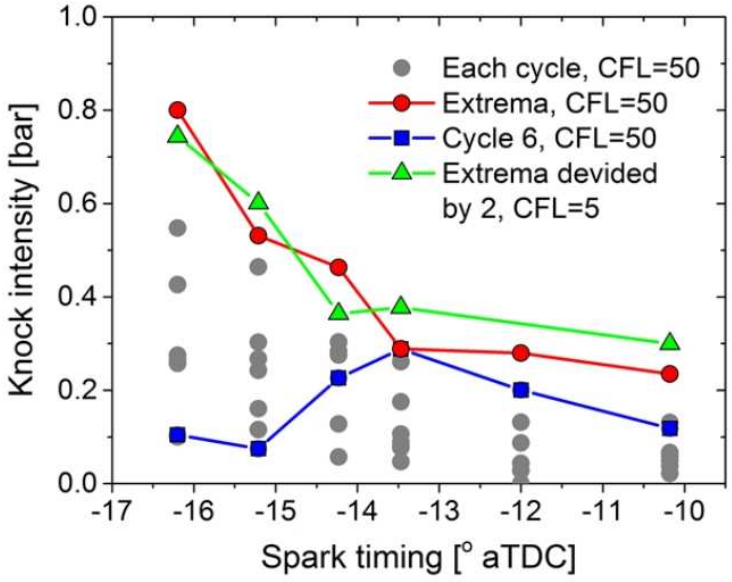

Figure 2.4: Slope change of maximum KI from Yue et al. Point of rapid increase in KI determines KLSA [47].

The negative aspects of these approaches are twofold. First, it requires multi-cycle low-CFL-Mach-number CFD simulations to capture in-cylinder pressure fluctuations and enable the calculation of KI. Yue et al. [47] showed it is possible to predict KLSA with high CFL Mach numbers; however, low CFL Mach numbers are still required for the correct prediction of KI.

Second, accurate prediction of EGAI is highly dependent on the fuel chemistry and, thus, requires accurate detailed or reduced chemical mechanisms for the fuels of interest. However, most chemical mechanisms available today lack relevant sub-mechanism such as the NO_x oxidation and

its reaction with hydrocarbons (HC). Recent works on this area [48–51] have shown NO_x chemistry to be an important sub-mechanism of HCs oxidation. Although the review of the importance of NO_x chemistry on the HC oxidation is left for the next section, it is important to highlight that its absence in most of the available mechanisms can result in late EGAI prediction [21, 22] and thus, inaccurate KI prediction.

2.4 Influence of NO_x Chemistry on EGAI

Research on the influence of NO_x (NO/NO_2) chemistry on HC oxidation has shown that NO_x plays an important role in the promotion/inhibition of HC autoignition [52–57]. Current data for n-heptane, iso-octane, ethanol, and toluene [54, 55] have shown that NO chemistry inhibits autoignition at low temperatures and concentrations. However, at medium and high temperatures and at low concentrations, autoignition is promoted, decreasing the Negative Temperature Coefficient (NTC) effect. This autoignition promotion, however, becomes weaker as NO concentrations are increased. Additionally, fundamental kinetics studies have suggested that NO_x chemistry also promotes the autoignition of smaller HC, such as CH_4 [58–61], C_2H_6 [62–65], and C_3H_8 [66]. This promotion, however, is pressure- and temperature-dependent.

Additionally to the chemical kinetics studies, there is a growing body of evidence for the importance of NO_x chemistry on SI engine simulations [67, 68]. Foong et al. [51] suggested that the addition of NO in their models significantly improved the agreement between simulations and experiments as shown in Figure 2.5, where it can be seen the onset of knock being advanced due to the presence of NO. Morganti et al. [50] have shown that NO addition in the residual-gas strongly promoted Liquefied Petroleum Gas (LPG) EGAI and that NO chemistry was necessary for their models to obtain good agreement with experimental data. Chen et al. [69] studied the effect of NO concentrations and intake charge temperatures on a CFR engine fueled with iso-octane. They found that the onset of knock varied significantly with intake charge temperature and NO concentration, where low levels of NO (<200 ppm) at low intake charge temperature (52 °C) promoted EGAI, i.e. advanced the onset of knock, but high levels of NO at low temperature suppressed

it. However, this suppressing effect became weaker with increasing intake charge temperatures, disappearing at the highest temperature of 200 °C.

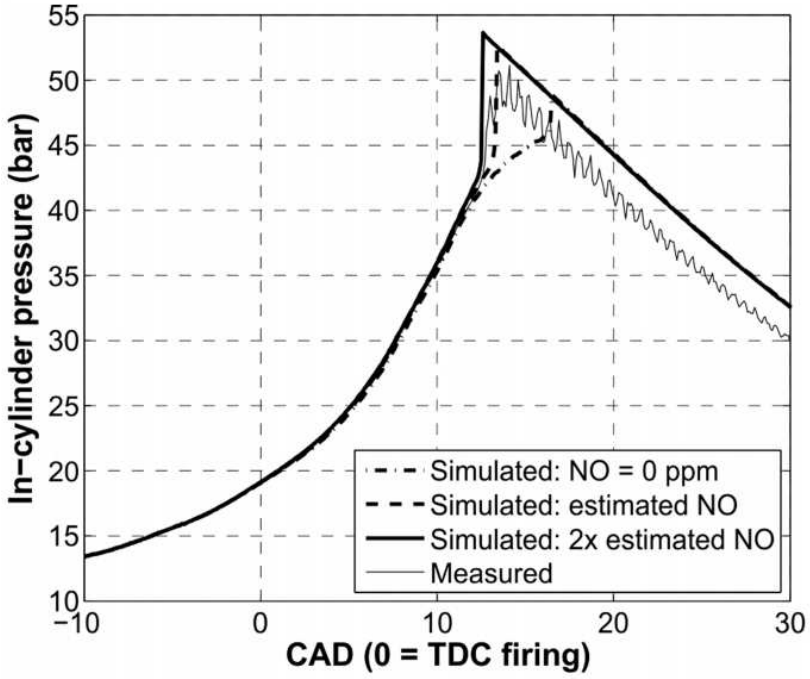

Figure 2.5: Effect of NO addition on knock prediction of SI engine 1-D simulations [51].

Lastly, Mohr et al. [48, 49] investigated the effect of NG reactivity and EGR substitution rate and composition on homogeneous ignition delay, flame speeds, and EGAI for stoichiometric NG/oxidizer/EGR blends. They observed that the addition of EGR composed of only inert species (CO_2 and Ar) suppressed homogeneous autoignition in all NG fuels tested under all conditions. However, for all NG fuels tested, increasing EGR rates with reactive species (Ar, CO_2, CO, and NO) promoted homogeneous autoignition under all conditions, thus reproducing the same trends for various NG fuel compositions that were observed in other studies and fuels.

2.5 Piston Design for Increased Thermal Efficiency

The need to increase SI NG engine thermal efficiency has led engine development efforts to focus on strategies that utilize high EGR levels and/or lean-burn strategies. These approaches gen-

erally have slower combustion rates due to the high dilution levels and NG's slow flame speeds. Therefore, since turbulence enhances the combustion rate, research needs to be done on the combustion chamber design to optimize in-cylinder turbulence in order to enhance burn rate, stability, and efficiency [7, 70, 71].

The main engine in-cylinder organized flows that breakdown and produce in-cylinder turbulence are: swirl (Figure 2.6 left), tumble (Figure 2.6 middle), and squish (Figure 2.6 right) [7, 72]. Tumble is the charge rotation about the axis parallel to the crankshaft. Swirl is the charge rotation about the axis perpendicular to the crankshaft, and squish is the charge motion generated by the squish regions, which are the volumes created by the piston crown and cylinder head as shown in the right-most illustration on Figure 2.6.

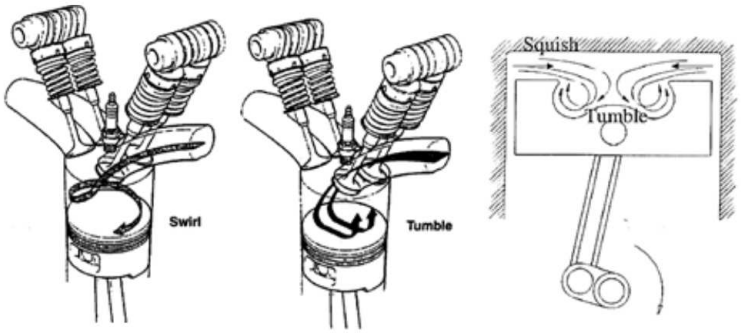

Figure 2.6: Organized in-Cylinder Flows: Swirl (left), Tumble (middle), and Squish (right) [73].

Combustion chamber optimization generally focuses on optimizing these organized flow structures in such a way that enhances in-cylinder turbulence [73]. Work on this area has shown that swirl has a remarkable effect on CA10, combustion duration, and reduced cyclic variability [72]. However, there is a swirling intensity that maximizes thermal efficiency beyond which heat losses become exacerbated, penalizing thermal efficiency [74]. Additionally, Belaire et al. [75] concluded that swirl motion combined with squish offers the best combustion rate enhancement, decreasing cyclic variability.

Tumble has also been shown to be an important player in enhancing SI combustion [71,76,77]. Urushihara et al. [78] observed in their work that tumble generated greater turbulence than swirl, and Selamet et al. [79] found that tumble also shortens combustion duration.

With a more applied approach, recent works on SI NG engine piston designs have addressed the effects of piston top contour and squish area ratios on the swirl, turbulent intensity, and combustion characteristics [70, 80–82]. Li et al. [70] analyzed six different bowl shapes effects on in-cylinder turbulence and, for the best performing piston design, found that, at high loads and lean-burn operation, the increased turbulent intensity increased Indicated Thermal Efficiency (ITE) and decreased UHC emissions while maintaining similar levels of NOx emissions. However, at low loads and lean-burn operation, it exhibited lower ITE and no improvement in emissions. On a different work, Moiz et al. [71] analyzed the impact of squish area ratios, CR, and D-EGR on an Heavy-Duty Diesel engine converted to SI NG operation. They found that, by decreasing the squish area ratio from 80% to 54% as shown in Figure 2.7, it is possible to have a 3.4% increase in ITE even though Turbulent Kinetic Energy (TKE) is reduced. This gain in ITE despite the decrease in TKE was explained based on the decreased heat losses from the piston surface.

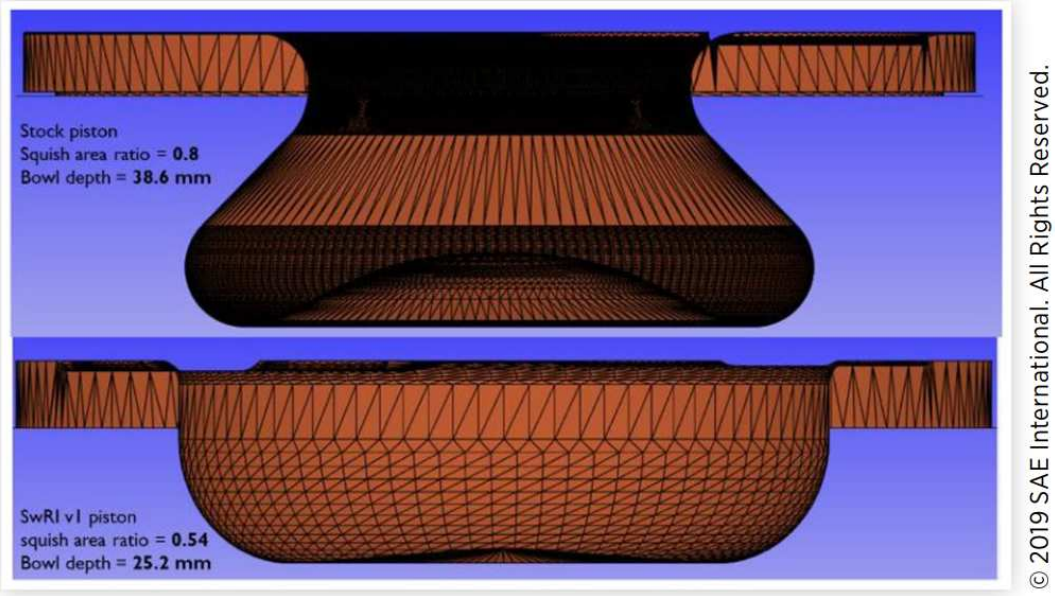

© 2019 SAE International. All Rights Reserved.

Figure 2.7: Piston design with reduced squish area as means to increase ITE [71].

Although there has been good progress on the understanding of how swirl, tumble and squish affect the turbulent intensity and combustion rate, more studies are still necessary to have a more full-picture understanding of how those flow parameters affect different combustion parameters, emissions, and heat losses, which ultimately affect thermal efficiency [72, 73]. Additionally, more research is also necessary on how tumble can affect NG SI combustion and is affected by piston design, especially in the case of retrofitted diesel engines to SI NG operation, since diesel engines are mainly swirly engines [71]. Lastly, it seems that the precise mechanisms by which thermal efficiencies are increased or decreased are not always assessed, but rather only an exposition of the results is presented.

Chapter 3

Experimental Methods

The experimental data presented in this work were collected by three other graduate students working at the Colorado State University's (CSU) Engines and Energy Conversion Laboratory (EECL) and reported in Refs. [19, 48, 49, 83]. A Cooperative Fuel Research (CFR) engine, a Cummins X15 diesel engine converted to single-cylinder SI NG operation, and a Rapid Compression Machine (RCM) were used for the data collection and their descriptions are presented in the following sections.

3.1 Cooperative Fuel Research (CFR) Engine

The CFR engine [84] is a single-cylinder, four-stroke, SI engine with a two-valve head. The engine has a stroke of 114.3 mm (4.5 in.), a bore of 82.55 mm (3.25 in.), and a displacement volume of 611.7 cm^3 (37.33 in^3). The design of the cylinder/head assembly allows the CR to be varied from 4:1 to 18:1 during engine operation by adjusting the head position relative to the crankshaft. The head has a total vertical travel of 1.235 inches, which increases or decreases the clearance volume and, thus, the compression ratio. The CFR engine available at the EECL is a 1957 F-2 model manufactured by Waukesha Engine, Dresser Industries. Figure 3.1 [84] shows a cut-away of the CFR engine highlighting its various features.

This engine has been upgraded to more accurately analyze knocking combustion. The knockmeter was removed from the detonation pickup hole, shown in Figure 3.1, and a water-cooled piezoelectric pressure transducer, Kistler model 6061A, was installed to measure crank angle resolved cylinder pressures. Additionally, intake and exhaust crank angle resolved pressures are measured using Kistler dynamic pressure sensors model 4007D and 4049B, respectively. Time-averaged intake and exhaust temperatures are measured at the same location of the pressure measurement using type K thermocouples. The engine has also been converted to run on gaseous fuels, with a blending system capable of blending up to 8 components. A digital rotary encoder

with a tenth of a degree resolution is installed on the crankshaft and used to measure crank position for crank-angle resolved data. The equivalence ratio is measured in the exhaust to verify stoichiometric operating conditions utilizing an ECM Dual-Channel AFRecorder 4800 series fast Air-Fuel Ratio Analyzer which includes inputs for H/C, O/C, and N/C ratios, improving accuracy for variable fuel composition.

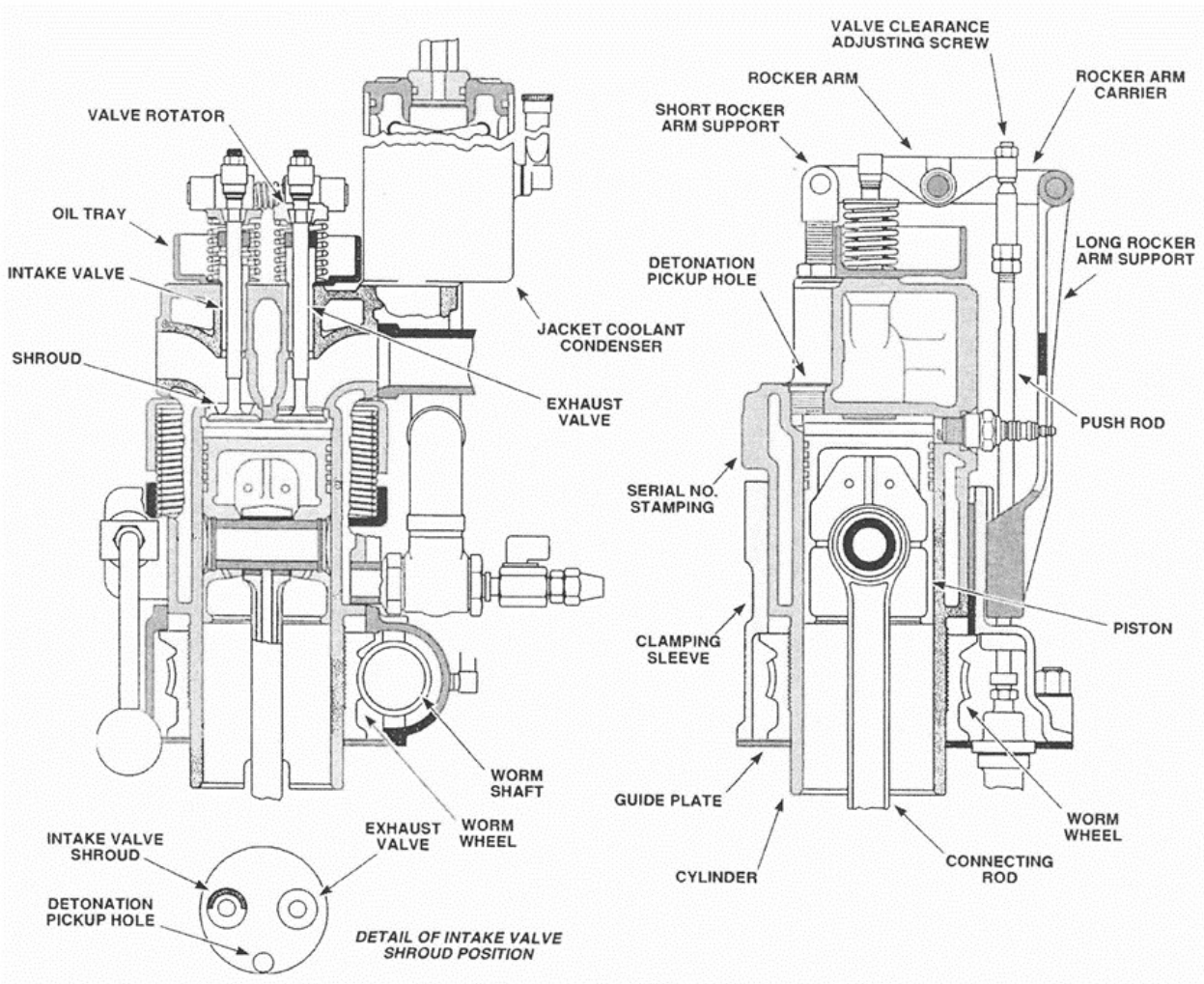

Figure 3.1: CFR Engine cut-away: cylinder/clamping sleeve assembly. [84]

The engine can be controlled using an in-house written LabVIEW program able to read inputs from all installed sensors and to provide an automated output control. The program also provides a Graphical User Interface (GUI) that displays engine variables and allows the operator to monitor

and control intake charge pressure and temperature, fuel mixture, air-fuel ratio, exhaust temperature and pressure, coolant temperature, and power level.

Additionally to the LabVIEW program, a Woodward Large Engine Control Module (LECM) was also installed on the CFR engine to explore C-EGAI strategies. The LECM is used to control gas, diesel, and dual-fuel reciprocating engines in a large variety of markets: marine propulsion, power generation, industrial, etc. It is able to control engine speed, load, air-to-fuel ratio (AFR), ignition, etc. and more importantly for this work, it offers knock and misfire detection. The LECM also offers a GUI software that allows the engine operator to visualize in real-time engine performance parameters and control them. More information on the CSU's CFR engine setup can be found in [12, 19].

3.2 Cummins Single-Cylinder Engine

The Cummins single-cylinder engine (SCE) was produced by modifying a Cummins engine production model X15 15-liter Diesel [83]. The modification consisted of removing the diesel fuel pump and filter, injectors and rails, ECM, EGR valve and cooler, EGR crossover, and turbocharger. New pistons, liner, bearings and seals, and intake and exhaust manifolds were added to the engine to allow for SI NG single-cylinder operation.

The single-cylinder operation was achieved by deactivating cylinders 1-5. For this, the deactivated cylinders had rocker levers replaced with spacers to maintain oil pressure and diesel pistons replaced with "dummy" pistons with a hole in the crown to reduce the compression work. Also, a SI NG piston bowl design replaced the original diesel piston in cylinder 6 to reduce the baseline compression ratio compared to the diesel model and allow SI NG operation. Additionally, the cylinder head and intake and exhaust manifolds were updated to allow for pressure measurements, as shown in Figure 3.2. Figure 3.3 shows a cut-away of the 3D solid model of the Cummins SCE highlighting the firing cylinder 6. Figure 3.4 shows a 3D solid model of pistons 1-5 (left) and a picture of the baseline bowl-in-piston design being used in cylinder 6. A complete description of the commissioning, modification, and setup of Cummins X15 is found in [83].

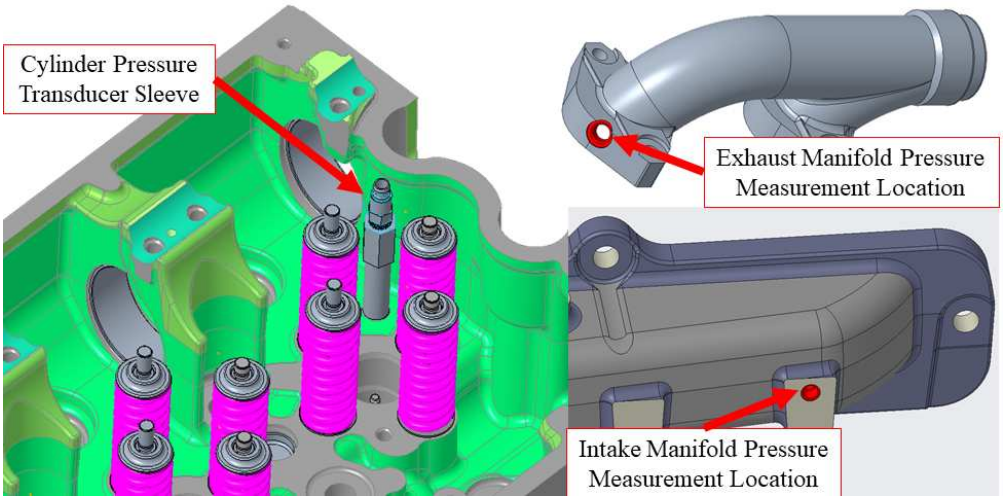

Figure 3.2: Cummins SCE Pressure Measurement Locations. Left: cylinder pressure transducer sleeve. Upper-right: exhaust manifold pressure transducer location. Lower-right: intake manifold pressure transducer location.

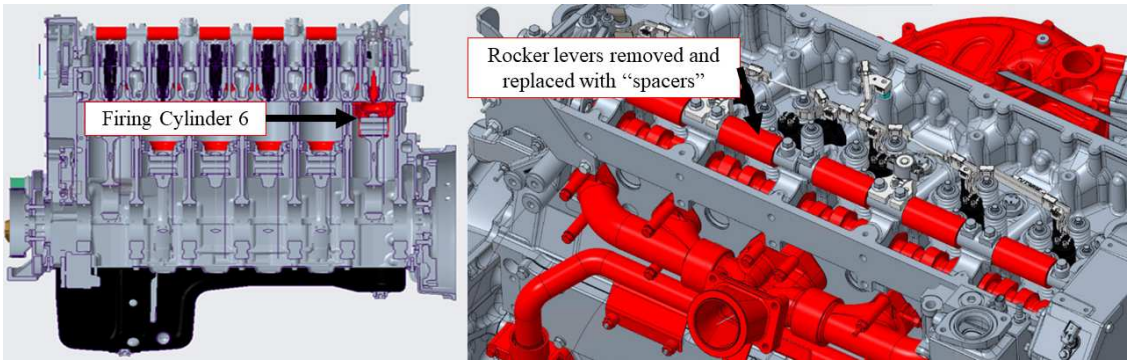

Figure 3.3: Cut-away of the Cummins SCE highlighting firing cylinder 6 (left). Illustration of rocker levers replaced with spacers (right).

Figure 3.4: Pistons used in deactivated cylinders 1-5 (left). Baseline SI-NG piston design used in firing cylinder 6 (right).

The final SCE is a 2.5-liter SI NG engine, with a bore of 137 mm and a stroke of 169 mm, and it is using similar instrumentation as the CFR engine (Section 3.1). The same pressure transducers are used for intake, exhaust, and cylinder pressure measurements as well as type K thermocouples for intake and exhaust temperatures. A Bosch LSU 4.9 UEGO Sensor is used for equivalence ratio measurements, torque is measured using a hollow aluminum coupler torque tube that measures the deformation of the strain gauge and, thus, brake torque. The engine speed is controlled by an EATON RGX Regenerative Drive VFD controller and emissions are measured using a Siemens 5-gas Analyzer. Finally, the engine can also be controlled by the in-house written LabVIEW program and the Woodward LECM. A more thorough description on the Cummins X15 engine setup and modification is found in [83].

3.3 Rapid Compression Machine

The experiments used in this work to study the influence of NO_x chemistry on end-gas autoignition were performed by Mohr and are part of his master thesis work [48]. Here a summary of the CSU's Rapid Compression Machine (RCM) experimental setup used in his experiments is presented.

The RCM is a horizontally-opposed, twin-piston, rapid compression machine manufactured by Marine Technology, LTD. This machine has a nominal compression ratio of 11.8:1 and operates on a hydraulically-locked and pneumatically-fired system. Figure 3.5, taken from Mohr's thesis [48], shows the CSU's RCM setup. The RCM, upon firing, compresses the air/fuel/EGR mixture in the combustion chamber in 15 to 20 ms and holds the pistons at TDC for the remainder of the test, maintaining a constant volume of 30 cm^3. Initial pressure and temperature are measured using MKS PDR2000 and MKS 722B13TCE2FA. Cylinder pressure is measured using a thermally-compensated high-speed pressure transducer Kistler 601CAA. Additionally, combustion chamber walls are heated using an OMEGA SRT201 heat wrap and piston position is measured using Positek Limited p100 series linear transducers. Finally, combustion temperatures are estimated using the ideal gas law and the adiabatic assumption due to the difficulty of measuring

combustion temperatures due to its rapid change. A more complete description of the CSU's RCM can be found in [24, 48].

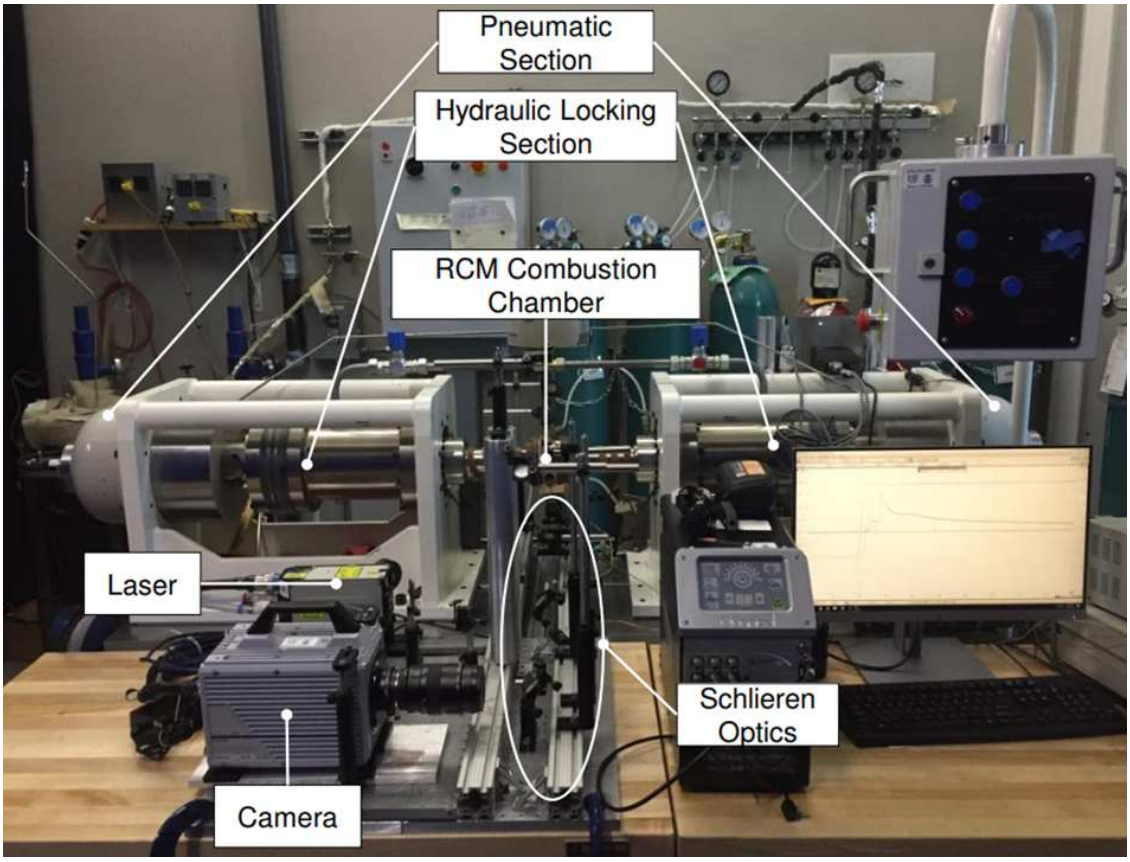

Figure 3.5: CSU's RCM complete setup [48]. For more detailed description refer to [48].

Chapter 4

Detection and Quantification of EGAI in SI NG Engines

In order to study engine/fuel interactions that lead to EGAI, one needs to first be able to detect and quantify EGAI in IC engines. Bayliff [19] showed that the current methods of detecting EGAI are appropriate to be used in SI NG engines; however, all of the methods fail to accurately capture the onset of EGAI, a crucial factor influencing the quantification of EGAI.

This chapter presents the development of an EGAI detection and onset-determination algorithm solely based on the profile of the Normalized Apparent Heat Release Rate (AHRR) curve under non-autoigniting and autoigniting operation, thus not relying on engine- and operating-condition specific thresholds. Instead, this method relies on the physics of EGAI and its expected consequences on the AHRR curve. As demonstrated in this chapter, the method was applied to two different engines under various IMEP, EGR, spark timings/CA50s, engine speed, and NG fuel compositions and can successfully detect the presence of EGAI and its onset. Additionally, the method takes less than two milliseconds to run for a single cycle on a standard workstation when using data with a resolution of 0.1 crank-angle degrees (°CA) and less than one millisecond with data of a 1.0 °CA resolution, provided cylinder pressure and AHRR are available. These runtimes might make the method suitable for use in real-time control environments. For clarity and organization, the newly developed method is referred to as the CECL method. The name was inspired by the laboratory's name where it has been developed: Chemical Energy Conversion Laboratory. This work is part of the work published as a technical paper at the SAE World Congress Experience 2022 [85].

Table 4.1: Tested CFR engine operating conditions.

Parameter	Min	Max	Unit
Compression Ratio	7.41	14.10	
Engine Speed	883	908	RPM
nIMEP	7	13	bar
BMEP	3	7	bar
Spark Timing	-22	-10	deg. aTDC
CA50	8.4	29.4	deg. aTDC
EGR	0.0%	26%	

Table 4.2: NG compositions tested using the CFR Engine. Percentages are in Mol %.

Species	Pipeline 1	Pipeline 2	Dry	Wet
CH_4	84.5%	82.4%	97.04%	84.0%
C_2H_6	10.8%	12.5%	2.80%	13.3%
C_3H_8	1.4%	1.9%	0.04%	2.5%
C_4H_{10}	0.5%	0.5%	0.01%	0.1%
C_5H_{12}	0.2%	0.1%	0.00%	0.0%
C_6H_{14}	0.1%	0.0%	0.00%	0.0%
N_2	0.6%	0.4%	0.11%	0.1%
CO_2	1.9%	2.3%	0.00%	0.0%
MN	69	72.9	87.2	69.2

4.1 Experimental Setup and Operating Conditions

The two engines that were used for this study are the standardized CFR engine and a Heavy-Duty Cummins X15 Diesel engine converted to a single-cylinder SI NG operation presented in Chapter 3. Tables 4.1, 4.2, 4.3, and 4.4 describe the operating conditions and NG compositions used for each engine.

4.2 AHRR Curve Behavior under EGAI Conditions

The work carried out in this paper is based on an extensive database of cylinder pressure measurements under non-autoigniting and autoigniting conditions and at various engine operating con-

Table 4.3: Tested Cummins X15 engine operating conditions.

Parameter	Min	Max	Unit
Compression Ratio	11.2	11.2	
Engine Speed	1195	1196	RPM
nIMEP	9.3	15.9	bar
BMEP	8.6	15.1	bar
Spark Timing	-18	-6	deg. aTDC
CA50	2.4	13.1	deg. aTDC
EGR	0.0%	10%	

Table 4.4: NG compositions tested using the Cummins X15 Engine. Percentages are in Mol %.

Species	X15 NG1	X15 NG2
CH_4	86.6%	85.2%
C_2H_6	9.8%	10.4%
C_3H_8	1.2%	1.9%
C_4H_{10}	0.2%	0.39%
C_5H_{12}	0.05%	0.1%
C_6H_{14}	0.01%	0.02%
N_2	0.47%	0.36%
CO_2	1.6%	1.69%
MN	77.6	74.9

ditions and NG compositions for two different SI NG engines. Autoignition was achieved by varying a combination of engine parameters, such as the IMEP, CA50, and CR (for the CFR engine). In general, the CFR engine needed an IMEP of at least 8 bar and a CA50 earlier than 16 °CA to autoignite under the tested conditions. The Cummins X15 was brought to the desired IMEP level using a late CA50, approximately 18-20 °CA, which was then advanced until autoignition was observed. As a result, EGAI on the Cummins X15 was observed for CA50s earlier than 11 °CA for the analyzed dataset.

With this extensive database of cylinder pressure measurements, a large database of normalized AHRR curves was obtained by calculating the AHRR using equation 4.1 [7] and normalizing it based on its peak value. In equation 4.1, V is the cylinder volume, P cylinder pressure, θ the crank angle, and γ the ratio of specific heats. These normalized AHRR curves were then studied for non-autoigniting and various intensities of EGAI conditions. In this AHRR database, it was observed that the AHRR could take one of the following profiles, regardless of the MN , but depending on the presence of EGAI and/or its intensity, shown in Figure 4.1.

$$AHRR = \frac{\gamma}{\gamma - 1} P \frac{dV}{d\theta} + \frac{1}{\gamma - 1} V \frac{dP}{d\theta} \tag{4.1}$$

The first possible AHRR profile is for a non-autoigniting operating condition, shown in the upper-left plot of Figure 4.1. In this condition, the AHRR curve will have a Gaussian-resembling profile, marked by only a positive slope before its maximum and only a negative slope after its maximum. The second possible profile is shown in the upper-right plot of Figure 4.1. It is named, for the sake of clarity and organization, "EGAI Type 1." This AHRR profile usually, but not necessarily, occurs during light to medium EGAI events and is marked by a local minimum point after its maximum, differing from the non-autoigniting profile that featured only a negative slope after its maximum. The "EGAI Type 2" shown in the lower-left plot of Figure 4.1 usually occurs in medium to heavy EGAI events and is marked by a local minimum point before its maximum. Here again, the local minimum point differs the autoigniting from the non-autoigniting AHRR profile. The last possible AHRR profile observed in this study is shown in the lower-right plot of Figure

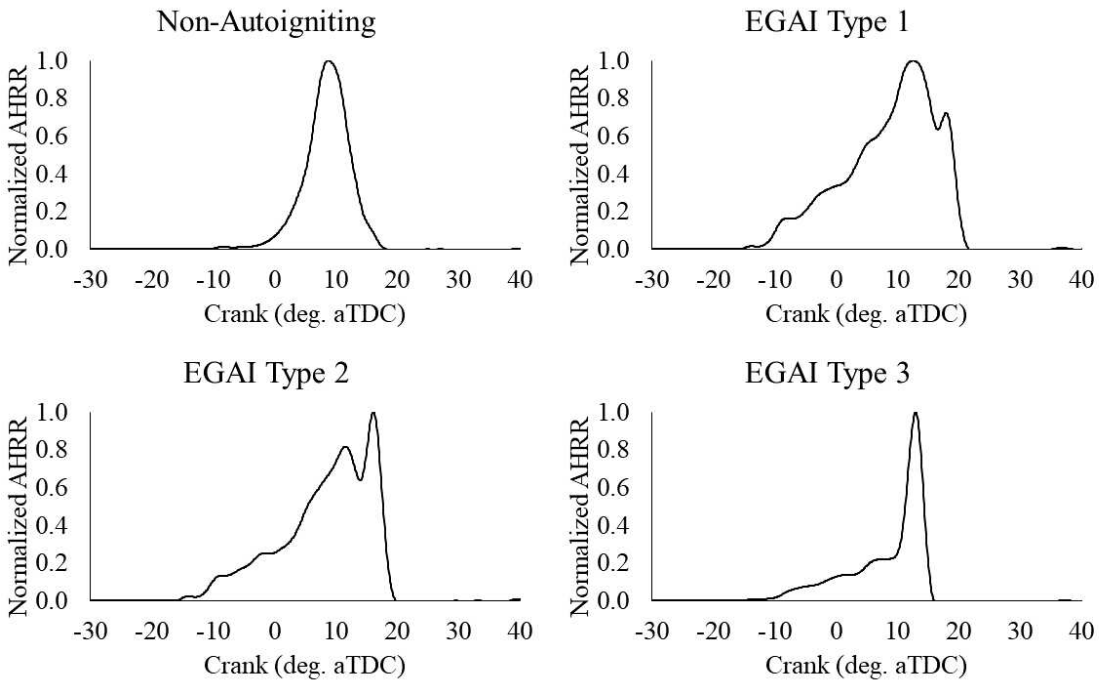

Figure 4.1: Four possible AHRR profiles depending on the presence and intensity of EGAI. AHRR profiles are from individual engine cycles.

4.1. This profile usually occurs in heavy EGAI events and is characterized by a rapid increase in the AHRR slope before its maximum.

Although both non-autoigniting and "EGAI Type 3" have only a positive slope before their maximums, their rates of change of slope are very different. For the non-autoigniting condition, the AHRR slope between TDC and its maximum is overall constant and positive, whereas the "EGAI Type 3" slope suffers a sudden and rapid increase at the onset of EGAI. The constancy of the slopes is verified by the second derivative, the rate of change in slope, that are nearly zero between TDC and the point of maximum AHRR. Figure 4.2 shows a comparison of the slopes (first derivative) and the rate of change of slopes (second derivative) of the AHRR curve for a non-autoigniting and an "EGAI Type 3" condition. As can be seen, the slope of the non-autoigniting condition before its maximum is nearly constant and positive with a nearly zero second derivative, justifying the ability to detect "EGAI Type 3" by finding where the AHRR leaves this behavior and undergoes a rapid increase in slope (rapid increase in the second derivative). This observation is consistent with the expected physical and chemical behavior of an EGAI event where the volumetric autoignition

causes a very rapid heat release event, which, in the context of an SI NG engine, shows up as a steep increase in the slope of the AHRR curve. A similar argument can be made for the other two AHRR profiles, which explains the increase in AHRR after it peaked and the appearance of a local minimum point.

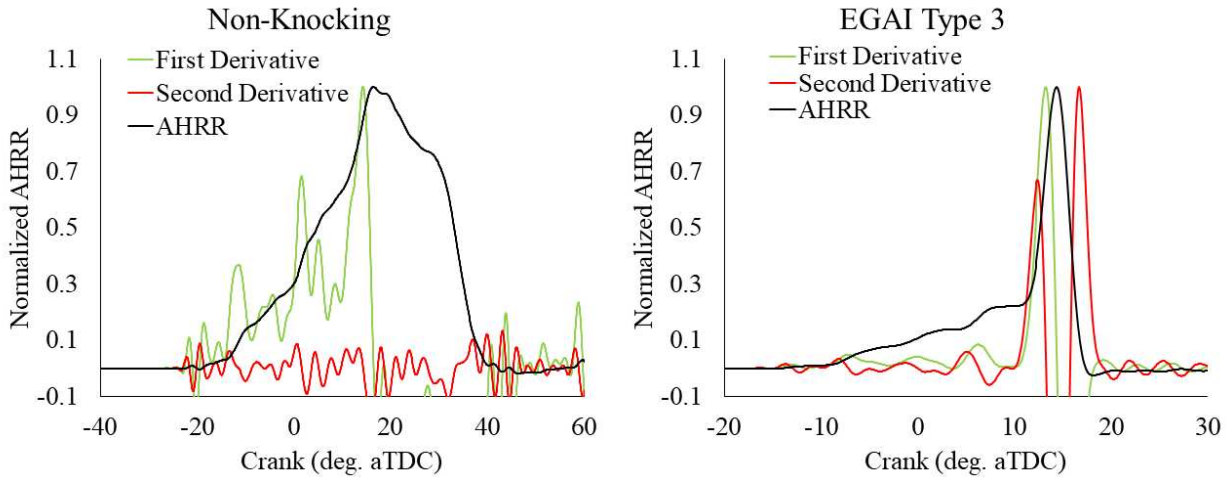

Figure 4.2: Comparison of the first and second derivatives behavior under non-autoigniting conditions and "EGAI Type 3." Top plot shows, through the second derivative, that the slope of the AHRR does not change up to its maximum (oscillations are due to noise). The bottom plot shows a constant slope of the EGAI curve up to the onset of EGAI, where there is a sharp increase in the AHRR slope.

An important observation that needs to be made is that these AHRR profiles are noticeable primarily on AHRR curves for individual engine cycles. Cycle-averaged AHRR curves can smooth out the local minimum points and characteristic shapes due to the various levels and onsets of EGAI; thus, in this work, only individual cycle AHRR curves are studied.

4.3 EGAI Signal Description

As mentioned in the previous section, the algorithm to detect and mark the onset of EGAI is based on local minimum points and rapid changes in slopes of the AHRR curve, which, due to the nature of AHRR calculation, are prone to misleading detection in the presence of excessive noise. Thus, a digital lowpass filter is applied to the cylinder pressure trace and the AHRR curve to remove the engine vibration-related noises using the MATLAB® software suite. The cut-off

frequency was selected based on the engine speed and sampling rate (7200 samples or every 0.1 °CA). The two engine geometries analyzed do not seem to influence the signal processing technique and, thus, no further treatment was taken. The analysis is performed between the Top Dead Center (TDC) of the firing stroke and the End of Combustion (EOC) crank angle since this is the window that EGAI can occur and to avoid any misleading results from noisy data during the other engine strokes. In this work, the EOC was defined as the location where the polytropic expansion process started and it was marked by detecting where the ratio of specific heats, gamma, became constant. Gamma was calculated by taking the slope of the Log-Pressure versus Log-Volume diagram. Figure 4.3 illustrates where the EOC was considered. Additionally, the intended use of this method is in individual cycles and not in the "mean-cycle" cylinder pressure traces. "Mean-cycle" cylinder pressures may smooth out the essential characteristics of the AHRR curve, preventing one from detecting an EGAI event. Using "mean-cycle" cylinder pressure traces also negates the attractiveness of the method, which is to determine, on a cycle-by-cycle basis, if EGAI is occurring and its quantification by the f-EGAI metric. Therefore, for this manuscript, calculations were performed for all recorded engine cycles, and, for the sake of data presentation , plots were created for a "representative cycle," or the individual cycle with the closest Peak Cylinder Pressure to the mean value from 1000 cycles. Finally, the same procedure used in [22] was used to determine whether a cycle is knocking for model validation against known data.

4.4 EGAI Detection and Quantification Algorithm

Having laid down the foundation for the method, the algorithm can now be described. The first variable to be marked is the location where AHRR is maximum. Then, having marked the location where the AHRR curve is maximum, the following conditions are checked, and conclusions are drawn if they are satisfied:

1. Is there a local minimum point after where the AHRR is maximum and before EOC?

    (a) If this condition is satisfied, "EGAI Type 1" is occurring.

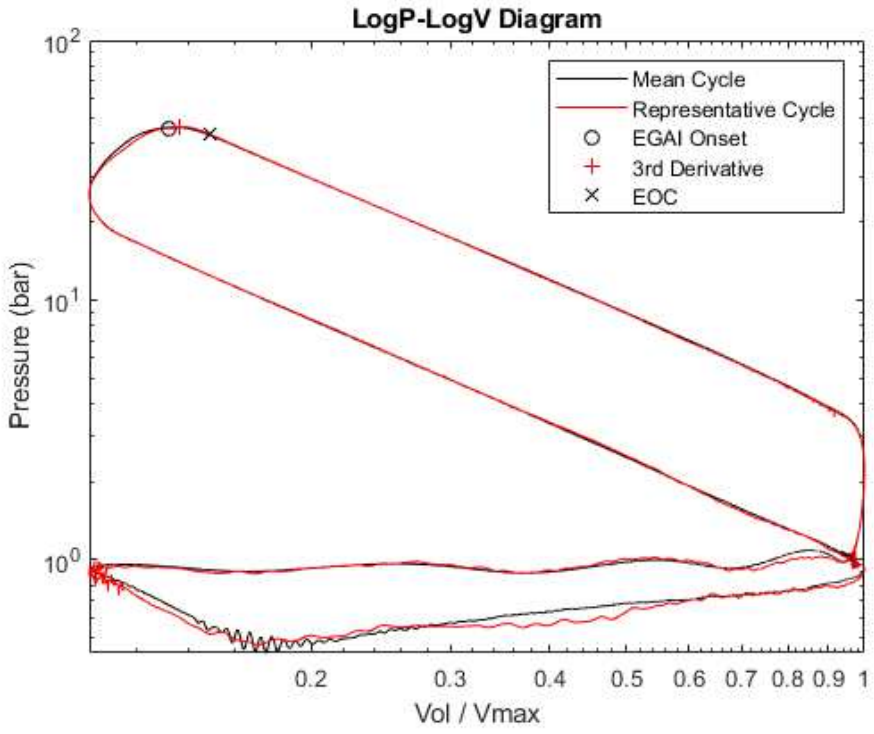

Figure 4.3: Illustration of the EOC considered in this work. The circle marks the onset of EGAI and the "x" marks the EOC. All analysis is performed for a single cycle, between TDC and EOC.

(b) The local minimum point location marks the onset of EGAI.

2. If (1) is not satisfied: is there a local minimum point between TDC and where the AHRR is maximum?

   (a) If satisfied, "EGAI Type 2" is occurring.

   (b) The local minimum point location marks the onset of EGAI.

3. If (1) and (2) are not satisfied: is there a point of a very rapid increase in the slope of the AHRR curve between TDC and maximum AHRR?

   (a) If satisfied, "EGAI Type 3" is occurring.

   (b) Location of the rapid increase in the AHRR slope marks the onset of EGAI.

4. If none of the above conditions are satisfied, the cycle is marked as non-autoigniting.

One should note that, in the above algorithm, no thresholds or user-defined targets are set to assign a cycle as autoigniting or to detect the onset of EGAI. Thus, this approach simplifies the detection of EGAI/knock, removes possible operator/engineer errors, and allows an EGAI detection solely based on the characteristic profile of the AHRR curve, regardless of engine hardware. In fact, as shown in Figures 4.1 and 4.2 and in the results section of this chapter, all computations were performed using the normalized AHRR curve for the two studied engines and all their operating conditions, which removes the influence of the engine operating conditions on the actual AHRR values, however, non-normalized AHRR curves can still be used and should, theoretically, work as well.

Finally, in order to quantify the relative strength of the EGAI event, the fractional EGAI (f-EGAI) metric is used. This metric was developed by Zdanowicz et al. [24, 86] and considers the fraction of the total energy released that participated in the EGAI event. Larger quantities of energy released by the EGAI even imply stronger autoignition, thus higher f-EGAI, and, conversely, lower energy released by the EGAI implies weaker and lower f-EGAI . f-EGAI is calculated according to equation 4.2 [24, 86]. This work assumed that all energy released after the onset of EGAI is due to the EGAI event. Although there might be limitations, this assumption has been shown to correlate well to EGAI intensity [19, 87].

$$f_{\text{EGAI}} = \frac{[\int \frac{dQ}{dt}]_{\text{EGAI}}}{\int \frac{dQ}{dt}]_{\text{Total}}} \tag{4.2}$$

4.5 Results and Discussion

The algorithm in the previous section was coded into MATLAB® and applied to an extensive database of AHRR curves for the CFR and Cummins X15 engines operating on a SI NG mode. The observation that motivated the development of the proposed method was the inability of other knock detection routines to determine the precise onset of EGAI, as noted by Bayliff [19]. For example, Figure 4.4 compares the onset of EGAI determined by the Third Derivative of the Cylinder Pressure Trace method [88] and the newly developed algorithm for the non-autoigniting and

"EGAI Type 1" cases, and Figure 4.5 for the "EGAI Type 2" and "EGAI Type 3" cases. In these figures, the left plot shows the representative AHRR curve for the given engine operating condition with marks for the EGAI onset determined with the new CECL method, by the third derivative of the pressure trace, and the EOC. The plots on the right of figures 4.4 and 4.5 compare the onset of EGAI determined by the CECL method (green) and by the third derivative of the pressure trace (red) for 1000 consecutive engine cycles. As can be seen in these figures, the third derivative method predicts a later onset of EGAI for all autoigniting cases, which can be visually inspected on the AHRR curve. In fact, the third derivative method consistently marks the second peak of the AHRR curve as the onset of EGAI instead of the local minimum point (EGAI types 1 and 2), where low-temperature chemical reactions start and cause EGAI. This error also leads to the smaller spread in onsets of EGAI detected by the third-derivative method since, for constant CA50 cases, the location of the maximum point of the AHRR curve should be somewhat constant. For the CFR engine cases studied in this work, the onset of EGAI predicted by the third derivative method is, on average, 4.1 crank-angle degrees later than those predicted by this newly developed method. In all these cases, the third derivative method successfully captures the start of the pressure oscillations; however, the slight crank angle differences between the onset of EGAI and pressure oscillations, which are a consequence of the EGAI event, lead to significant errors in the f-EGAI estimation, 20.1% on average. If one aims to have a Controlled EGAI (C-EGAI) operation by controlling the f-EGAI, these errors need to be mitigated and f-EGAI accurately estimated to ensure a stable operation. To put into context, the f-EGAI for the CFR engine ranges from 15%, the minimum acceptable f-EGAI in the CFR engine to be considered, to 57%. In the Cummins X15, f-EGAI ranged from 10% to 40%. Thus, the third derivative method is not suitable for this C-EGAI application since it can have a narrow window of operation. It is important to note that the range of acceptable f-EGAI is engine-dependent and will vary based on structural constraints. One interesting and important observation is the presence of cycles experiencing EGAI in an operating condition regarded as non-autoigniting. As can be seen in the top plots of Figure 4.4, the CECL

method is able to capture such random cycles experiencing EGAI even under very light EGAI conditions, as is the case for this operating condition.

Additionally to the CFR engine data shown in Figures 4.4 and 4.5, the CECL method was applied to the data acquired using the single-cylinder SI NG Cummins X15 engine at different operating conditions and NG compositions. Figure 4.6 shows a representative result from the Cummins X15 engine at a light EGAI condition. The CECL method again accurately captured the onset of EGAI even under very light EGAI conditions. While the differences between the third derivative of the pressure trace method and the newly developed method were reduced under these conditions, there was still a significant discrepancy between the two methods. The reason is that for the low levels of EGAI, the second peak of the AHRR is very low and near the local minimum point, which causes the third derivative method to predict a similar onset of EGAI. However, once more, the CECL method, solely based on the AHRR profile, showed to be a robust method for detecting EGAI even under very light conditions for two very different engine platforms/operating conditions, which are essential for a C-EGAI combustion mode. Additionally to detecting EGAI on different engine platforms, figures 4.4, 4.5, and 4.6 show that the CECL method can also be used for various MNs since the two engines used very different NG compositions with varying levels of MN. More specifically, results shown in figures 4.4 and 4.5 used composition "Pipeline Day 1" from Table 4.2 of MN 69, and results shown in Figure 4.6 used composition "X15 NG2" from Table 4.4 with MN equal to 74.9. Finally, the MATLAB® built-in function to time how long it takes to run a code was used and, for individual cycles, the code took up to 2 milliseconds to compute the onset of EGAI and f-EGAI.

4.6 CECL Method's Accuracy at Lower Resolutions

In order to validate the CECL method for detecting the presence and the onset of EGAI, coarser data of the CFR engine, with lower encoder resolution, was used. This coarser data was virtually generated by sampling, from the original data set, information at larger crank angle intervals, i.e., 0.2, 0.5, and 1.0 °CA, respectively. The hypothesis for this exercise is that if a coarser data set of

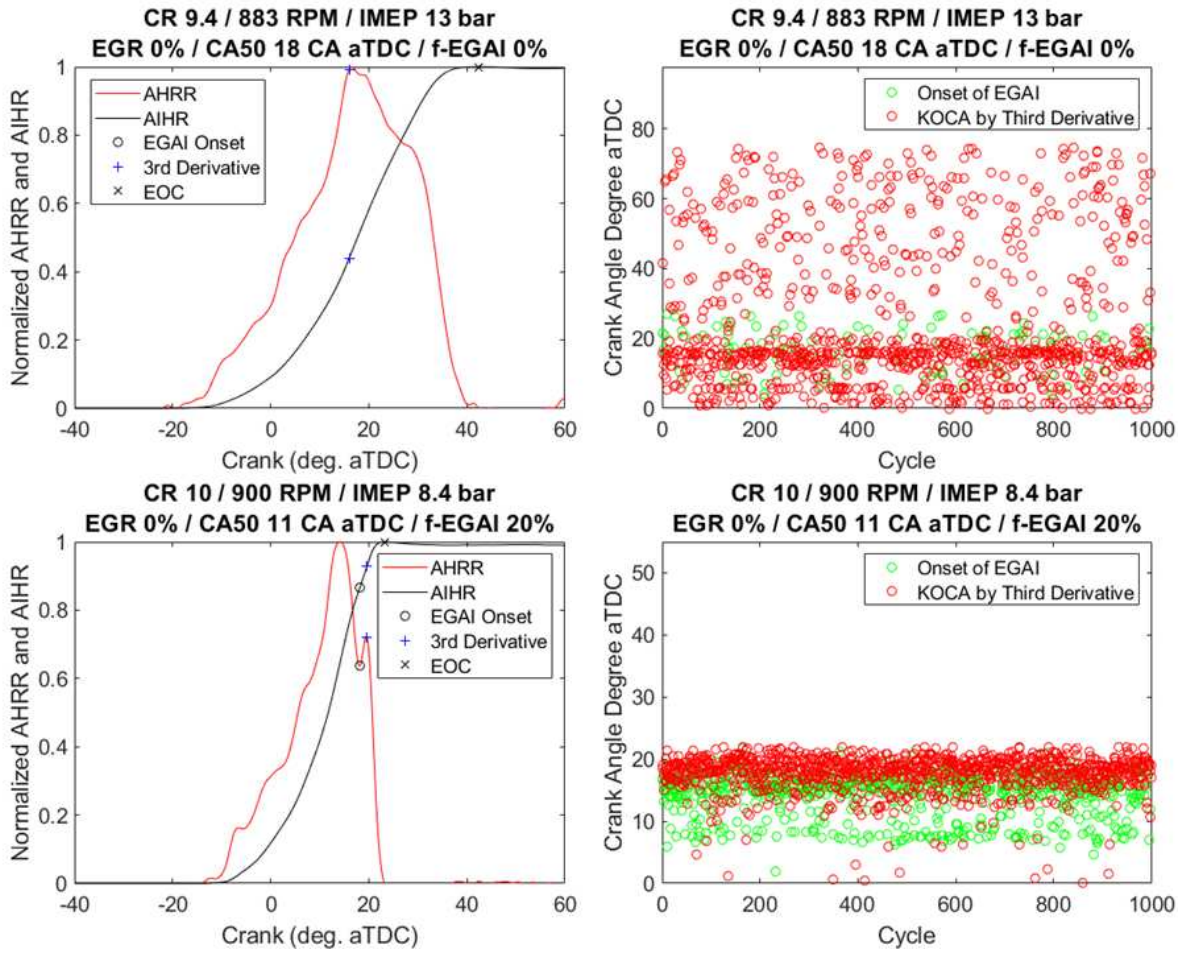

Figure 4.4: Comparison between the onset of EGAI determined by the newly developed method and the Third Derivative of the Pressure Trace for "non-autoigniting" (top) and "EGAI Type 1" cases (bottom).

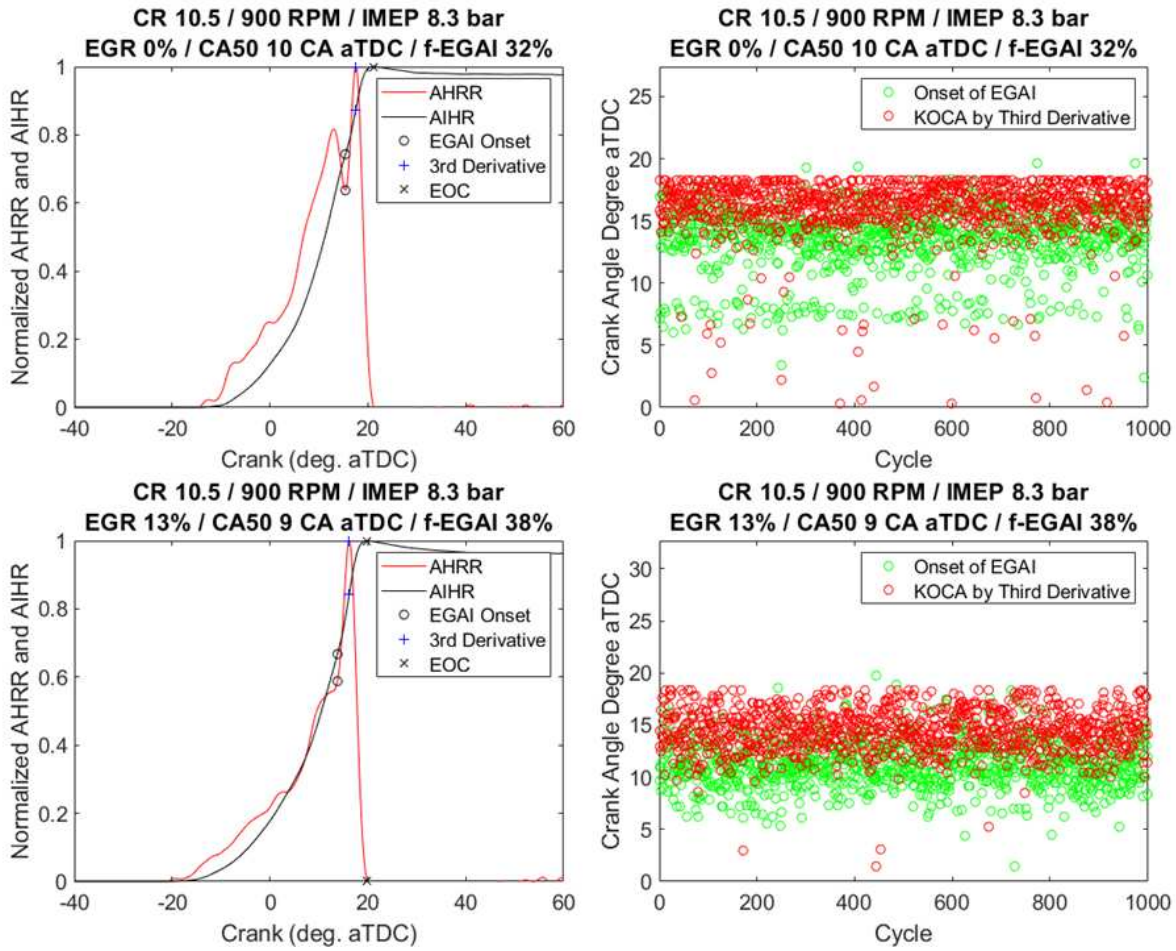

Figure 4.5: Comparison between the onset of EGAI determined by the newly developed method and the Third Derivative of the Pressure Trace for "EGAI Type 2" and "EGAI Type 3" cases.

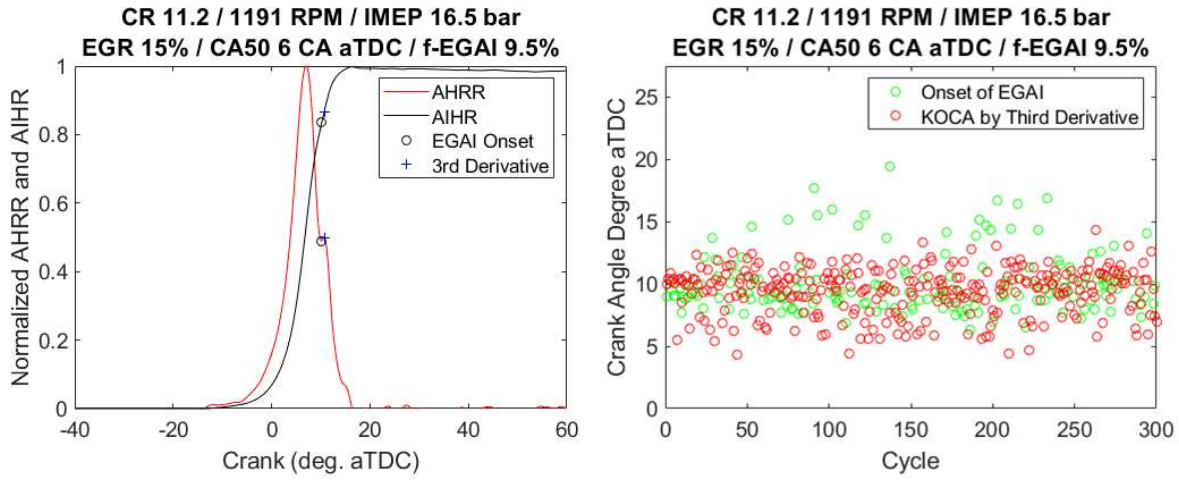

Figure 4.6: Cummins X15 onset of EGAI results. For very light EGAI cases, differences between the newly developed method and the third derivative of the pressure trace become small.

AHRR curves still has the essential features, i.e., local minimum points and rapid rise in slope, it will still be possible to use the CECL method to detect the presence and the onset of EGAI using commercially available low-cost cylinder pressure transducers. Figure 4.7 shows the coarsening result for the "EGAI Type 1" case shown in Figure 4.4. As can be seen, the coarsening of the data does not affect the main features of this type of EGAI-containing AHRR profile, even for the 1.0 °CA case. Figure 4.7 shows that the method performed well with the coarsened data, however, with the 1.0 °CA resolution, the accuracy of the onset of EGAI was affected. Additionally, Figure 4.8 shows a decrease in the density of green circles for the 1.0 °CA resolution data set, which is caused by the method failing to detect as many autoigniting cycles as it can detect when using data with finer resolution.

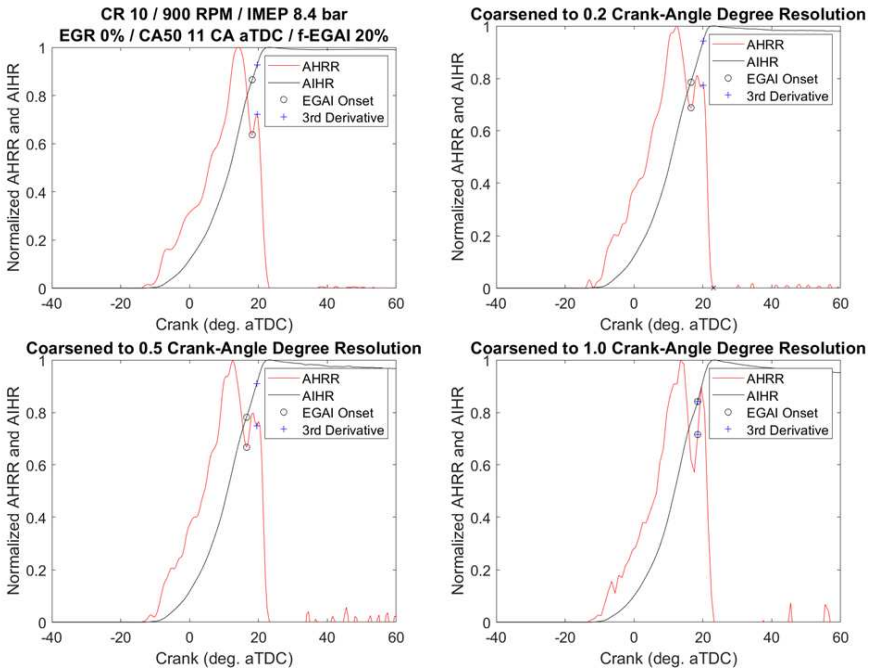

Figure 4.7: Detection and onset of EGAI under the "EGAI Type 1" condition and coarser data. For this EGAI condition, the method robustly predicted the occurrence and onset of EGAI.

Even though this new approach of detecting and finding the onset of EGAI seems appropriate for data with 1.0 °CA resolution, when the procedure is repeated for the "EGAI Type 2," the CECL method fails to detect the presence of EGAI, as shown in Figure 4.9. As shown on the lower-right

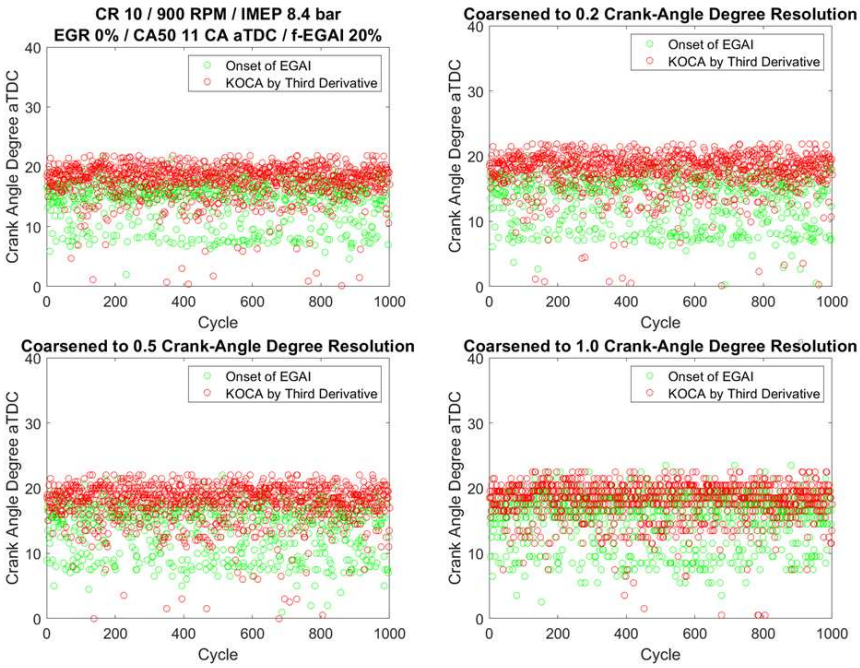

Figure 4.8: Comparison of the onset of EGAI predicted by the new method with the Third Derivative of the Pressure Trace. The newly developed method again more accurately predicted the onset of EGAI, however, for the 1.0 °CA resolution, it detected fewer autoigniting cycles than data with finer resolution.

plot, the second local minimum point disappears, removing the essential feature for the EGAI detection. On the other hand, for the "EGAI Type 3" shown in Figure 4.10, the essential feature of a rapid rise in AHRR slope at the onset of EGAI is kept during the data coarsening, allowing the method to detect the presence and onset of EGAI. As a measure of the compromises when using lower resolution data, Table 4.5 shows the errors on the predicted onset of EGAI for the representative cycle for each EGAI type using coarsened data.

Finally, Table 4.6 quantifies the method's effectiveness at detecting the presence of EGAI in the presence of coarser data. The cases shown in Table 4.6 are the same as those plotted in figures 4.7, 4.9, and 4.10. For each operating condition, 1000 consecutive engine cycles were recorded. As expected, the absolute error in the number of cycles with detected EGAI grows as the data becomes coarser. Although the method applied to a 1.0 °CA resolution data worked for the representative cycle shown in the previous plots, Table 4.6 shows that this encoder resolution is not ideal for the CECL method and, thus, should be used with caution. Additionally, the 0.5 °CA resolution works

Table 4.5: Error on the predicted onset of EGAI due to data coarsening for the representative cycle for each EGAI type.

EGAI Type	Original (0.1°)	0.2 °CA	Error	0.5 °CA	Error	1.0 °CA	Error
Type 1	18.2	16.7	-1.50	17.0	1.20	18.5	0.30
Type 2	15.4	15.8	0.40	16.4	1.00	EGAI Not Detected	
Type 3	11.8	11.8	0.00	12.9	1.10	13.4	1.60

well for the cases undergoing EGAI but introduces errors in the non-autoigniting cases, leading to false detections of EGAI.

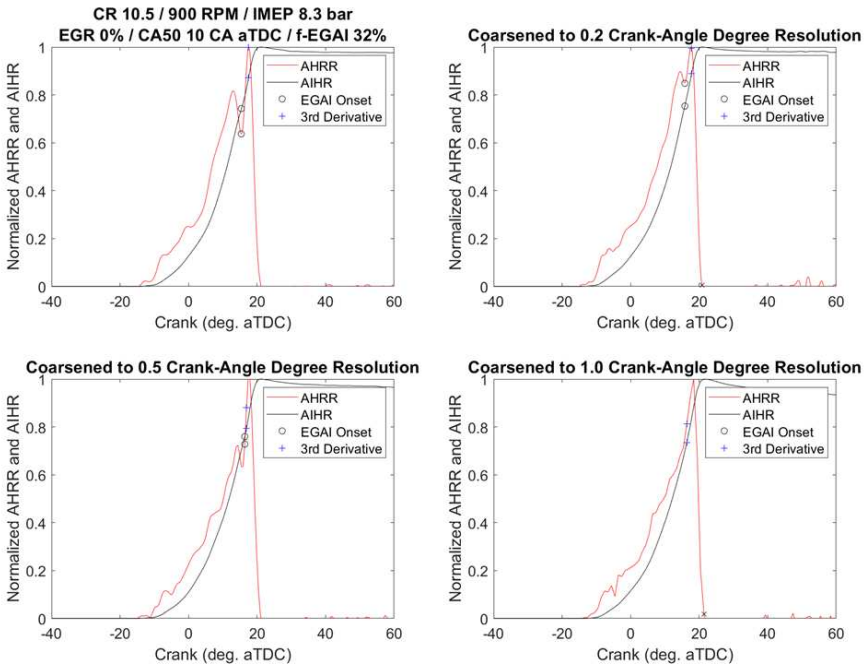

Figure 4.9: Detection of EGAI and its onset under "EGAI Type 2" AHRR profile using coarsened data. With 1.0-crank-angle degree resolution, local minimum points disappear, making the method unable to detect the presence of EGAI.

4.7 Summary

In this chapter, a method for detecting and quantifying the presence and onset of EGAI on individual engine cycles has been proposed based on the characteristic profile of the normalized

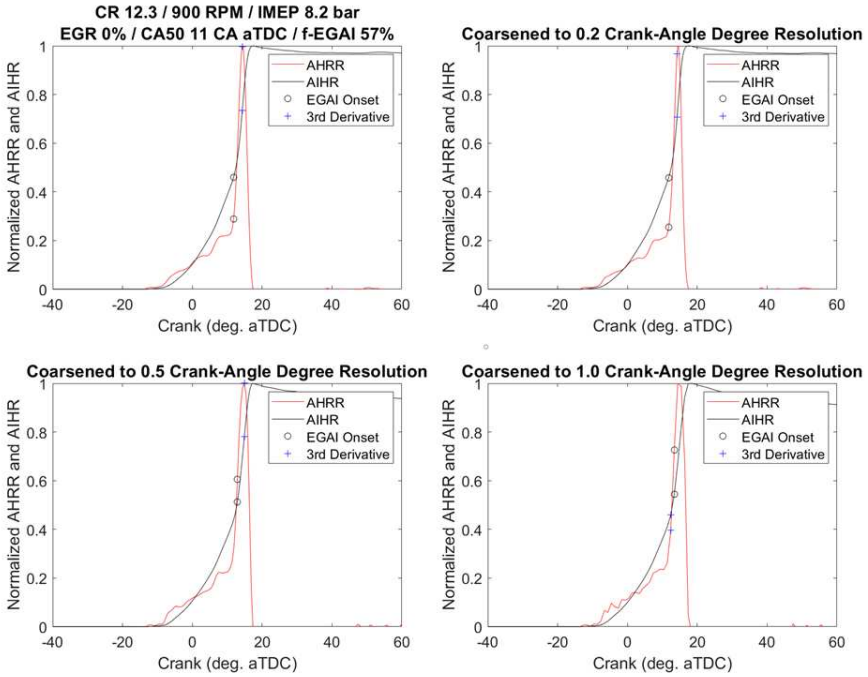

Figure 4.10: Detection of EGAI with coarser resolution and "EGAI Type 3." Under these conditions, the rapid increase in slope did not disappear, allowing the method to work correctly still.

Table 4.6: Cycles undergoing EGAI out of the 1000 consecutive engine cycles recorded.

EGAI Type	Original (0.1°)	0.2 °CA	Error	0.5 °CA	Error	1.0 °CA	Error
Non-autoigniting	106	98	-7.5%	138	30.2%	279	163.2%
Type 1	663	601	-9.4%	656	-1.1%	918	38.5%
Type 2	955	959	0.4%	969	1.5%	871	-8.8%
Type 3	990	983	-0.7%	969	-2.1%	579	-41.5%

AHRR curve under various engine operating conditions, EGAI severity, and NG compositions. The main conclusions of this chapter are:

1. The third derivative method of determining KOCA consistently predicts a later KOCA than actual;

2. Since there are similar profiles of AHRR curves for SI NG engines, a method can be developed to detect EGAI simply based on these profiles, removing the need for engine-specific thresholds;

3. The newly developed CECL method, solely based on the characteristic AHRR profiles, accurately captures the local minimum point location that characterizes the beginning of EGAI, allowing a more accurate calculation of f-EGAI that is essential to a C-EGAI combustion mode;

4. The CECL method takes up to 2 milliseconds to determine the presence and location of EGAI and its intensity, i.e., f-EGAI. This might indicate the possibility of using the CECL method in real-time control schemes. However, further studies need to be performed to confirm this hypothesis;

5. Coarser encoder resolution data should be used with caution since the main features used to detect the presence and location of EGAI can be lost. However, the analysis was performed by virtually coarsening the data, and further validation should be performed using real coarser data.

Chapter 5

CFR Engine Computational Modeling for NG Combustion and EGAI Investigation

With accurate detection and quantification of EGAI in SI NG engines, one could now study the main modeling approaches and intricacies related to modeling EGAI in SI NG engines. For this purpose, multiple modeling approaches, single- and multi-dimensional, were performed with the CFR engine described in Chapter 3.1 and their suitability for the various analysis strategies was evaluated. These models were also used to perform initial investigations on NG EGAI and its benefits on Indicated Thermal Efficiency.

This chapter describes the details of the three modeling approaches used and is part of a paper published at the Proceedings of the ASME 2020, Internal Combustion Engine Division Fall Technical Conference (ICEF2020) [21].

5.1 Engine Operating Conditions

The standardized Cooperative Fuel Research (CFR) F2 engine, described in Section 3.1, was used to acquire a total of 51 operating points necessary to support model development. The test points swept combustion phasing marked by the location at which 50% of fuel energy is released (CA50: 6.7-31.9 deg. aTDC), break mean effective pressure (BMEP: 3.2-7.0 bar), EGR levels (0-20%), and compression ratios (CR) (7.41-14.1:1). Additionally, three different fuel compositions were tested under the Methane Number (MN) test procedures as detailed in Wise et al. [89]. This strategy made it possible to observe four knock regimes: non-knocking, light knock, medium knock, and heavy knock. Table 4.2, presented in Section 4.1, shows the compositions and experimentally determined MNs of the four tested fuels. The Pipeline 1 and 2 fuels were sourced from the NG pipeline supplying the lab on two separate days of testing. The dry fuel composition was custom blended and selected to represent a typical high MN NG supply and the Wet blend was

formulated to mimic the composition of a reactive NG. The Pipeline 2, Dry, and Wet fuels were tested under MN test conditions and, as such, data with their CH_4/H_2 reference mixtures were also acquired.

5.2 Computational Models

Three modeling approaches were taken in this work, namely, 1-D GT-Power TPA model, 3-D CONVERGE CFD utilizing SAGE as the combustion sub-model, and 3-D CONVERGE CFD utilizing a hybrid combustion sub-model consisting of G-Equation and SAGE. Section 2.3 presented a review of the theory behind these models, however, in the subsequent subsections, a more detailed description of the model developed for the CFR engine is presented.

All CFR engine models presented in this work were based on the solid CFR engine models generated using an X-Ray scan by Argonne National Laboratory [45, 90] with minor changes highlighted in Section 5.2.2.

5.2.1 1-D Three Pressure Analysis Model

A 1-D Three-Pressure Analysis (TPA) CFR model was created using GT-Power [26]. The outputs of this model were later used to define initial and boundary conditions for subsequent CFD engine modeling, discussed later. As described in Section 2.3, the 1-D TPA GT-Power modeling approach is a non-predictive analysis performed to calculate parameters that are difficult or impossible to be measured in the test cell, such as burn rate, wall temperatures, trapping ratio, residual fraction, among others. Three crank angle resolved pressures are necessary as inputs: intake, exhaust, and cylinder pressures together with time-averaged intake and exhaust temperatures. Since this is a simplified 1-D model and does not contain a detailed 3-D solid model in it, discharge coefficients according to [91] and valve lift profiles at zero valve lash according to [90] were used to correctly account for the volumetric efficiency. Cylinder walls, ports, and valve temperatures were calculated using the Cylinder Wall Temperature Solver and the Finite Element Cylinder Structure Geometry modules employing the Woschni correlation [92]. With this simplified 1-D model, initial

and boundary conditions, e.g. wall temperatures, in-cylinder temperature, and intake and exhaust initial gas temperatures, were calculated and used in the 3-D CFD models. Additionally, the 1-D model provides the amount of expected Residual Gas Fraction (RGF) necessary for the generation of the laminar flame speed tables required by the G-Equation as shown in Section 2.3. Figure 5.1 shows the TPA model of the CFR engine.

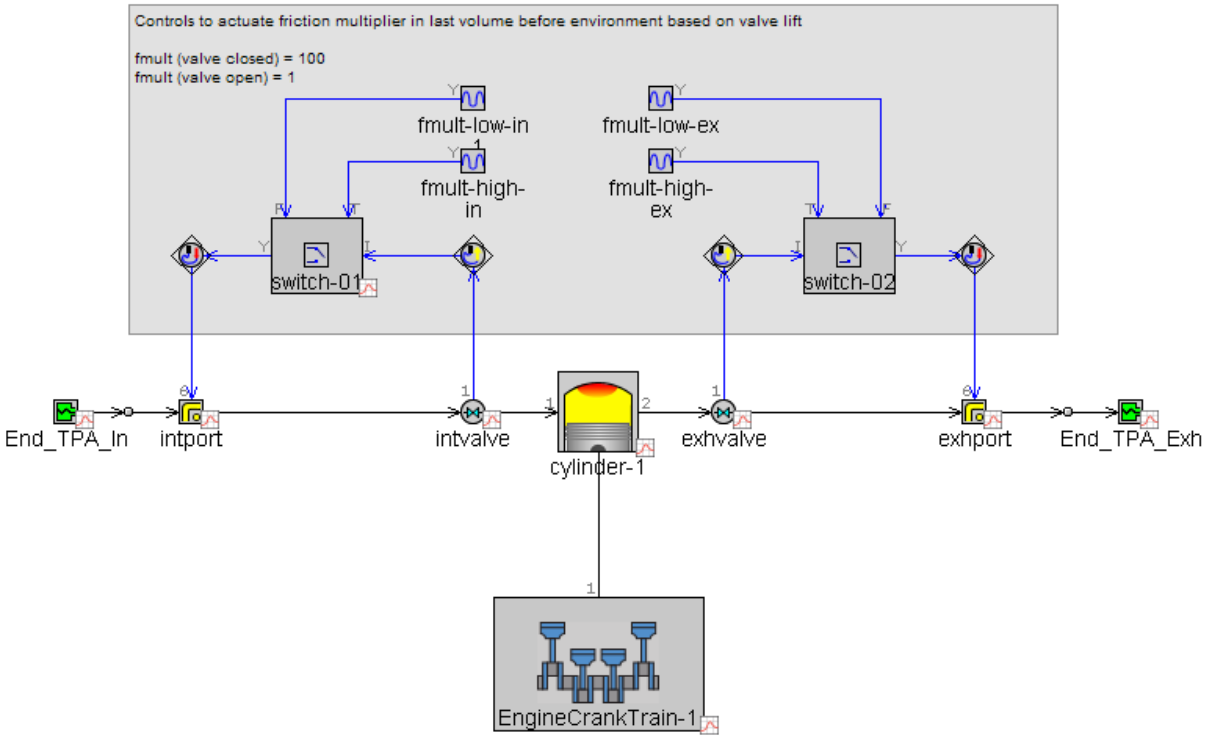

Figure 5.1: 1-D GT-Power TPA Model of the CFR Engine.

5.2.2 3-D CFD Model with Chemical Kinetics

CONVERGE CFD version 2.4 [27] was used to carry out the 3-D modeling of the CFR engine. As mentioned previously, the surface mesh utilized in the simulations was generated from an X-ray scan performed by Argonne National Laboratory and incorporates realistic geometry features of the intake and exhaust ports, knockmeter cavity, spark plug, and the 180° intake valve shroud.

Figure 5.2 shows the surface of the CFR engine used in the 3-D simulations. This surface mesh was updated from the original (ANL's engine) to match the conditions found in the CSU's CFR engine. Namely, the knockmeter cavity, spark plug, and piston crevice were updated and/or added to account for the actual geometry of the CFR engine at CSU. The pressure transducer for the in-cylinder pressure measurement is installed on the knockmeter cavity and is flush with the cylinder head. The spark plug used in the CSU's CFR engine was measured and its dimensions were included in the model to account for the correct spark plug gap, J plug, crevice volume dimensions, and orientation. Figure 5.2 shows the surface geometry used. Features in red were updated from ANL's CFR engine.

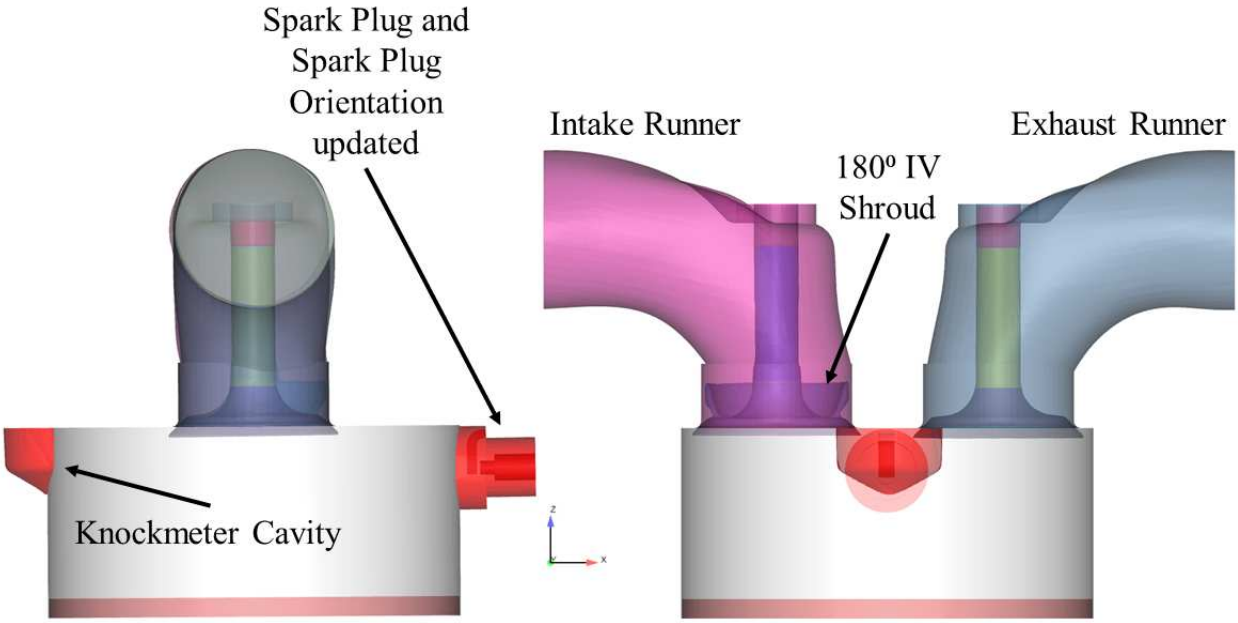

Figure 5.2: Surface Mesh of the CFR engine used in the CFR simulations. Features in red were updated to match CSU's CFR engine.

The base grid size for the mesh generation used was 4 mm outside of the cylinder. Inside the cylinder, a permanently fixed embedding for the cylinder region was used to refine the base grid down to 1 mm. Four levels of fixed embedding were specified to compute the spark kernel and initial flame propagation (grid size of 0.250 mm). Near the walls, three levels of boundary embedding were used to resolve heat transfer. Additionally, AMR was used to refine grid size

down to 0.5 mm inside the cylinder based on temperature and velocity subgrid scales of 2.5 K and 1 m/s, respectively. Turbulence was modeled with the RANS and RNG $k-\epsilon$ model. According to [36, 93, 94], these grid sizes are sufficient to simulate normal and knocking combustion with RANS in SI engines. To account for wall heat transfer, the model proposed by O'Rourke and Amsden [95] was employed.

To initiate combustion, a model for the spark event is necessary. In order to model the spark appropriately, two spherical energy sources of 0.5 mm in radius were used in the spark plug gap between the electrodes, creating an "L" energy deposit profile which represents the breakdown, arc, and glow phases. The duration of each energy deposition event was 0.5 degrees for the first event and up to 16 degrees for the second. Their intensities were selected based on the parameters measured during the CFR engine testing, i.e. up to 125 mJ. The chemical mechanism used in this work for all models is a reduced mechanism from ARAMCO 3.0 [96] with 82 species and 519 reactions, named ARIES82 [48,49]. Figure 5.3 compares calculated ignition delays for ARAMCO 3.0 and ARIES82 at 40 bar and stoichiometry.

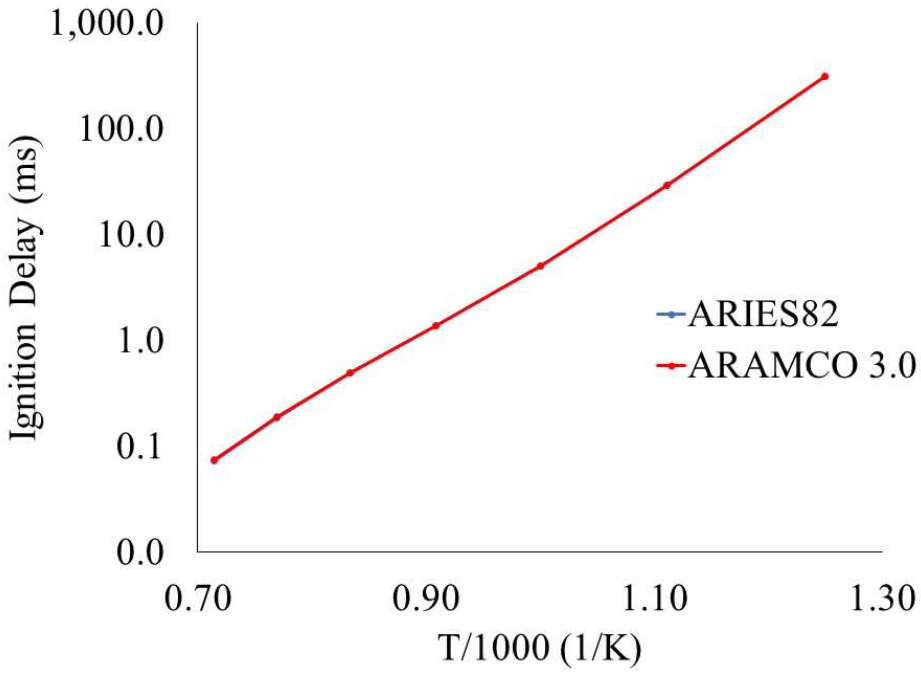

Figure 5.3: Ignition Delay comparison between ARIES82 and ARAMCO 3.0. ARIES82 ignition delay predictions agree quite well ARAMCO 3.0 predictions

5.2.3 3-D CFD Model with Level Set Approach

The G-Equation Flamelet Model based on the Level Set Approach [42] was also used to simulate the CFR engine. This model shared the same CFD parameters with the SAGE-based model except for the combustion sub-model.

Recalling the model derivation provided in Section 2.3, the combustion chamber is divided into two regions by the iso-surface $G(\mathbf{x}, t) = 0$: the unburned and burned regions. The G-Equation plus SAGE combustion sub-model consists of tracking the flame propagation using the G-Equation, equation (2.24), and solves the detailed kinetics using SAGE in the unburned region to detect EGAI and in the burned region to solve for the post-flame chemical reactions. Therefore, laminar flame speeds and a chemical kinetics mechanism able to capture EGAI chemistry for the fuel of interest are necessary as model inputs. Laminar flame speeds were provided to the G-Equation in the form of a lookup table generated for each fuel *apriori* simulations. ARAMCO 3.0 [96] mechanism and the 1-D chemistry tool in CONVERGE were used for the lookup table generation. The range of parameters used to generate the flame speed lookup tables was 400-1100 K for temperature with 100 K steps, 10-70 bar for pressure with 5 bar steps, 0.7-1.3 for equivalence ratios with 0.1 steps, and 0-30% of dilutants with 10% steps. The maximum concentration of dilutants was chosen to be 30% by mass since the sum of the RGF plus EGR did not exceed 30% in the experiments as estimated using the 1-D TPA model. In this work, the calibration process found that model constant b_1 in equation (2.24) equal to 2.1 is sufficient to simulate all cases.

5.3 Modeling Results

5.3.1 1-D Three Pressure Analysis Model Results

Model validation was performed using data acquired for Pipeline 1 NG at a variety of CA50, BMEP, and EGR rates. To ensure proper volumetric efficiency and, therefore, correct trapped mass for each operating condition, the intake valve flow area multiplier was set to 1.25 for all cases, which ensured fuel flow rates and air flow rates agreed within 5% of the measurements, which is within the measurement uncertainty. Correctly matching fuel energy at each operating

point makes the tuning of the overall cylinder heat transfer convection multiplier reasonable since heat transfer is modeled using correlations that might not be accurate during knocking combustion [90]. Therefore, the overall cylinder heat transfer multiplier was varied up to 1.15 to match net IMEP. Gamma Technologies recommends a maximum of 1.1 [26], however, other researchers have successfully used multipliers up to 3 [90]. Figure 5.4 shows predicted versus measured fuel and air flow rates for all test conditions.

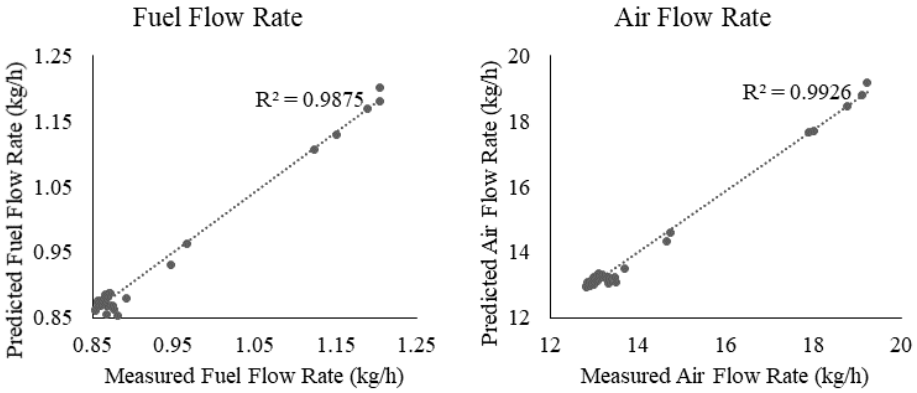

Figure 5.4: TPA Model of the CFR Engine: flow rates results agree well with experimental data and within measurement uncertainty.

Performance parameters also agree well with all test cases, matching experimental CA50 within 2 deg., and all but two cases within 1 deg. Average Peak Cylinder Pressure (PCP) is also within 2%, and PCP location within 1 deg. Figure 5.5 shows plots of the predicted versus measured quantities mentioned above. Figure 5.6 shows two representative cylinder pressure traces.

5.3.2 3-D CONVERGE CFD Model Results

Ten operating points were simulated using the 3-D CFD models for the four different fuel compositions. Simulations with Pipeline 1 had parameters such as CA50, CR, BMEP, and EGR varied to achieve different operating conditions and knock intensities (KI), which were calculated according to the procedure in Wise et al. [89]. For Pipeline 2, the MN Reference CH_4/H_2 blend, and the Dry NG, tests were carried out under the MN test procedure conditions, as reported in [22], therefore, spark timing for these cases was held constant. This differed from the tests with Pipeline

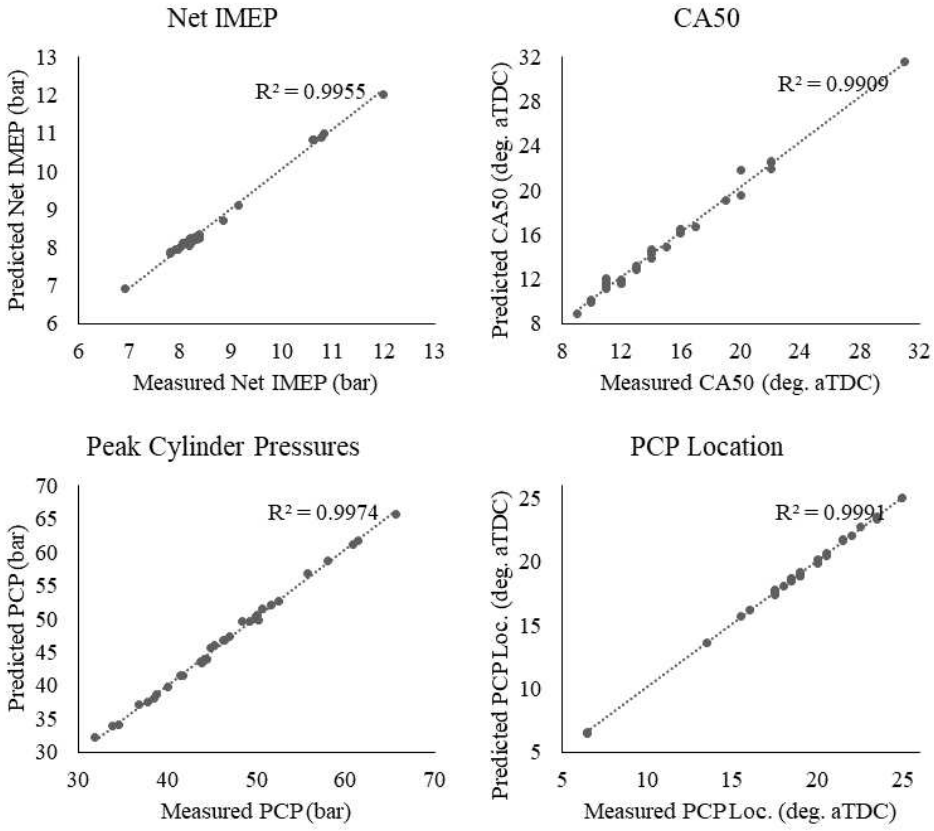

Figure 5.5: TPA Model of the CFR Engine: IMEP, CA50, PCP, and PCP location also agree well with experimental data.

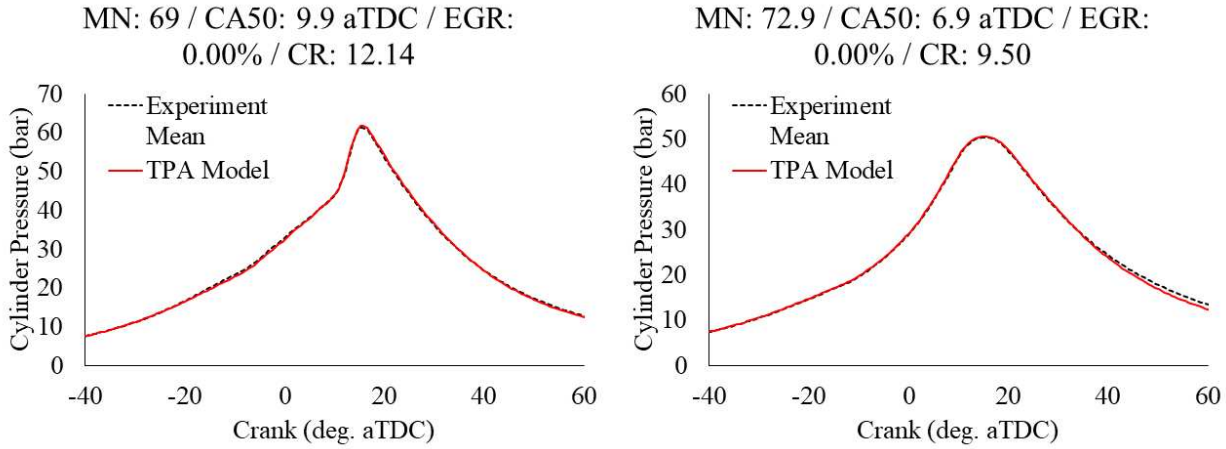

Figure 5.6: TPA Model of the CFR Engine: two representative cylinder pressure traces showing the good model agreement with experimental data.

Table 5.1: Range of Wall Temperatures used in the CFR Engine CFD Model.

Boundary	Min. Temp. (K)	Max Temp. (K)
Cylinder Wall	425.76	463.38
Cylinder Head	456.45	529.93
Piston	422.49	463.38
Int. Valve Face	483.96	605.15
Exh. Valve Face	522.72	670.93
Int. Valve Rod	428.86	490.75
Exh. Valve Rod	462.27	544.63

1 where the spark timing was allowed to vary to maintain constant CA50 from cycle to cycle. Since the KI for operating conditions under the MN test are low and spark timing is fixed, the Pipeline 2 cases and the corresponding MN Reference blend were selected for the G-Equation Level Set Approach model calibration. The assumption is that if the model is tuned to predict burn rates and light knocking events just beyond the knock limit of such different fuel compositions, as required by the MN test procedure, it will be able to predict the onset of stronger knocking events when higher end-gas temperatures (from higher BMEP) are present. This is due to the exponential decrease in ignition delays and their reduced uncertainty at higher temperatures. All ten simulated operating points were run for one engine cycle with initial and boundary conditions estimated using the 1-D TPA model. Table 5.1 shows the range of the wall temperatures used in the CFD simulations. Additionally, a spark energy of 20mJ was sufficient to achieve stable combustion and satisfactorily match CA10 in the G-Equation model.

SAGE model calibration started from the calibrated G-Equation model. It was found that SAGE is more sensitive to spark energy. A spark energy of 20mJ was not enough to achieve good CA10, CA50, and PCP agreement and, therefore, was increased to 125mJ, closely matching the energy used in the experiments. Additionally, a large sphere embedding around the spark plug was necessary to properly match CA10 and CA50. Figure 5.7 shows a comparison of the spark settings on the heat release rate plot.

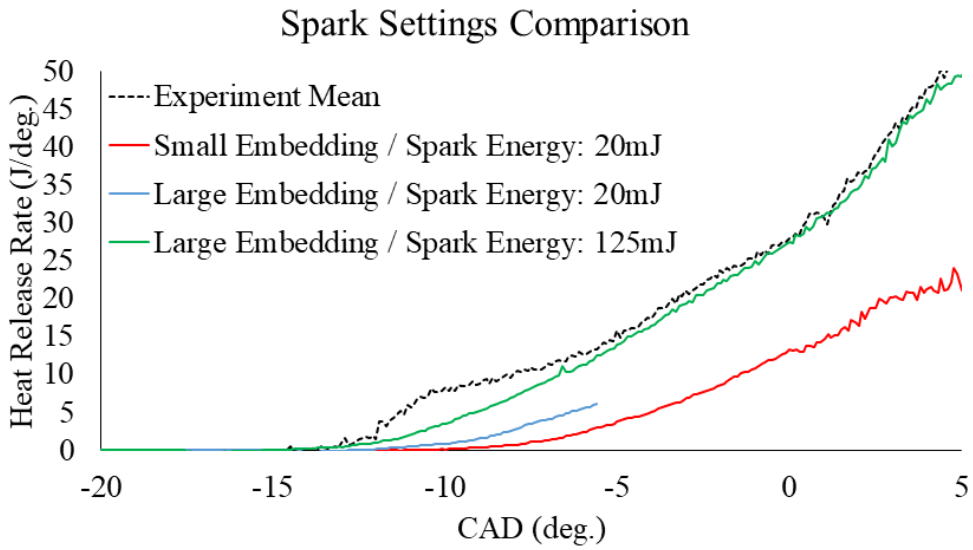

Figure 5.7: CFR CONVERGE CFD model: Spark Modeling Comparison used in the SAGE combustion sub-model.

Figure 5.8 shows CFD results for three different cases (from left to right): light knock used in the G-Equation calibration, medium knock with SAGE, and heavy knock with G-Equation approach. As can be seen, good agreement with cylinder pressure trace and heat release rate is found for all cases. In fact, average error for PCP is -0.03%, PCP location: +1.01 deg., CA50: +0.12, and IMEP: +2.4%. For the knocking cases, knock onset crank angle (KOCA) was predicted on average 1.65 degrees later than the experiments, resulting in an average of 3.5% lower EGAI fraction (f-EGAI). The reason for this later knock event is perhaps due to the uncertainties in the reduced mechanism and the fact that NO_x (present in the EGR) chemistry was not accounted for but has been shown to shorten ignition delay times as suggested by [48–51].

5.4 Discussion

5.4.1 Comparison of the Different Modeling Approaches

The 1-D TPA model is a non-predictive model where experimental data is required. Using experimental data, GT-Power calculates the burn rate for each operating point in an iterative manner. From the calculated burn rate, other parameters are then calculated, resulting in a useful model

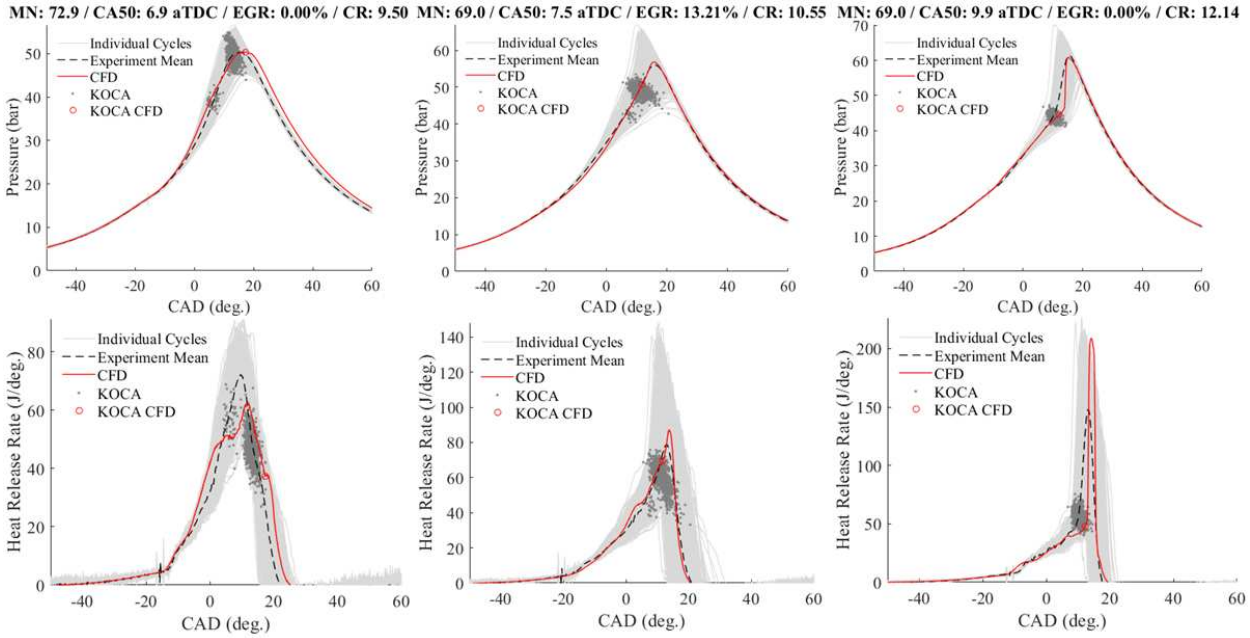

Figure 5.8: CFR CONVERGE CFD model: Pressure traces of three representative engine operating conditions. Left: G-Equation calibration. Middle: medium knock intensity with SAGE. Right: heavy knock with G-Equation.

for experimental data assessment. Additionally, sub-models can be calibrated using TPA to ensure their agreement with experimental data before a predictive model is calibrated. This model is also computationally inexpensive where, in this work, the total simulation time was about 6 minutes for 34 operating points running on a typical workstation. The main disadvantage of the model is its lack of prediction of engine results without experimental data, however, this is easily circumvented by calibrating a SI Turbulent Flame Combustion Model, which, based on a fully calibrated TPA model, has the ability to predict engine results. Furthermore, the various multipliers available in GT-Power are very useful to circumvent the simplified correlation limitations, however, they can be a tricky option for the inexperienced user, where by over-utilizing them one can match experimental data for the wrong reason.

In the 3-D CFD models, the chemical kinetics solver SAGE model showed to be a good option for initial simulations when experimental data is not yet available. This is due to the fact that it does not require model constant parameter calibration as in the G-Equation modeling approach. In this work, by virtue of matching CA10 and CA50, engine parameters such as PCP, PCP location,

CA90, and gIMEP resulted in values close to the mean values and well within the experimental data spread (Figure 5.8). However, chemical mechanism accuracy affects SAGE results and performance and, therefore, it is usually a more computationally expensive simulation depending on the size of the mechanism used. In this work, the average simulation time with SAGE was 29% longer than the G-Equation modeling approach. On the other hand, G-Equation can not only be more computationally efficient but also take advantage of more detailed chemical kinetics for the flame speed lookup table generation and the use of reduced mechanisms in the end-gas for knock detection, since flame propagation and chemistry are decoupled. This method allows one to use more accurate/detailed chemistry where it is needed without severely compromising computational efficiency. However, as stated before, some level of calibration is necessary for the model parameters, such as the b_1 constant [42, 97] making it a less predictive model. Lastly, G-Equation allows for the calculation of the flame speeds in the domain by solving equation (2.26) and, since this is an important parameter, the G-Equation approach was chosen for the analysis of EGAI.

5.4.2 Natural Gas Combustion and EGAI Analysis

The CFR engine models are intended to aid in the understanding of NG combustion and EGAI, i.e. engine parameters and fuel properties that lead to end-gas autoignition, and shine light on possible strategies on how to operate an NG engine in a controlled end-gas autoignition (C-EGAI) mode. An interesting observation is the positive correlation between f-EGAI and KI. As shown in Figure 5.9, f-EGAI appears to have a linear correlation with KI. The same behavior is captured by the 1-D TPA model where the simulated KI was estimated using the Gamma Technologies method [26] which takes into account fuel activation energy, EGR concentration, and equivalence ratio. The implication of this correlation is the possibility to run CFD simulations much more efficiently since to accurately capture KI in a CFD model one has to run multiple cycles and set the Mach Courant-Friedrichs-Lewy (CFL) number to be approximately or smaller than 3 [35, 47] in order to properly capture the pressure fluctuations inside the cylinder. If a correlation between KI and f-EGAI exists, then one could use the approach taken in this work, namely single cycle

simulation with Mach CFL set to 50, to estimate KI for a given engine from f-EGAI and greatly reduce computational cost.

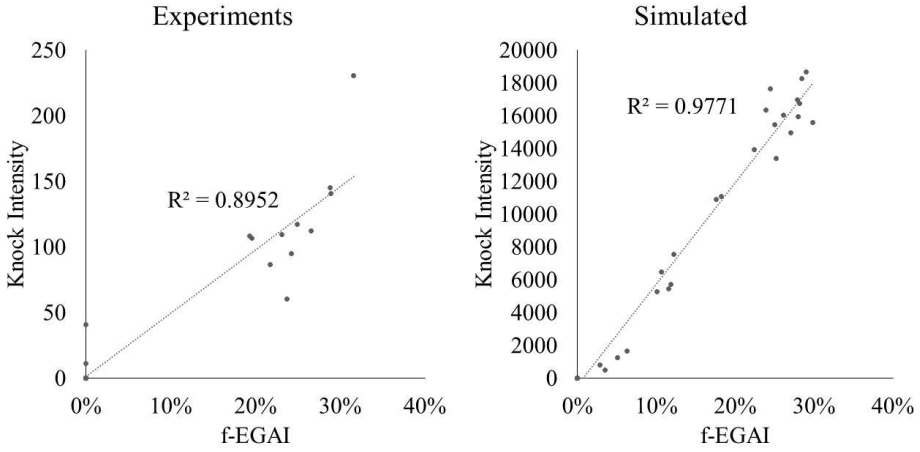

Figure 5.9: CFR Engine KI versus f-EGAI. Model trend agrees well with experimental trends.

Additionally, Figure 5.10 shows that there is an opportunity to increase engine thermal efficiency by using C-EGAI. As can be seen, increasing f-EGAI, indicated thermal efficiency also increases up to a maximum before falling off. It is also important to highlight that the knocking cases shown in Figure 5.10 had many parameters varying at the same time, so it should not be considered to directly correlate f-EGAI on indicated efficiency. Here again, the 1-D TPA model captured well the experimental observations, further validating its accuracy and utility.

Furthermore, additional important observations can be made using the 3-D CFD results. Figure 5.11 shows the effect of increasing EGR fraction and retarding CA50 on EGAI. It can be seen that EGAI is suppressed with higher EGR rates as a result of the combined effect of lower end-gas temperatures and reduced laminar flame speeds (LFS). Retarding CA50 and lowering CR also shows the same suppressing effect on EGAI due to cooled end-gas temperatures.

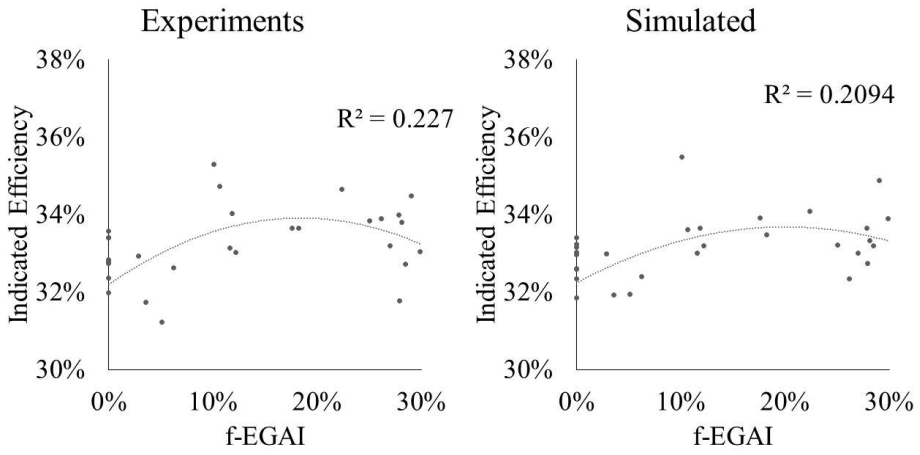

Figure 5.10: CFR ITE versus f-EGAI. Relation between ITE and f-EGAI shows that there is an opportunity to increase ITE by utilizing C-EGAI.

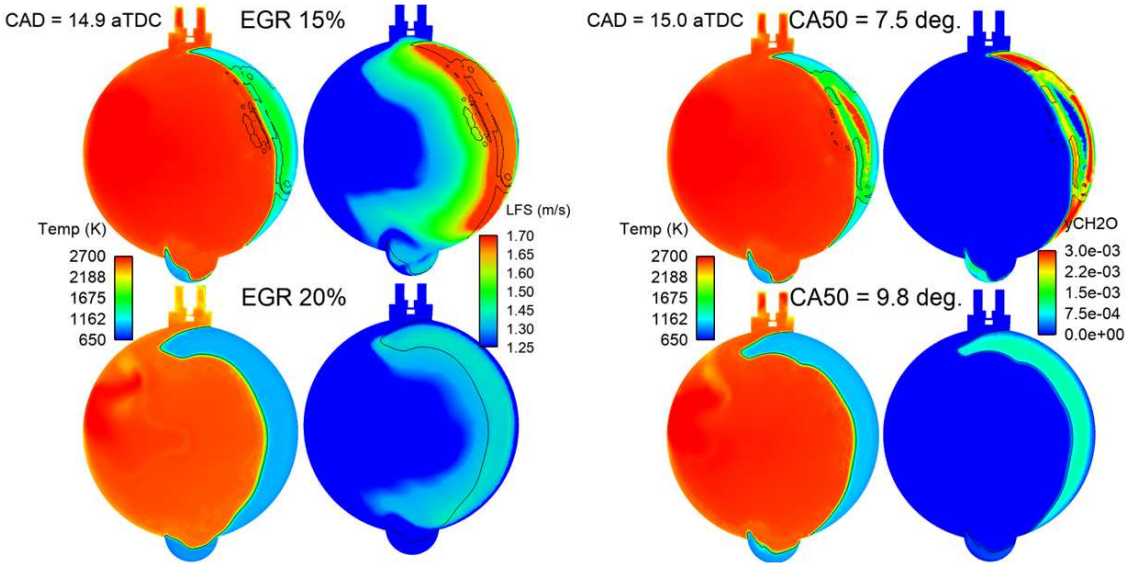

Figure 5.11: Left: effect of increasing EGR on EGAI. Right: effect of retarded CA50 on EGAI.

Chapter 6

NO_x Chemistry Effects on End-Gas Autoignition

As discussed in Section 2.4, research has shown that NO_x (NO/NO_2) chemistry influences HC oxidation [52–57], inhibiting or promoting EGAI depending on the fuel composition, thermodynamic state of the unburned gas, and NO_x concentrations. Additionally, Chapter 5 showed how the absence of NO_x chemistry in chemical mechanisms leads to a later EGAI prediction in SI NG engine models. Additionally, to the best of the author's knowledge, there has not been developed a reduced mechanism capable of capturing real NG combustion and its non-trivial interactions with NO_x species that is suitable, size-wise, for multi-dimensional engine simulations.

Therefore, to bridge this gap in the literature, a reduced NG/oxidizer/NO_x combustion mechanism was developed with the aim to be of suitable size for multi-dimensional engine simulations while capturing the non-trivial interactions of varying NG blends/activities with NO_x. To generate the new reduced NG/NO_x mechanism, NO_x chemistry was added to the previously developed reduced NG mechanism by Mohr et al. [48, 49] called ARIES82 and was validated using previously published IDT data [48, 49]. In this chapter, a brief discussion on the important species and reactions for NG/NO_x oxidation is provided and the mechanism's performance is compared to state-of-the-art detailed mechanisms (i.e., NUIG Mech1.2 and ARAMCO 3.0). Finally, the newly generated reduced NG/NO_x mechanism was employed in a multi-dimensional CFD IC engine model and compared to experimental engine test data, highlighting the importance of NO_x chemistry on NG EGAI prediction under engine-relevant conditions [21, 22].

6.1 Homogeneous Ignition Delay Data

The experimental data utilized in this study was gathered by Mohr et al. [48, 49] and is briefly described in this section. Utilizing the RCM described in Section 3.3, Mohr et al. tested three synthetic NG fuel compositions with varying concentrations of CH_4, C_2H_6, and C_3H_8 to simulate the spread in reactivity (quantified by the Methane Number) seen in the US NG supply chain. The

Table 6.1: Fuel compositions utilized to analyze NO_x influence on NG homogeneous autoignition. Concentrations are in Mol%.

Species	Dry	Intermediate	Wet
CH_4	99%	95%	82%
C_2H_6	0.5%	4%	15%
C_3H_8	0.5%	1%	3%
MN	95	86	68

Table 6.2: Synthetic NO_x compositions utilized to analyze NO_x influence on NG homogeneous autoignition. Concentrations are in Mol%.

Species	Reactive EGR	Non-Reactive EGR
Ar	79.3%	80.0%
CO_2	20.0%	20%
CO	0.35%	-
NO	0.35%	-

three synthetic NG compositions referred by Mohr et al. as dry, mid, and wet are provided in Table 6.1, along with their calculated Methane Number (MN). Mohr et al. conducted tests with synthetic EGR substitution rates at 0%, 10%, 20%, and 30% by mass for each fuel composition. The synthetic R-EGR composition, shown in Table 6.2, was chosen to simulate a typical medium-duty SI NG engine EGR composition. Although EGR composition will change with engine operating conditions, the same composition was used across all test points to maintain consistency. Additionally, the mid fuel composition was also tested with an NR-EGR composition to assess the effect of reactive species in the EGR on NG homogeneous autoignition. The NR-EGR composition is also provided in Table 6.2.

As can be seen in these tables, no N_2 or H_2O were utilized in these experiments. This is due to the nature of the RCM, where, to avoid condensation and ensure good mixing, no H_2O was utilized to compose the synthetic EGR blends, having the CO_2 concentration adjusted to match the same gamma as an EGR blend with H_2O. Argon (Ar) replaced N_2 to achieve different compressed

temperatures and pressures for the same compression ratio through manipulating the mixture's ratio of specific heats.

Each of the fuel and EGR compositions were tested at a fixed initial pressure of 1 bar and three different initial temperatures: 35 °C, 45 °C, and 55 °C. This approach resulted in different compressed temperatures at similar compressed pressures. The homogeneous ignition delay time was then calculated as the time between the RCM's pistons reached TDC and the time at the maximum temperature or pressure derivative.

Mixture preparation was performed as described by Mohr et al. [48, 49], where, to ensure good mixing, NG/oxidizer/EGR mixtures were stored in mixing tanks for up to 2 hours. As noted in [98], extended storage of mixtures containing NO and O_2 can lead to NO conversion into NO_2 via $2NO+O_2 \leftrightarrow 2NO_2$. In this study, constant volume calculations were performed to estimate the correct amount of NO converted into NO_2 after 2 hours of mixing, and this composition was used in the homogeneous IDT calculations. For the 30% R-EGR mixtures, roughly 90% of NO was consumed to NO_2 over the course of the 2-hour mixing duration.

6.2 Reduced Chemical Mechanism Development

The reduced NG chemical mechanism ARIES82 [48,49] (82 species and 518 reactions), which was generated by reducing ARAMCO 3.0 [96] using the Directed Relation Graph with Error Propagation (DRGEP) method and proven to successfully capture NG autoignition in both 0-D simulations of the RCM and 3-D simulations of an engine without NO_x [21, 22], was used as the base mechanism to subsequently incorporate NOx chemistry. The choice of starting from a reduced mechanism instead of reducing from a large, detailed mechanism came due to the fact that detailed mechanisms available at the time of conducting this study failed to accurately reproduce NG/NO_x IDTs as shown later in the manuscript, whereas ARIES82 accurately captured NG IDTs times (without NO_x species) and already had a suitable size for multi-dimensional engine simulations. The NO_x-containing ARIES82 mechanism, hereafter referred to as ARIES82NOx, was generated by incorporating the NO_x-chemistry subset from the mechanism developed by Dagaut

and Dayma [99] and the complete C_3+NO_x sub-mechanism from NUIG Mech1.1 [56, 100–107]. The final ARIES82NOx reduced mechanism incorporated 141 species and 783 reactions, an acceptable size for use in full-cycle ICE CFD simulations. Although the focus of this work is the ARIES82NOx mechanism, this mechanism was further reduced to improve computational efficiency of multi-dimensional engine simulations using the DRGEP method and sensitivity analysis, targeting a 1% deviation in IDTs predicted by ARIES82NOx. The resultant further reduced mechanism, referred to as ARIES50NOx, contains 50 species and 257 reactions.

6.3 Simulation Approach

The upgraded ARIES82NOx reduced mechanism was evaluated by comparing homogeneous IDT calculations for all three NG compositions, EGR compositions, and conditions tested in the previous RCM experimental campaign by Mohr et al. [48, 49]. Variable Volume 0-D Simulation toolbox available in CONVERGE version 3.0.25 [28] was used to perform all IDT calculations. The 'adiabatic core hypothesis' [108] was used to capture heat loss effects, and the procedures highlighted in [109] were used to calculate the time-dependent gas temperatures and the adiabatic core volume for use in IDT calculations. IDTs are subsequently plotted versus top dead center (TDC) temperatures for simplicity; however, the transient volume traces used to perform the IDT calculations and account for heat losses within the RCM experiments are available upon request. Ignition sensitivity analyses were performed with the ARIES82NOx mechanism using CONVERGE v3.0.25. IDT calculations and sensitivity analysis were also performed with the recently published NUIGMech1.2 detailed mechanism (2857 species, 11809 reactions) with updated CH_4-NO_x chemistry [98] for comparison.

CFR engine simulations were then performed using ARIES82NOx with CONVERGE version 2.4.35 [27]. Boundary conditions matched those reported in previously published engine tests, which explored the role of varying EGR rates and controlled EGAI on NG SI ICE efficiency [21, 22].

6.4 Results and Discussion

6.4.1 Homogeneous Ignition Delay

Figure 6.1 compares the calculated IDTs plotted versus the inverse of the TDC temperature to the previously published experimental data from Mohr et al. [48, 49]. Cases with and without reactive EGR (R-EGR) for all three NG compositions are shown. Included are calculations using the newly developed reduced mechanism, ARIES82NOx, ARIES82 [48, 49] (for the cases without EGR addition), and the state-of-the-art detailed mechanisms NUIG Mech1.1 and NUIG Mech1.2. While not shown, mixtures containing 10% and 30% R-EGR were simulated and compared to experimental data and used to assess mechanism errors. These intermediate R-EGR data did not show any unusual trends. As can be seen in Figure 6.1, the addition of R-EGR to the NG/oxidizer mixtures enhances the chemical reactivity and shortens the IDTs of all NG mixtures. ARIES82 agrees well with the data absent of EGR (and NO_x) whereas NUIG Mech1.1 shows the largest discrepancies for drier fuels in the presence of R-EGR , confirming our choice of using the ARIES82 mechanism as the foundation on which to add NO_x-chemistry. Results shown in Figure 6.1 of IDTs from NUIG Mech1.1 also show the large discrepancies for the Dry and Mid fuels with R-EGR addition. On the other hand, the results with the newly developed reduced mechanism, ARIES82NOx, show good agreement with the experimental data, demonstrating an average absolute error in calculated IDT of 19.1%. The average of the absolute errors found for the NUIG Mech1.2 was 18.5%, only slightly lower than that found with ARIES82NOx. Interestingly, ARIES82NOx and NUIG Mech1.2, generally followed similar trends when compared to the experimental data, for example, both calculating faster IDTs for the wet fuel than observed in the experiments. The general overlap between the reduced and detailed mechanism substantiates the robustness of the reduced mechanism in predicting NG IDTs in the presence of NO_x species.

6.4.2 Sensitivity Analysis

A sensitivity analysis was performed using ARIES82NOx and compared to that of NUIG Mech1.2 mechanism to (1) expand on a recently published study investigating CH_4–NO_x chem-

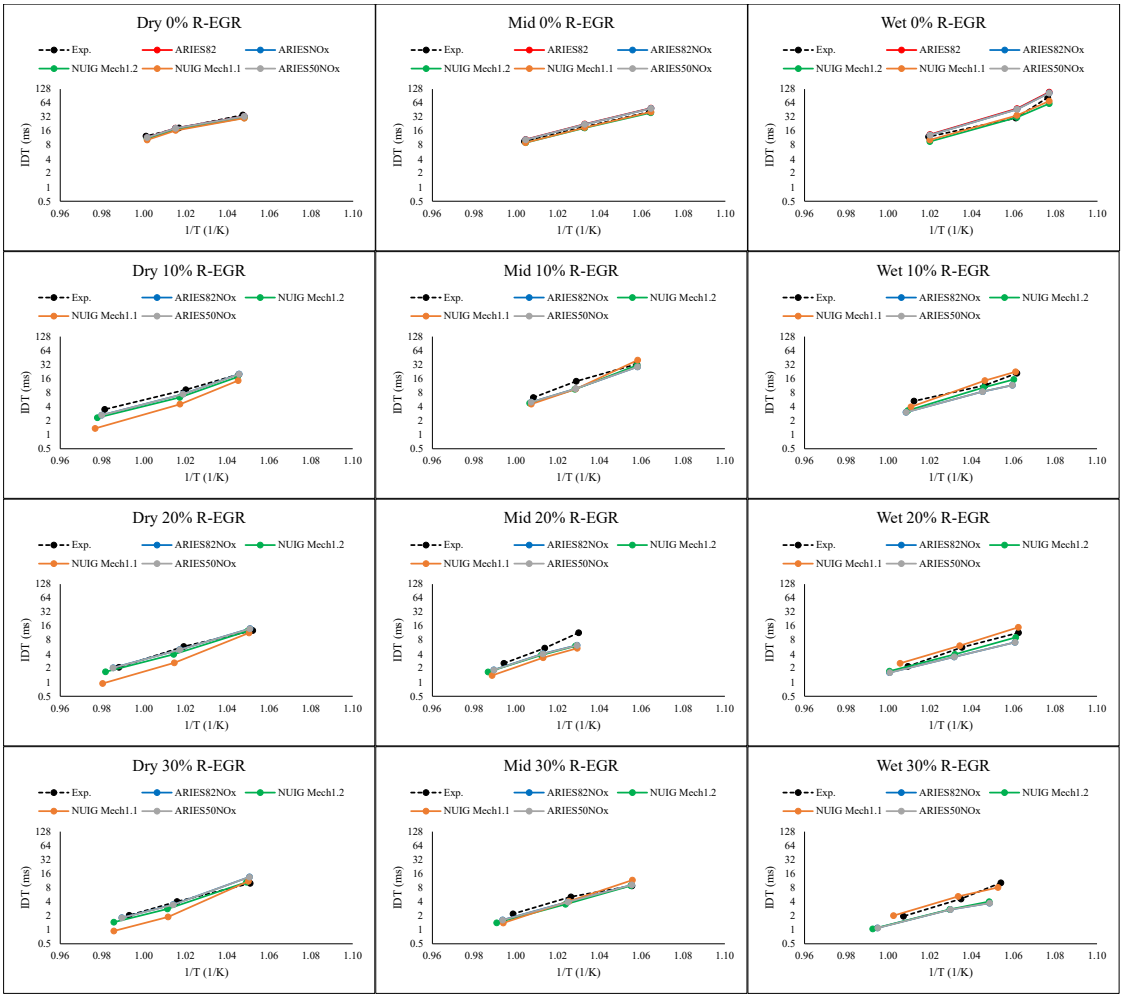

Figure 6.1: IDT calculation results for all fuels and R-EGR substitution rates.

istry by highlighting the important reactions when C_x-C_3 species are present and (2) to further validate the chemistry being captured by the reduced ARIES82NOx mechanism by comparing it to a state-of-the-art, detailed chemical kinetic mechanism [98].

Figures 6.2 and 6.3 compare the ten most ignition-promoting (6.2) and inhibiting (6.3) reactions in the ARIES82NOx mechanism to that of NUIG Mech1.2 for the wet fuel with a 30% R-EGR substitution rate at TDC temperature of 948 K and TDC pressure of 32 bar. These analyses were conducted to match the RCM conditions and thus were performed using the updated composition after the mixture was allowed to sit for 2 hours (i.e., with the majority of the NO being converted to NO_2). As shown in figures 6.2 and 6.3, although there are some slight differences in the normalized sensitivity coefficients between the detailed and reduced mechanism, as is expected due to the considerably different number of reactions in each, the leading reactions responsible for both promoting and inhibiting autoignition are essentially the same. As noted by Sahu et al. [98], CH_3+NO_2↔CH_3O+NO is the most important NG ignition promoting reaction as it feeds the main hydrocarbon oxidation pathway of methane with the production of methoxide (CH_3O). However, the competing reaction, which occurs with a third body to form nitromethane (CH_3NO_2), is an endothermic reaction that is very sensitive to reducing system reactivity and extending IDTs.

For NG fuels, there are several reactions with C_2-C_3 species that are important, including RH+NO_2↔R+HONO which enhance fuel consumption, and thus, autoignition. Additionally, for the wet fuels, NUIG Mech1.2 indicates that the formation of Nitroethane, $C_2H_5NO_2$, is important for inhibiting autoignition; however, this reaction does not appear in the ARIES82NOx sensitivity analysis since the sub-mechanism for the formation and oxidation of $C_2H_3NO_2$ is not present in the reduced mechanism. Its addition would result in a considerable number of added reactions without considerably improving the IDT calculation accuracy. Sensitivity analyses were also performed for the dry NG composition and as expected, showed less sensitivity for the C_2-C_3 reactions on ignition than the wet fuel. Interestingly, for these conditions, the sensitivity analyses do not indicate R1 nor NO_x obstruction on RO_1 chemistry as being important even for the wet NG fuels, despite their known sensitivity to the ignition of larger hydrocarbons.

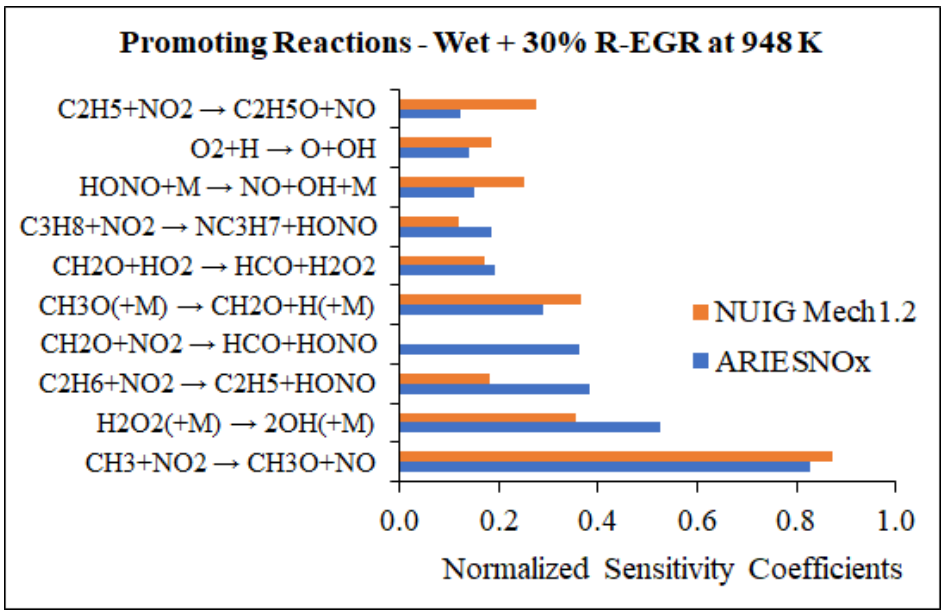

Figure 6.2: Sensitivity Analysis results for the Wet fuel with 30% R-EGR. Top most ignition-promoting reactions.

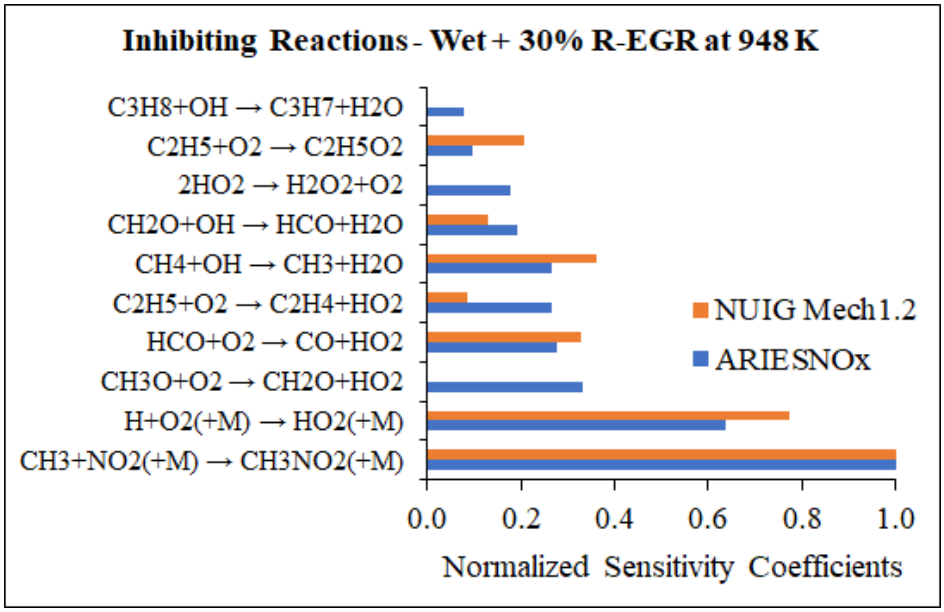

Figure 6.3: Sensitivity Analysis results for the Wet fuel with 30% R-EGR. Top most ignition-inhibiting reactions.

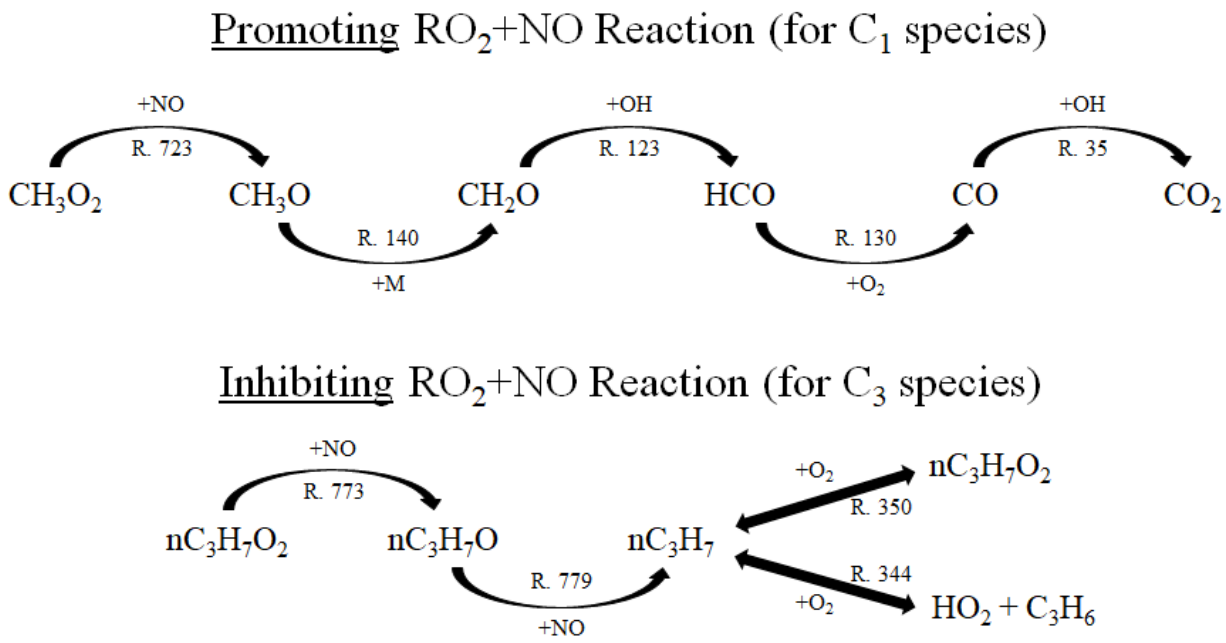

Figure 6.4: Reaction Pathway Flux analysis of the unaltered NO species in the EGR. Pathway flux highlights the different behavior of C_1 and C_3 species in the presence of NO.

A sensitivity analysis was also conducted using the unaffected composition (with all NO_x being comprised of NO) as would be seen in an engine. Interestingly, with NO present the analysis shows that RO_2+NO reactions promote autoignition for methyl fuel radicals; however, the same class of reactions for C_3 and larger HCs result in inhibition. This can be explained due to the fact that RO_2+NO will form RO+NO_2, which is CH_3O+NO_2 for C_1 species, feeding the main HC oxidation pathway, whereas, for C_3, the pathway will ultimately form an olefin+HO_2. The results of these pathway flux analyses are provided in Figure 6.4.

6.4.3 Laminar Flame Speed

As a further validation on the robustness of ARIES82NOx in capturing NG combustion, Laminar Flame Speed (S_L) calculations were performed and compared to ARAMCO 3.0, the mechanism used to generate S_L lookup tables in [21,22]. The excellent agreement of calculated S_L between the two mechanisms, shown on the overlapping curves of Figure 6.5, further validates its robustness and suitability to be used in NG engine simulations. Figure 6.6 shows additional S_L calculations

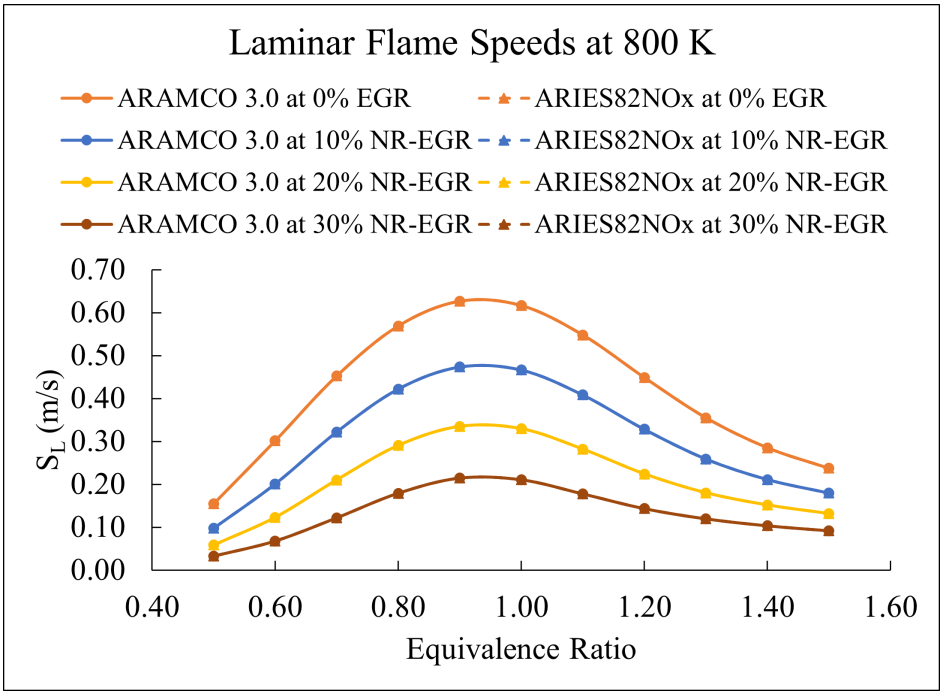

Figure 6.5: ARIES82NOx Laminar Flame Speed Comparison with ARAMCO 3.0. Overlapping lines show the excellent agreement with detailed mechanism calculations.

comparing the effect of R-EGR versus NR-EGR on S_L for stoichiometric Mid fuel combustion at varying temperatures and EGR ratios. Similarly to what was observed by Mohr et al., there is no noticeable difference between the effects of R-EGR and NR-EGR up to temperatures of 800 K; however, beyond 800 K the addition of R-EGR seems to enhance reactivity and increases S_L. The author speculates that, due to the higher temperatures, H-abstraction is increased which, combined with higher rates of NO formation, enhances reactivity. Additionally, higher temperatures result in greater Nitromethane (CH_3NO_2) dissociation, whose formation, as shown in Chapter 6.4.2, is the most inhibiting reaction. Figure 6.7 shows mass fraction distributions supporting this speculation; however, this topic needs further analysis .

6.5 Impact on Multi-Dimensional Engine Simulations

Multi-dimensional CFR engine CFD simulations were carried out with both the ARIES82 and ARIES82NOx mechanisms and compared to experiments to explore the impact of NO_x containing EGR on engine performance. The CFR engine CFD model developed in [21], calibrated using the

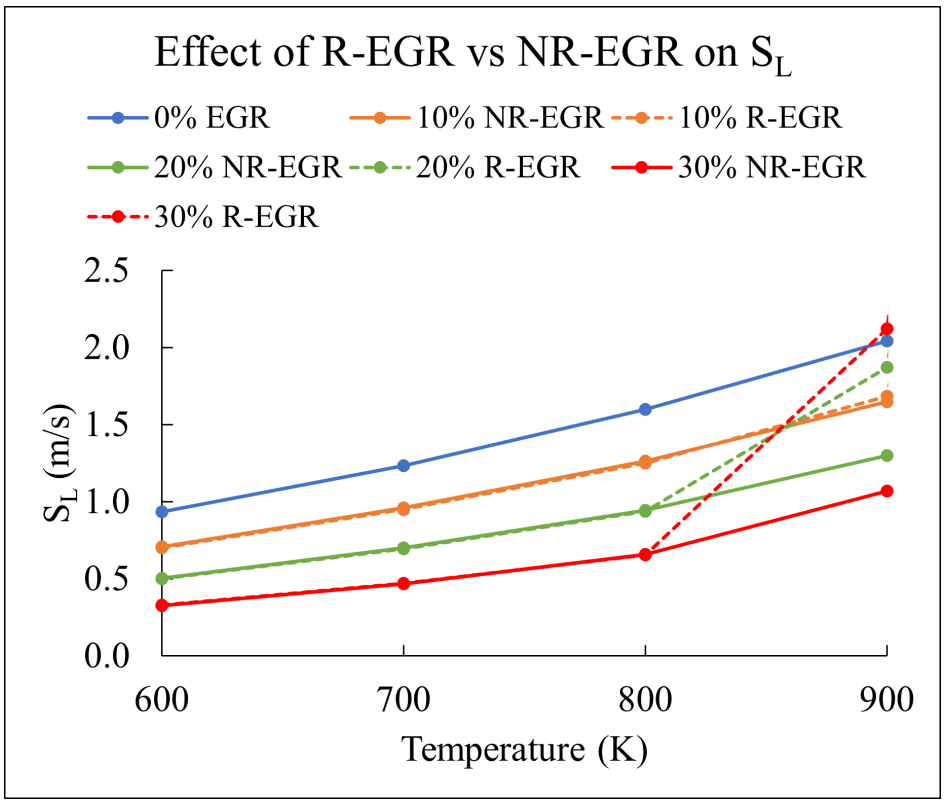

Figure 6.6: Effect of R-EGR versus NR-EGR on the Mid fuel's S_L. The same S_Ls are observed up to 800 K, agreeing with Mohr et al. results. S_Ls at higher temperatures need further analysis.

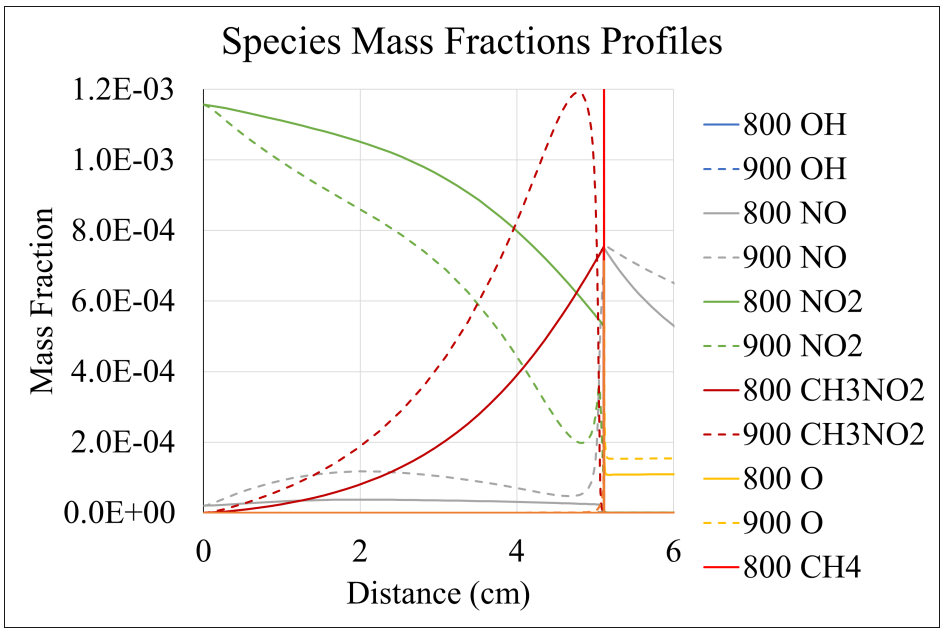

Figure 6.7: Species Mass Fraction profiles for S_L calculated at 800 K and 900 K using the Mid fuel and 30% R-EGR.

Table 6.3: EGR composition used in the CFD ICE simulations.

Species	Mol
CH_4 (THC)	0.09%
CO	0.06%
NO	0.14%
N_2	74.52%
CO_2	8.78%
H_2O	16.09%

ARIES82 mechanism, was used to analyze the effects of NO_x chemistry on the prediction of NG EGAI. In this work, the model (originally run with ARIES82, without NO_x) was rerun with the newly developed reduced mechanism, ARIES82NOx, while keeping the same boundary and initial conditions as well as the same calibration parameters, i.e., nothing was changed in the model except for the chemical mechanism and the EGR composition. The model was run with the intake, exhaust, and residual gas compositions updated to properly match the EGR composition that was experimentally observed, which contains NO and whose composition is shown in Table 6.3. Pipeline NG fuel with an MN of 69 from Table 4.2 was used. Due to the absence of NO_x species in the ARIES82 mechanism, only complete combustion products had been assumed for the EGR composition in the previous work [21] and in Chapter 5. Two operating points were simulated with varying compression ratios, Indicated Mean Effective Pressures (IMEP), EGR ratios, and CA50s, all at a constant engine speed of 900 RPM. This sweep of parameters led to various values of knock onset crank angle (KOCA), or the crank angle at which EGAI occurs, and fractional end-gas autoignition (f-EGAI), which we define as the fraction of the energy released from the EGAI event normalized by the total heat release . Table 6.4 summarizes the experimental engine conditions for the selected simulated cases. Additionally, 'Case 1' was also run using ARIES50NOx to assess its accuracy and computational performance in multi-dimensional engine simulation.

Figure 6.8 shows the simulated pressure (taken from a monitor point matching the position of the cylinder pressure transducer in the experiments) and the Apparent Heat Release Rate (AHRR)

Table 6.4: Simulated engine operating conditions.

Test Case	CR	RPM	IMEP (bar)	EGR	Lambda	CA50 (°aTDC)	P_{in} (bar)	T_{in} (°C)
Case 1	9.55	903	12	17%	1.00	12	1.6	61
Case 2	12.3	900	8	0%	1.01	12	0.9	60

profiles for the two simulated cases with the respective individually resolved cycle (gray) and a representative cycle (black), chosen to be the cycle with the maximum cylinder pressure closest to the average of all cycles maximum pressure, from the experimental data. These plots also include: (1) The original simulation data with ARIES82 without NO_x (red trace), (2) the simulation data using ARIES82NOx (blue trace), and (3) the simulation data using ARIES50NOx (green trace) with the experimentally observed EGR/residual gas composition. Also reflected are the measured and predicted KOCA noted by the overlaid symbols.

In both cases, the addition of NO_x chemistry advances the onset of EGAI and leads to a better representation of the engine pressure data, and more accurately reflects the onset of EGAI indicated in the AHRR plots. Table 6.5 shows a comparison of the mean experimental KOCAs of all 1000 engine cycles and the predicted/simulated KOCA using ARIES82 and ARIES82NOx. As can be clearly seen, the results for KOCA significantly improve, allowing the CFR engine simulations to match KOCA within 1.0 crank-angle degree (°CA) of the experimental values when using the ARIES82NOx mechanism. Although not shown in Table 6.5, ARIES50NOx predicts a KOCA 1.28 deg. earlier than the experimental mean. Important to notice is the direction of the change. Similar to the RCM experiments, the system's reactivity when utilizing ARIES82NOx is enhanced, and the onset of EGAI is advanced by over 2 °CA. 'Case 2' further highlights the importance of using a NOx-containing mechanism even in cases without EGR, where the NO_x formed during combustion remaining in the residual gas is sufficient to influence EGAI and improve the CFD simulations. Additionally, as observed by Mohr et al. and discussed in Chapter 6.4.3, NO_x species do not seem to influence flame propagation in the CFD simulations since the pressure traces and AHRR before the onset of EGAI nearly overlap. Lastly, Figure 6.8 also shows the excellent agreement

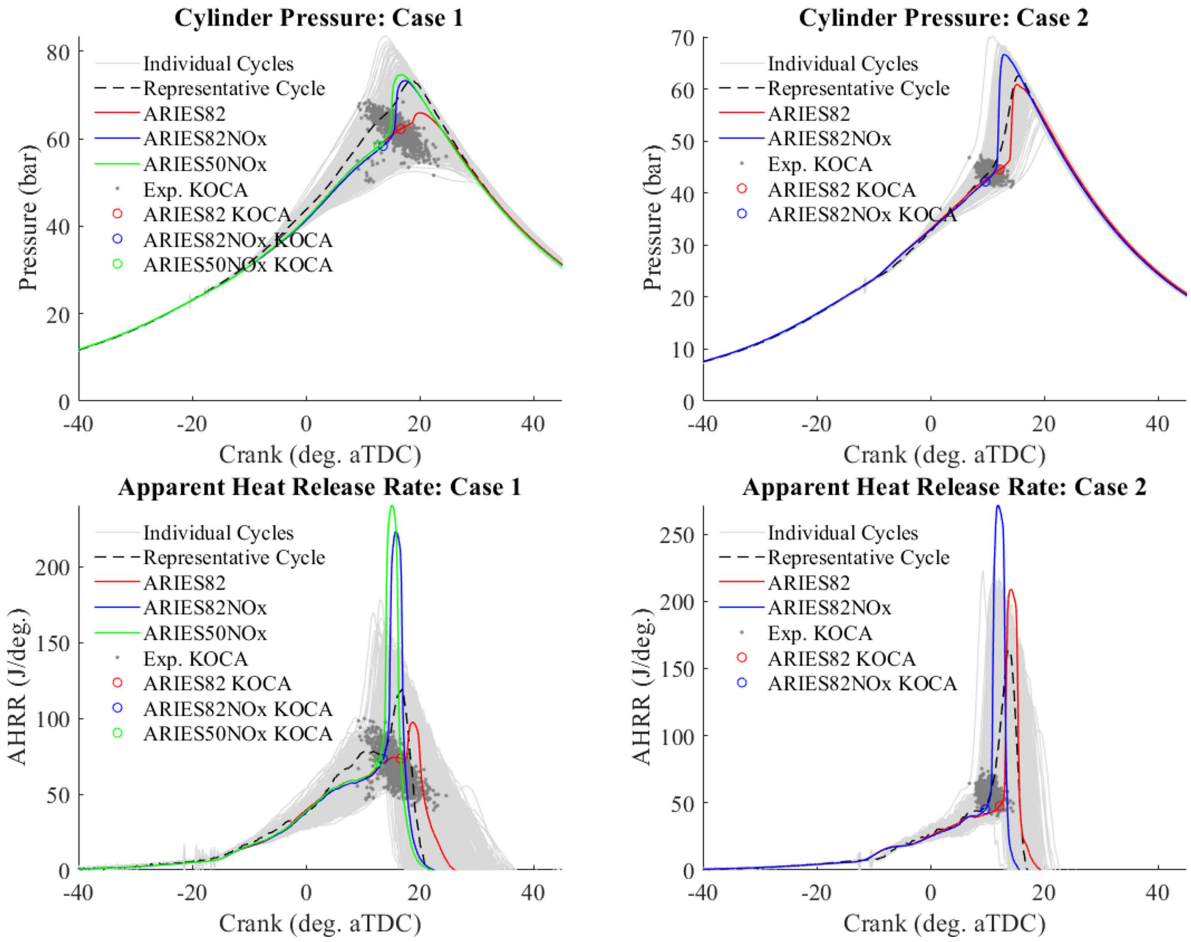

Figure 6.8: Cylinder pressure and AHRR with overlaid KOCA obtained from experimental data and CFD simulations using ARIES82 (red) and ARIES82NOx (blue).

Table 6.5: Simulated KOCA results comparison between ARIES82 and ARIES82NOx.

Test Case	Experimental	ARIES82	Error	ARIES82NOx	Error
Case 1	14.0	16.9	2.9	13.6	-0.4
Case 2	10.3	12.1	1.8	9.8	-0.5

of ARIES50NOx with experimental data, showcasing its accuracy, while reducing simulation time during the combustion section by nearly 50%.

Leveraging the CFD results and the predicted spatial distribution of CH_3, NO_2, NO, and OH concentrations at onset of EGAI (Figure 6.9, 'Case 2') one can visualize and better understand the mechanisms responsible for EGAI described in Chapter 6.4.2 that occur within the engine. Figure 6.9 illustrates that at the same location where the concentrations of CH_3 and NO_2 significantly decrease (top row), there is a corresponding increase in the concentrations of NO and OH, which is an indication of the reaction sequence CH_3+NO_2↔CH_3O+NO and NO+HO_2↔NO_2+OH, the importance of which was previously discussed with the homogeneous IDT results and in [98]. If the subsequent timesteps were to be plotted, the same pattern of lower concentrations of CH_3 and NO_2 corresponding to the locations of higher concentrations of NO and OH would continue and indicate the areas undergoing EGAI.

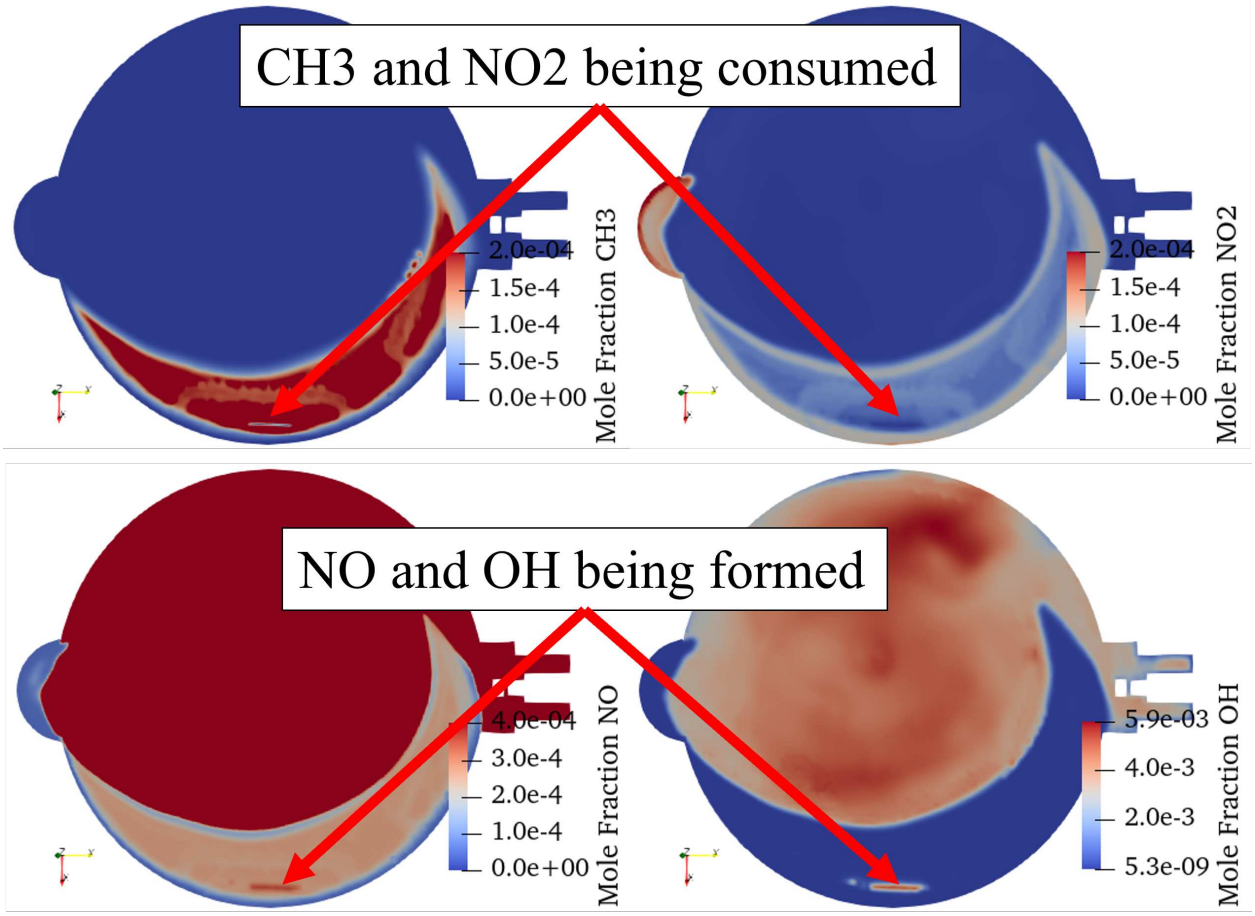

Figure 6.9: Spatial distribution of CH_3, NO_2, NO, and OH. Highlighted locations show the onset of EGAI.

Chapter 7

Role of Natural Gas Composition on EGAI

Having set the grounds for the proper detection and quantification of EGAI on engine test data (Chapter 4), the proper approach to computationally model NG EGAI (Chapter 5), and generated an accurate and suitably-sized chemical mechanism for multi-dimensional CFD engine models (Chapter 6), this chapter presents a study on how different NG compositions in the MN rating tests have the same or similar propensity to autoignite and, therefore, the same or similar f-EGAI. Additionally, a novel methodology to predict a fuel's propensity to knock, based on available engine data from either experiments or simulations, is presented. This methodology is based on the charge fraction undergoing autoignition, namely, the end-gas autoignition fraction (f-EGAI), and was developed based on first-order laminar flame speeds and ignition delay analysis combined with a 0-D homogeneous batch reactor model. This work has been published in the Proceedings of the Combustion Institute under the title "Investigation of the end-gas autoignition process in natural gas engines and evaluation of the methane number index" [22]

7.1 Modeling Approach

A closed homogeneous batch reactor in CHEMKIN [110] coupled with CFR engine test data is used to predict end-gas autoignition with an adiabatic assumption. The objective of these calculations is to interpret the MN rating test results and to explore the link between the fraction of the charge participating in the end-gas autoignition and KI. Measured cylinder pressure from -180° aTDC to 100° aTDC from the CFR engine is used as input. Charge temperature at Bottom Dead Center (BDC) is estimated with intake manifold temperature and coolant temperature. ARAMCO 3.0 [96] was used as the detailed chemical kinetics mechanism.

The volumetric heat release rate was retrieved from the results and the autoignition time, or the knock onset crank angle degree (KOCA), is determined at the location of the rapid heat release rate, i.e. where the derivative of the heat release rate reaches its maximum. Assuming the same

hardware such as combustion chamber geometry, compression ratio, and the same engine speed for similar turbulence intensity and flame speeds, the 0-D model can be used to capture changes in reactivity due to fuel type, charge strength, temperature, and pressure history. This is possible since turbulent combustion dominates in internal combustion engines and the turbulent intensity is dependent on engine configuration/geometry and operating conditions [29, 42].

The 0-D modeling approach described previously provides a means to link fuel ignition chemistry to KI if a pressure/temperature history is specified. Noting that the pressure/temperature history is largely dominated by the deflagration heat release, this approach requires the decoupling of the flame propagation, which can also impact the fraction of charge experiencing end-gas autoignition. Therefore, the multi-dimensional models presented in the previous chapter are also used here to further explain the MN results.

7.2 Methane Rating Test Results

Figure 7.1 shows the average MN measurements after three repetitions for each fuel for both naturally aspirated intake (1 atm) and boosted intake (1.3 bar) conditions. As noted by the narrow error bars in Figure 7.1, highly repeatable results (STD < 1.13 MN units) were achieved using the updated CFR engine and the FFT knock quantification procedure [12]. As can be seen, the experimentally determined and the calculated MN differ by a maximum of 2.42 MN units for the selected fuels, with the calculated MN showing higher results for all three fuels.

Figure 7.2 left compares the pressure traces for the dry and wet NG fuels to their (CH_4/H_2) reference fuels under the MN test conditions. These plots show a surprisingly good agreement between the NG and their reference fuels, indicating that, under the MN test conditions, the reference fuels mimic the behavior of the NG fuels. To determine how well the MN reference fuels predict the behavior of the NG fuels under more engine relevant conditions, comparative experiments were carried out at higher CR, BMEP, and CA50 for the Pipeline 1 NG and its reference fuel where a specified KI was no longer targeted. Figure 7.2 right shows the results for two engine relevant conditions where the previously mentioned parameters were kept constant between the

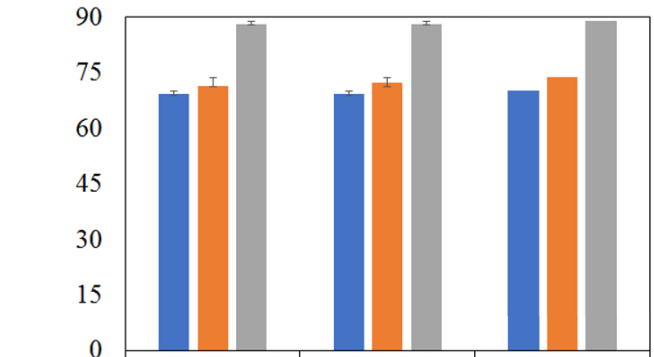

	Non-boosted (Measured)	Boosted (Measured)	Calculated
Wet	69.26	69.29	70.30
Pipeline	71.38	72.44	73.80
Dry	88.02	88.29	89.10

Figure 7.1: Methane Number Rating Test Results.

NG and the reference fuel. The CR was held constant at 7.41:1 and 12.14:1 for the non-knocking and knocking cases, respectively. BMEP and CA50 were held constant at 6 and 4 bar and 14° aTDC and 10° aTDC for the non-knocking and knocking cases, respectively. Again, a high level of agreement between the NG and its reference fuel cylinder pressures, heat release rates (HRR), and BMEP was observed.

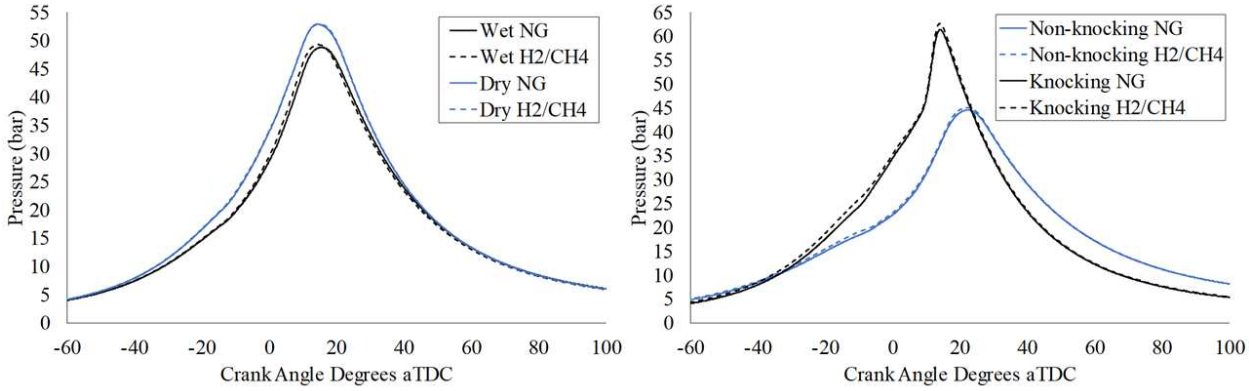

Figure 7.2: Experimental pressure traces under the MN rating test conditions (left) and under engine relevant conditions (right).

Table 7.1: LFS and AI at 55 bar and 900 K.

Fuel	LFS (cm/sec)	AI (ms)
Pipeline 2 NG	85.77	18.36
Pipeline 2 Ref	89.55	22.24
Wet NG	87.23	19.20
Wet Ref	92.73	22.16
Dry NG	76.41	26.13
Dry Ref	79.89	23.40
Pipeline 1 NG	84.53	18.13
Pipeline 1 Ref	92.84	22.16

7.3 Chemical and Thermodynamic Analysis

To help understand the engine results, Laminar Flame Speed (LFS) and Autoignition Interval (AI) analysis are used, where AI is defined as the time between the end of compression and the time of charge spontaneous ignition, differentiating from 'ignition delay' often used to describe the engine performance. Table 7.1 shows the results for LFS and AI calculated at 55 bar and 900 K. The LFS and AI analysis reveal that, although the reference fuels have higher flame speeds than the NG, they compare quite well (within 10% for all cases) explaining why we see nearly overlapping pressure traces between the NG and reference fuel mixtures. However, larger differences in the fuels' AI are noticed between the NG and their reference fuels, sometimes as high as 22%, which contradicts the MN test data showing similar measured KI. The dry NG is the only mixture that exhibits longer AI than its corresponding reference fuel, likely due to the long AI of methane, which makes up 97.03 vol% of the dry NG fuel versus 89.1 vol% in the reference fuel.

Since the charge composition of each test case is very different, their specific heat ratio (gamma) and polytropic compressed end-gas temperature will also be different, even if their pressure curves are very similar. Figure 7.3 shows gamma and end-gas temperature comparison between the Pipeline 2 NG and its reference fuel. The reference fuel has higher gamma values than the NG over the entire compression event. For similar pressures as encountered in the CFR engine operating with the Pipeline 2 NG, the end-gas temperature is higher for the reference fuel by approximately

15 K as shown in Figure 7.3, which results in a 14% lower AI relative to the NG fuel, reversing the trend seen in Table 7.1. The same results were seen for the wet and, to a lesser extent, the dry fuel. Therefore, this difference in compressed temperature can influence ignition chemistry and must be accounted for during the calculation of the AI.

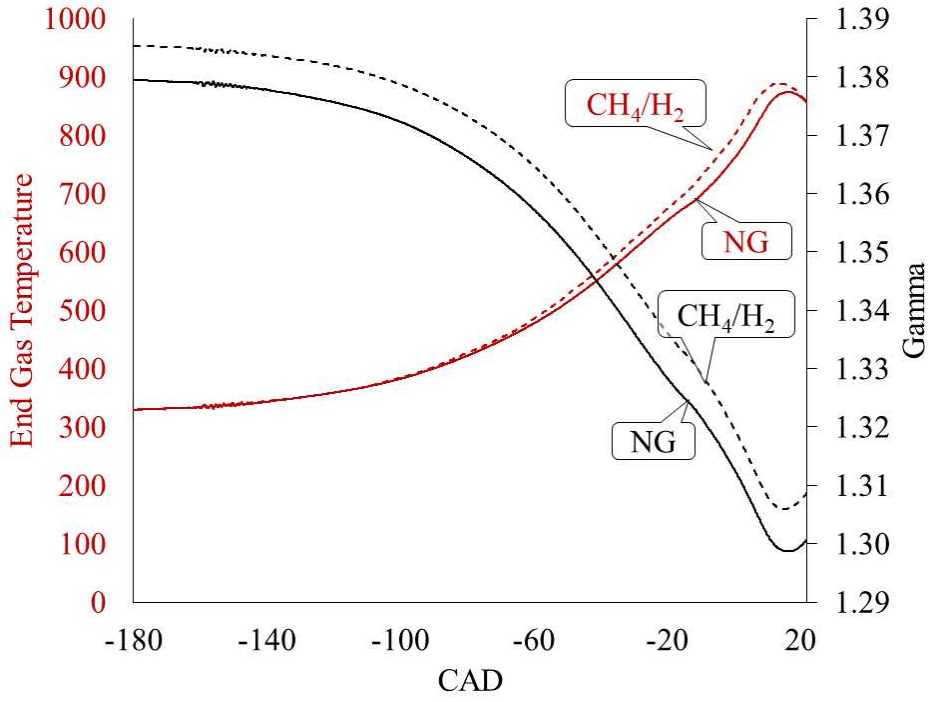

Figure 7.3: CH_4/H_2 has higher γ and higher end-gas temperature for similar pressure ratio.

Previous research has used the fraction of the end-gas undergoing autoignition (f-EGAI) to characterize knock [24]. Since the KI, for a given engine geometry and test condition, is proportional f-EGAI, as shown in reference [24] and the previous chapter, both tested NG and its reference fuel should have similar f-EGAI since their KIs are similar.

In order to quantify the f-EGAI for the different fuels, CHEMKIN 0-D homogeneous ignition delay calculations described in Section 7.1 were used. Table 7.2 summarizes the f-EGAI results, determined from the autoignition CAD, for all the NG fuels and their reference mixtures under the MN test conditions. Despite the differences in the AI between the NG and their reference fuels, once incorporating the effects of different gammas and, consequently, different compressed end-

Table 7.2: Experimental and 0-D modeling KOCA and f-EGAI results.

Fuel	Exp. KI (kPa^2)	Exp. Knock Onset	0-D Knock Onset CAD	0-D f-EGAI
Pipeline 2 NG	49.45	12.84°	17.77°	17.8%
Pipeline 2 Ref	50.57	12.12°	16.57°	19.0%
Wet NG	51.30	13.1°	17.17°	13.4°
Wet Ref	49.90	12.14°	16.40°	12.3%
Dry NG	55.40	13.23°	17.22°	14.8%
Dry Ref	55.10	13.06°	17.20°	13.6%
Pipeline 1 NG	1000	10.40°	12.13°	42.88%
Pipeline 1 Ref	1300	8.92°	8.62°	50.85%

gas temperatures during the induction period before the end-gas autoignition, combined with the competition between LFS and AI as is done in the 0-D ignition delay calculations, almost the same f-EGAI and KOCA between the NG and their reference fuels are observed. This corresponds well with the overlapping pressure traces shown earlier in Figure 7.2 and is confirmed by the fact that the NG and the reference fuels both targeted a KI value of 50 kPa^2.

As a result of the heavy-knock conditions experienced in the engine-relevant test conditions (Figure 7.2 right), the 0-D modeling approach could not be used since the input pressure curves are strongly influenced by the presence of knock. In this case, CFD was used to predict the end-gas autoignition dynamics. These results are shown in Table 7.2 for the Pipeline 1 NG and compared to experimental results (last two lines). In this case, the 3-D CFD model ignition predictions show very similar KOCA for the two fuels, confirming the observations seen in the measured pressure trace Figure 7.2 (right). Furthermore, the 3-D CFD modeling indicates a larger f-EGAI for the reference fuel, which again corresponds to the higher measured KI.

Figure 7.4 shows 3-D CFD results for in-cylinder temperature, Turbulent Flame Speeds (TFS), and the in-cylinder pressure for the Pipeline 2 NG (top) and its reference CH_4/H_2 fuel (bottom) at the knock onset for the Pipeline 2 reference fuel. As can be seen in Figure 7.4, the unburned-gas temperature is higher for the reference fuel as predicted by the 0-D modeling. The figures in the middle column show that TFS for both fuels are very similar, confirming the assumption that

turbulent intensity is strongly dependent on engine configuration and operating conditions allowing the use of the 0-D model to quickly assess a fuel's propensity to knock under the same engine hardware and operating conditions. Lastly, the CFD model also predicts the knock onset earlier for the reference fuel, confirming the 0-D model predictions and the experimental observations as can be seen in Table 7.2.

Additionally, CFD results agree well with trends observed in the experiments and 0-D modeling where higher KI cases had larger f-EGAI and earlier knock onset. For the Pipeline 2 NG and its reference fuel shown in Figure 7.4, knock onset CAD was 18.2° and 16.1° aTDC and f-EGAI 2.42% and 5.43% for the Pipeline 2 NG and its reference fuel, respectively. Again, the earlier onset of knock led to higher KI and, consequently, higher f-EGAI.

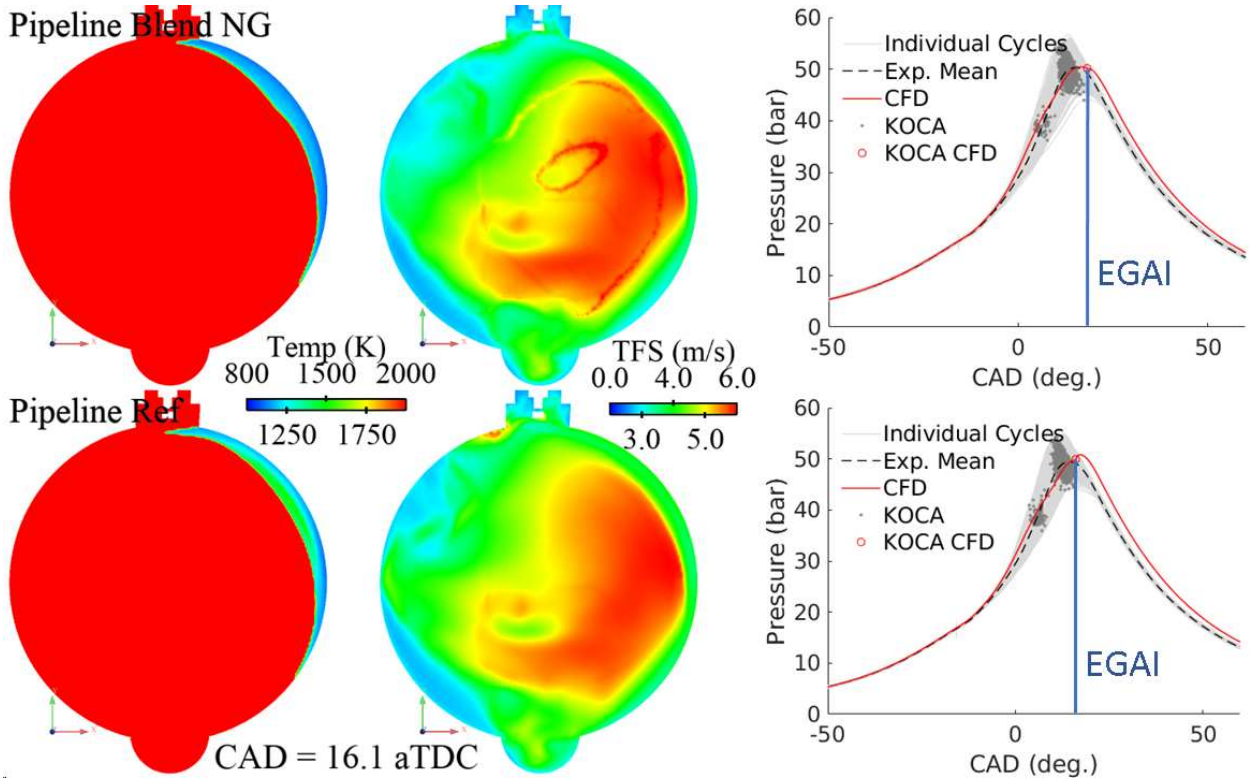

Figure 7.4: NG and Reference Blend spatial temperature and TFS distribution (left and middle). Corresponding in-cylinder pressures (right).

7.4 Discussion and Conclusions

The in-cylinder combustion behavior between the NG fuels and their MN reference CH_4/H_2 blends were remarkably similar even when tested at more extreme engine-like conditions and varying knock intensity levels. The LFS for the NG and their reference blends are very similar; however, differences in the AI were noticed, with the wetter NG fuels exhibiting shorter AI than their reference blends.

With slightly faster LFS and longer ignition delays for the same temperature and pressure, the MN reference CH_4/H_2 fuel should theoretically have a lower propensity to autoignite than its NG counterpart, as all of the unburned gas would be consumed before any autoignition could take place. However, the remarkably similar autoignition behavior can be explained by understanding that turbulent combustion dominates under engine conditions, eliminating the differences in flame propagation, and that the MN reference fuels have higher specific heats ratio, causing unburned gas temperatures to be higher, which, in turn, shortens AI.

The outcomes here confirm again that the KI is linked to the f-EGAI and, when coupled with a 0-D homogeneous batch reactor simulation, might allow one to quickly predict the propensity of a fuel to knock if reliable engine specific information (e.g., pressure/temperature history) from an experiment or CFD simulation is available to be used as an input.

Chapter 8

Piston Design Optimization to Realize Ultra-High Efficiency in SI NG Engines

Section 2.5 presented a literature review on in-cylinder flow parameters, how the flow parameters affect engine performance, and recent studies on piston design to improve SI NG engine efficiencies. Chapters 5 through 7 presented the work done on investigating appropriate methods for NG EGAI modeling and prediction. This chapter changes the focus to the application of this acquired knowledge to optimize the piston bowl shape of the Cummins X15 engine, and thus, its combustion chamber design, in order to find an optimum piston design for the realization of a SI NG combustion with C-EGAI operation at higher CRs in HD engines. This optimization study was divided into two phases. The first phase entailed the use of a calibrated 0D/1D GT-Power model of the Cummins X15 engine to find an optimum compression ratio. The second phase used a calibrated 3D CFD model of the same engine to optimize the piston bowl shape at the optimum CR to increase thermal efficiency. Since EGAI can enhance thermal efficiency, all the optimization work was done at an EGAI-free operation to ensure that the gains in efficiency are solely due to the different piston designs and not due to the presence of EGAI.

8.1 0D/1D GT-Power Models

A single-cylinder, 0D/1D GT-Power Three Pressure Analysis (TPA) model, similarly as created for the CFR engine in Chapter 5, was created to serve as the baseline for the calibration of a predictive Spark Ignition Turbulent Combustion (SITurb) GT-Power model described in Section 2.3.1. Figure 8.1 shows the Cummins X15 GT-Power TPA model created. As is the case in the experimental work, only cylinder number 6 is fired (single-cylinder operation). Table 8.1a shows the natural gas fuel composition used in the model calibration and CR optimization. Table 8.1b shows the range of engine operating conditions used in the model calibration.

GT-Power TPA model results show an excellent agreement with experimental data. As shown in figures 8.2 and 8.3, fuel flow rates match within 2% of experimental data, gIMEP and BMEP within 5%, which result in a Brake Thermal Efficiency (BTE) agreement within $1\%_{pt}$.

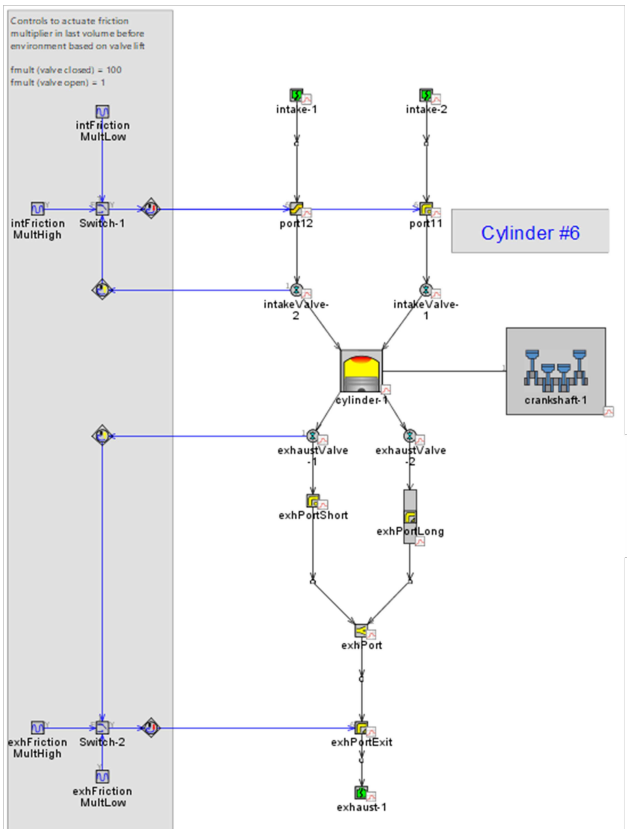

Figure 8.1: 0D/1D GT-Power model of the Cumming X15 Single-Cylinder engine.

Having a calibrated TPA model, a predictive GT-Power model using the SI Turbulent Flame Combustion Model (SITurb) described in Section 2.3.1 can be calibrated. This is done by inputting laminar flame speed information for the fuel being used, which, in this case, was done by using the correlation developed by [33], and then calibrating model constants to correlate laminar flame speeds, turbulent flame speeds, and burn rate. This predictive 0D/1D model is based on the work of [29]. For more detailed information on the calibration procedure and SI Turbulent Flame Combustion Model development, the interested reader is referred to [26, 29].

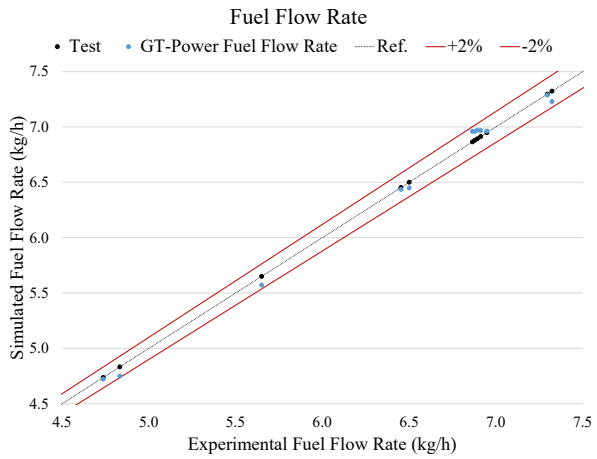

(a) Simulated versus experimental fuel flow rate.

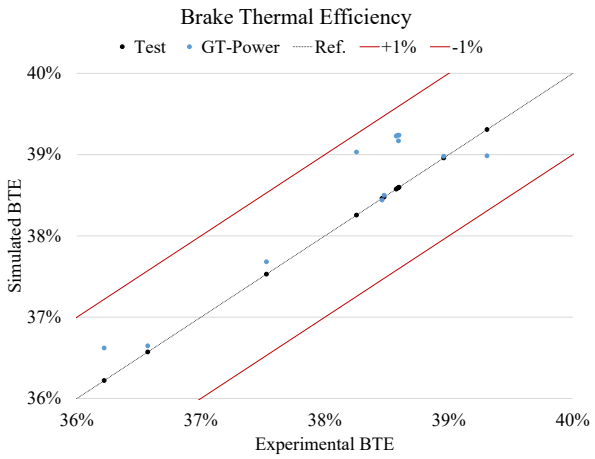

(b) Simulated versus experimental BTE.

Figure 8.2: Simulated versus Experimental Fuel Flow Rates (a) and Brake Thermal Efficiency (b) for the Cummins X15 GT-Power model.

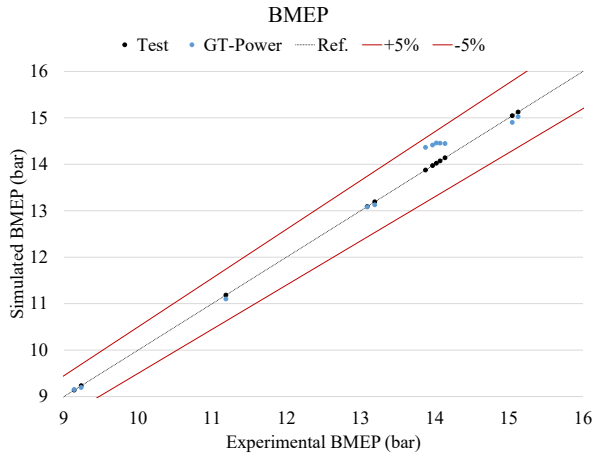

(a) Simulated versus experimental BMEP.

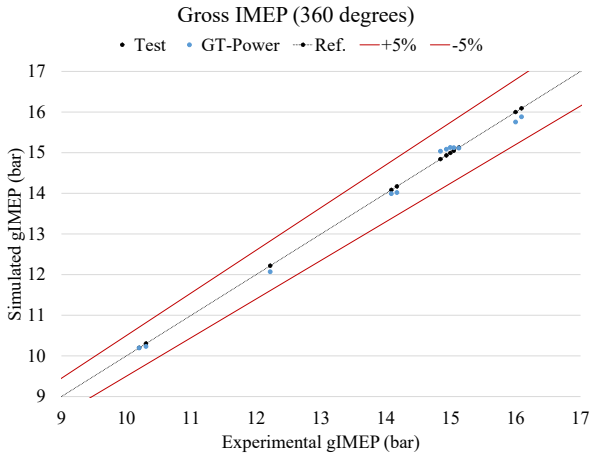

(b) Simulated versus experimental gIMEP.

Figure 8.3: Simulated versus Experimental BMEP (a) and gIMEP (b) for the Cummins X15 GT-Power model.

Species	Mol
CH_4	86.56%
C_2H_6	9.85%
C_3H_8	1.24%
C_4H_{10}	0.18%
C_5H_{12}	0.05%
C_6H_{14}	0.01%
N_2	0.37%
CO_2	1.60%
MN	77.6

(a) NG composition used in the Cummins X15 model Calibration.

Parameter	Min	Max
IMEP (bar)	10	14
BMEP (bar)	9	16
CA50 (deg.)	1.4	9.7
EGR	0.0%	0.0%

(b) Range of engine operating conditions used in the Cummins X15 GT-Power model calibration.

Table 8.1: Fuel composition and engine operating conditions used in the Cummins X15 GT-Power model calibration.

Similar to the GT-Power TPA model results, the predictive GT-Power SITurb model shows an excellent agreement in predicting the engine behavior for the known operating conditions. Cylinder pressures, fuel flow rates, gIMEP, and BMEP have excellent agreement with experimental data. BTE has a slightly higher error when compared to the agreement achieved with the TPA model, however, all cases still agree within 1%pts, showing that the model is suitable for predictions of the engine behavior due to changes in operating conditions. Figure 8.5 shows the excellent agreement achieved with the SITurb model compared to experimental data.

In these models, the Livengood-Wu integral was used to track the occurrence of EGAI. The induction-time correlation developed by Gamma Technologies [26] was employed and calibrated using a GRG Nonlinear solver to match the ignition delays predicted by the ARIES82 mechanism developed by Mohr et al [48, 49]. Equation 8.1 is the induction time correlation used in the simulations where M1 was calibrated to 13.80538 and M2 = 1.22764. MN is the fuel Methane Number and Fuel, O_2, and Diluent are the fuel, oxygen, and diluent concentrations, respectively. Figure 8.6 shows the good agreement between the induction times predicted by the calibrated correlation and the ARIES82 mechanism.

IMEP 10 bar; CA50 at 6 deg. aTDC

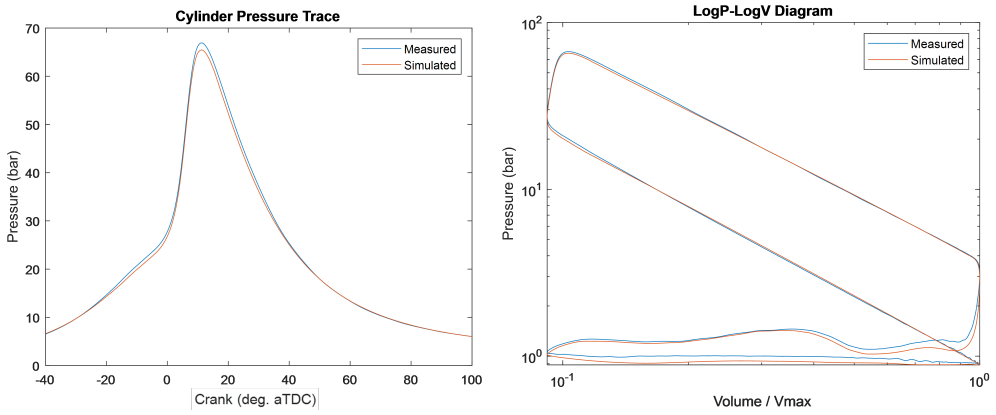

Figure 8.4: Cylinder pressure (left) and LogP-LogV (right) diagram for a selected operating condition showing the model's excellent agreement with experimental data.

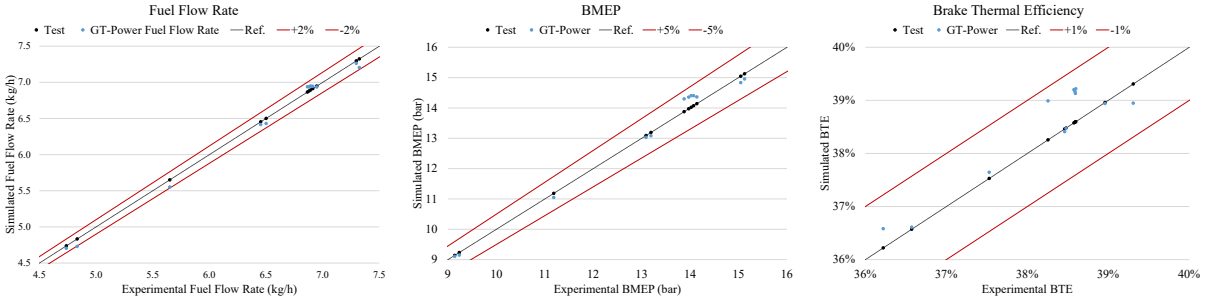

(a) Predicted fuel flow rates. **(b)** Predicted BMEP. **(c)** Predicted BTE.

Figure 8.5: Predicted versus experimental fuel flow rate, BMEP, and BTE. Slightly higher errors in the SITurb model, however, an excellent agreement with experimental data is still observed.

$$\tau = M1 * 1.9858 * 10^{-9} * \exp\frac{18659}{M2 * T} * (\frac{MN}{100})^{0.978} * Fuel^{-0.578} * {O_2}^{-0.28} * Diluent^{0.03} \quad (8.1)$$

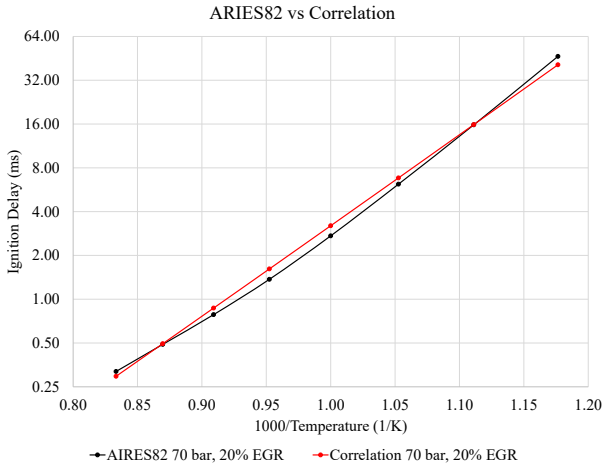

Figure 8.6: Calibrated induction-time correlation shows good agreement with ARIES82 mechanism predictions.

8.2 Compression Ratio Optimization

In order to find an optimum CR at which a knock-free operation may still be possible, the predictive GT-Power SITurb model was used to simulate the Cummins X15 engine under various operating conditions and CRs. A total of 935 simulations were run varying CR (11-20:1), IMEP (10-24 bar), CA50 (5-10 deg. aTDC), and EGR (0-25%). The goal of this operating condition and CR sweep was to find the optimum CR at an optimum operating condition to be further enhanced by the piston shape optimization task using a 3D CFD model. Results from this optimization procedure show that CRs between 14:1 and 16:1 are the most promising in terms of achieving higher BTEs. This can be seen by plotting BTE versus CR and looking at the cases that achieved at least 44% BTE, which was the original Cummuns engine's BTE when operating with diesel. As

Table 8.2: Highest efficiency operating conditions for each EGR percentage.

EGR	CR	IMEP (bar)	CA50 (deg. aTDC)	BTE	PCP (bar)	Case #
0%	13	20	10	41.8%	126.28	703
10%	14	20	10	43.2%	129.66	830
15%	14	22	10	44.1%	140.60	911
20%	15	22	10	45.0%	146.73	921
25%	15	22	10	45.6%	147.19	930

it can be seen in Figure 8.7, these CRs have the highest number of operating conditions at or above 44% BTE, with the CR 15:1 showing the highest BTE of all cases at 45.6%.

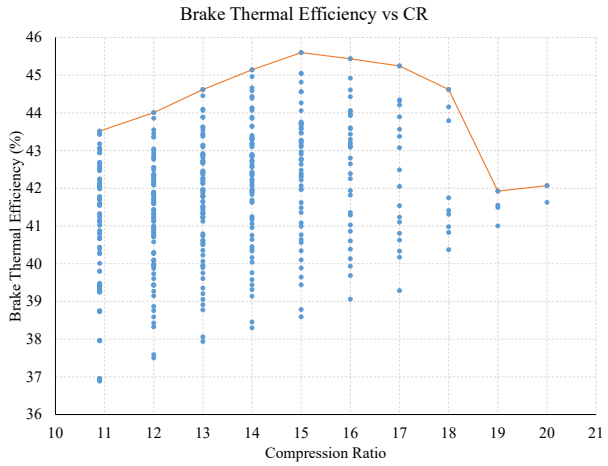

Figure 8.7: BTE versus CR. CRs between 14:1 and 16:1 are the most promising options for further optimization.

Another way to look at the results is by searching for the highest BTE at a given EGR ratio and knock-free operation. This information is shown in Table 8.2. As expected, increasing EGR percentage allows the use of higher CRs and results in higher BTE. Since this project aims at using EGR as means of controlling EGAI, CRs of 14:1 and 15:1 were selected for further analysis.

Finally, looking at the spread of operating conditions that achieved a BTE of 44% or higher, as shown in Table 8.3, it becomes clear that the CR 14:1 is the most promising option to be further optimized. The reasons being are the good spread of IMEP levels, CA50, and the widest spread of

Table 8.3: Knock-free Cases at BTE 44% or Higher.

CR	Min IMEP	Max IMEP	Min CA50	Max CA50	Min EGR	Max EGR	# of Cases
12	22	22	10	10	25%	25%	1
13	20	22	8	10	20%	25%	4
14	18	22	8	10	15%	25%	9
15	18	22	8	10	20%	25%	8
16	15	20	7	10	20%	25%	7
17	15	18	8	10	25%	25%	4
18	15	15	10	10	20%	25%	2

EGR percentages. These factors lead to the highest number of operating conditions achieving or exceeding a BTE of 44% among all CRs. Therefore, the final optimized piston had a CR of 14:1.

8.3 Piston Design Optimization

Having selected the optimum CR, 22 different piston designs were simulated. Ten piston designs were based on the baseline piston initially installed on the Cummins X15 engine and are shown in figures 8.8 and 8.9. The other 12 designs were generated only for exploration purposes since they could not be manufactured out of the available blank pistons and used the initially developed CFD model that had not been validated against experimental data. Although with limitations, these exploratory designs allowed for comparative investigation of tumble and swirl motion effects on engine performance and helped inform the design of the final piston designs. These 12 designs and the exploratory study results are included in Appendix A.

The goal of the manufacturable designs shown in Figure 8.8 were to explore how the different squish area ratios would influence the flow field and its effects on the combustion parameters, which ultimately affect thermal efficiency. The different designs were generated by varying the Squish Area Ratio (Squish Area/Bore Area) and adjusting the bowl depth to maintain constant CR. The literature review presented in Section 2.5 and the exploratory simulations shown in Appendix A have shown that a smoother transition between the bowl and squish regions is beneficial for engine thermal efficiency due to faster flame propagation towards the squish region. Addition-

ally, the simulations in Appendix A have also shown that tumble flow is beneficial for thermal efficiency due to the decreased ignition delay, faster flame propagation away from the spark plug, and reduced heat losses. For these reasons, the 'non-standard' designs in Figure 8.9 were generated to explore their suitability and effects on engine thermal efficiency.

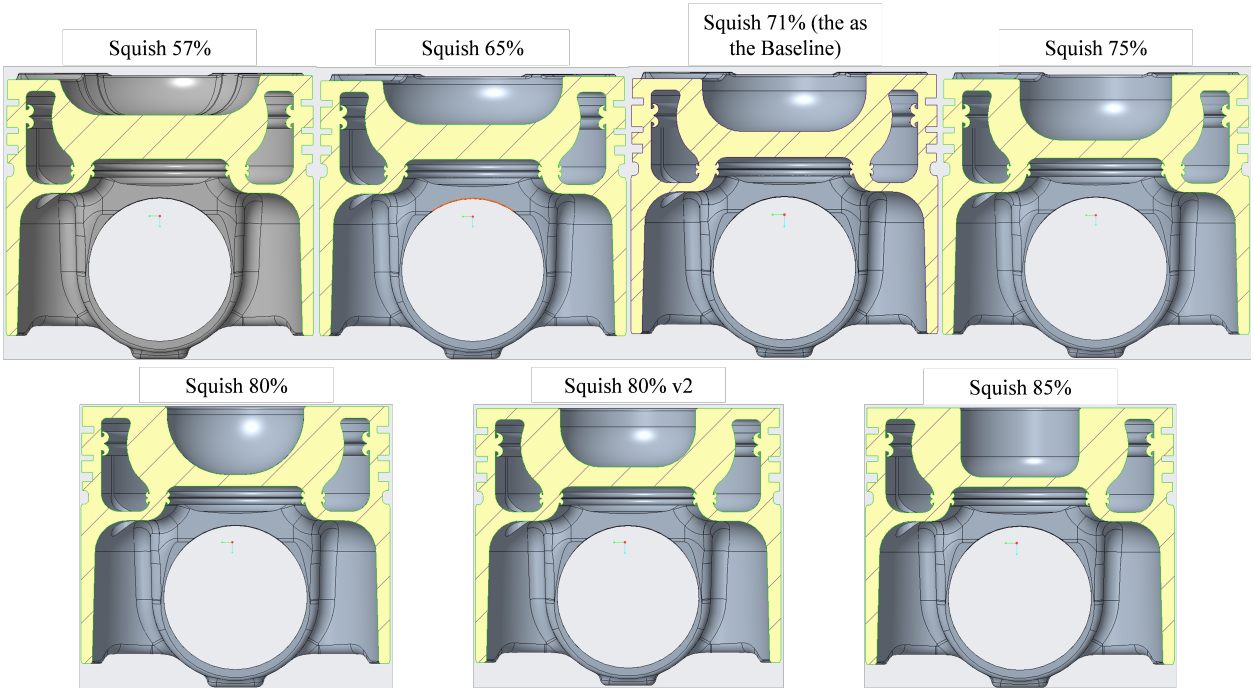

Figure 8.8: Piston designs varying squish areas to achieve various levels of turbulence and surface areas.

An analysis of the results is provided in Table 8.4 to assess combustion, engine performance, emissions, heat losses, and knock propensity of each design. The Ignition Delay shown in the table is the crank-angle degree interval between sparking time and CA10, Burn Duration is the crank-angle interval between CA10 to CA90, and UHC is the sum of the exhaust concentrations of CH_4, C_2H_6, and C_3H_8. Maximum Amplitude of Pressure Oscillations (MAPO) and the Knock Intensity (KI) metrics are used to characterize the knock propensity of each design. The table is color-coded in a way that the greenest parameters are the best-performing designs, whereas the reddest are the worst-performing ones.

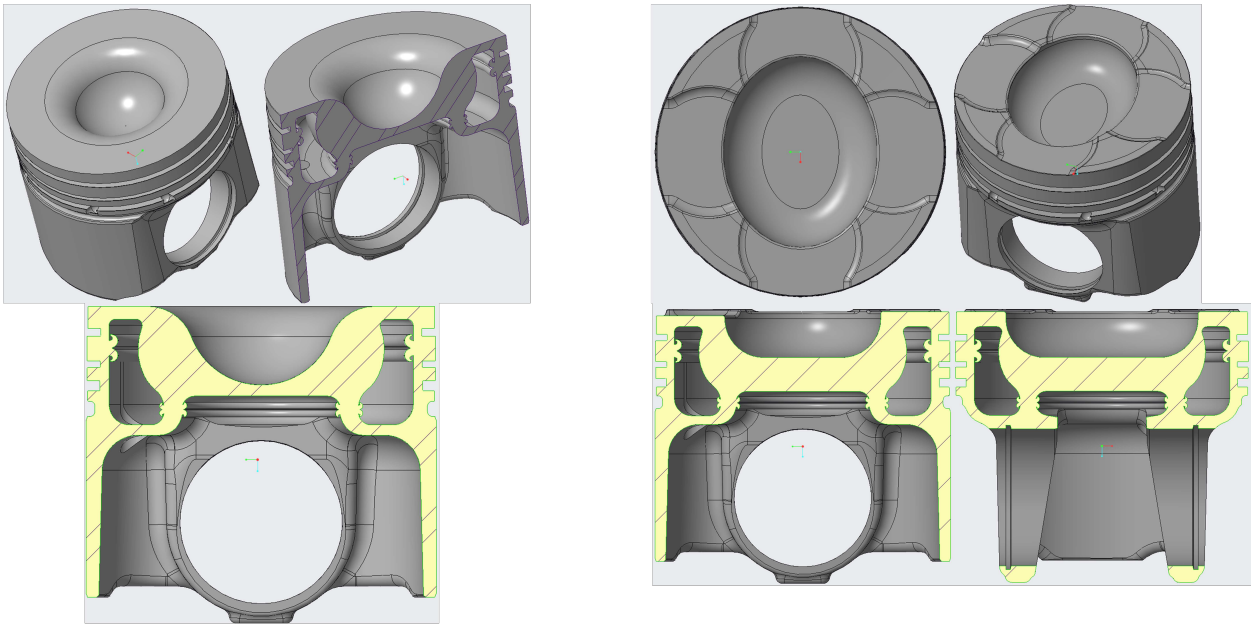

Squish 57% Bowl

Squish 65% and 71% Tumble

Figure 8.9: 'Non-standard' piston designs to explore different bowl-to-squish region transition (left, Squish 57% Bowl) and tumble-inducing bowl (right, Squish 65% and 71% Tumble).

Table 8.4: CFD simulation results for various combustion, engine performance, emissions, heat loss, and knock propensity. The greenest colors highlight the best performing designs, whereas the reddest colors highlight the worst performing designs.

Simulation	PCP (bar)	CA10 (deg.)	CA50 (deg.)	CA90 (deg.)	Burn Duration (deg.)	Ign. Delay (deg.)	nIMEP (bar)	ηi	BMEP (bar)	BTE	UHC at 360° in the Exh (PPM)	Piston Heat Loss (J)	Total Heat Loss (J)	MAPO (bar)	KI (bar-deg)
Squish 57% Bowl	136.5	5.0	10.3	17.60	12.60	5.00	18.38	47.9%	17.63	45.9%	6745.12	372.50	671.26	0.0217526	0.2695
Squish Area 57%	134.7	6.4	10.2	18.30	11.90	4.90	17.95	46.7%	17.20	44.8%	6425.65	410.76	679.08	0.0353934	0.3883
Squish Area 65%	135.6	5.5	9.9	18.71	13.19	5.01	18.20	47.4%	17.45	45.5%	7134.61	443.14	713.30	0.0288914	0.3251
Squish Area 65% Tumble	135.2	5.3	9.8	18.51	13.20	4.91	18.37	47.8%	17.62	45.9%	7481.03	443.11	711.41	0.0238123	0.2831
Squish Area 71%	132.8	5.9	10.0	18.71	12.81	5.11	18.15	47.3%	17.40	45.4%	7481.59	447.09	716.49	0.0161354	0.2149
Squish Area 71% Tumble	135.2	5.8	10.2	18.71	12.91	4.80	18.15	47.3%	17.40	45.4%	7864.64	451.64	720.84	0.0263352	0.3331
Squish Area 75%	135.1	6.2	10.0	18.60	12.39	5.21	18.06	47.1%	17.31	45.2%	8409.79	467.10	735.91	0.0246660	0.2835
Squish Area 80%	132.2	4.9	10.8	18.20	13.29	6.91	18.33	47.8%	17.58	45.8%	6143.52	403.64	689.26	0.0389801	0.4711
Squish Area 80% Version 1	136.9	5.5	10.5	17.51	12.00	5.01	18.20	47.4%	17.45	45.5%	7301.63	391.65	655.89	0.0323578	0.2656
Squish Area 85%	136.7	5.7	10.1	17.42	11.71	5.71	18.16	47.3%	17.41	45.4%	7270.04	461.49	771.86	0.0263861	0.3704

As it is clear in Table 8.4, piston design Squish 57% Bowl offers the highest ITE since it has the lowest piston heat loss. Design Squish Area 80% also yields similar BTE, however with much longer ignition delay, which can negatively affect ignitability, and with a much higher propensity to knock, which gives less room for the Controlled End-Gas Autoignition (C-EGAI) operation. However, all piston designs offer very similar thermal efficiencies, differing only in the decimals, varying among them their ignitability and tendency to knock. Since the goal of this optimization was to find an optimum performing piston design and since all designs offer very similar thermal efficiencies, the design with the largest room for a C-EGAI operation was chosen to allow for a safe engine operation under EGAI conditions. Therefore, the design "Squish Area 71%" has been selected to be manufactured and installed in the Cummins X15 engine for testing. Additionally, the results obtained from these CFD simulations were obtained at the same engine operating conditions, thus, if one were to rerun the same simulations but at a Knock-Limited Spark Advance (KLSA), design "Squish Area 71%" would give the best performance since it would allow the most advanced spark timing to be used.

Finally, the piston was installed and tested by the student responsible for engine testing, demonstrating a BTE of 45.3% while operating under SI NG C-EGAI combustion mode.

Chapter 9

Controlled EGAI and Mechanisms for High Efficiency in SI NG Engines

To finalize the study of modeling and control of NG EGAI, the optimized piston developed in Chapter 8 was installed in the Cummins X15 engine and tested. This piston allowed the single-cylinder Cummins X15 engine to achieve diesel-like efficiencies, i.e., $\geq$44% BTE, when operating with NG under a C-EGAI mode.

In this chapter, the test data gathered with the optimized piston was used to further validate and update the GT-Power models developed in Chapter 8. The goal of having updated GT-Power models was to perform a complete study, for a wide range of operating conditions, on the influence of EGAI, i.e., f-EGAI, on engine efficiency and on the mechanisms by which EGAI enhances thermal efficiency and can be achieved.

9.1 0D/1D GT-Power Model Tuning

As described in Section 2.3.1 and in the SITurb model reference works by Hires et al. [29], Blizard et al. [30], and Morel et al. [31], the SITurb model calibration constants are engine-hardware specific since turbulence is primarily generated by the engine geometry, i.e., intake system, piston, head, etc. Thus, to accurately capture the Cummins X15 engine behavior with the new optimized piston, the SITurb model developed in Chapter 8 needs to be updated for the new piston design. Additionally, the intake system (manifold and runners) as well as the knock sub-models have been updated to (1) ensure flow rates are accurately predicted for a wide variety of operating conditions, thus accurately predicting thermal efficiencies, and (2) ensure combustion, especially EGAI, is accurately captured to allow for the study of EGAI using 0D/1D models.

The intake system was expanded to model in detail every runner of every cylinder in the engine even though only cylinder #6 is firing. This modification ensured pressure oscillations in the intake

system were accurately captured and would respond to changes in operating conditions, especially to varying boost pressures. Figure 9.1 shows the complete, updated GT-Power model map for the single-cylinder Cummins X15 engine.

The SITurb combustion model was also updated to accurately capture flame propagation and EGAI of any NG composition without the need to recalibrate the induction time correlation, Equation 8.1. The latter goal was achieved by employing the chemical mechanism developed in Chapter 6. Due to its small size and accuracy in capturing NG IDTs, ARIES50NOx was implemented to reduce the computational expense incurred on the GT-Power model by these upgrades.

The process by which the SITurb model with chemical kinetics is (re)calibrated is a crucial factor in determining the success or failure of the model calibration process. Since there are nuances of the model calibration that are important to be followed, the list below provides a step-by-step description of the model update process to ensure accurate flow rates, flame propagation, and EGAI detection.

1. Match flow rates, IMEPs and onset of EGAI. Using the GT-Power TPA model, adjust the heat transfer multipliers in the intake system and cylinder to match flow rates, IMEPs, and onsets of EGAI. Heat transfer in the intake system primarily affects flow rates by changing the charge density; however, since the intake runners are at the head temperature, and in-cylinder heat transfer affects IMEP and EGAI, these two parameters should be adjusted simultaneously. Differently than when using an induction time correlation, when using chemical kinetics, the only tunable factor to calibrate EGAI is the in-cylinder heat transfer multiplier.

2. Update SITurb model. Using knock-free conditions, including knock-limited ones, calibrate model constants discussed in Section 2.3.1 for the new piston. These constants aim at capturing flame propagation and thus, using autoigniting cases would lead to incorrect results.

3. Fine tune EGAI detection with SITurb. With the calibrated SITurb model, fine tune the intake and in-cylinder heat transfer multipliers to match flow rates, IMEPs, and onset of EGAI.

An important caveat during this process is to select a cycle that is the most representative for each operating condition since averaged pressure traces smooth out the changes in slopes due to EGAI, making it difficult to accurately model EGAI onset. Additionally, since at any given engine condition some cycles might undergo EGAI and some might not, calibrating the SITurb and knock sub-models in GT-Power to the average of EGAI onset and f-EGAI of all cycles can also yield misleading results. In this work, a cost function, Equation 9.1, was utilized to select the most representative cycle for each operating condition. The most representative cycle was selected as the cycle where the cost function was minimum.

$$CF_i = \frac{|\frac{dP}{dt}_{max,i} - \frac{dP}{dt}_{max,avg}|}{|\frac{dP}{dt}_{max,avg}|} + \frac{|f_{EGAI,i} - f_{EGAI,avg}|}{f_{EGAI,avg}} + \frac{|MAPO_i - MAPO_{avg}|}{MAPO_{avg}} + \frac{|IMEP_i - IMEP_{avg}|}{IMEP_{avg}} + \frac{|CA50_i - CA50_{avg}|}{CA50_{avg}} \tag{9.1}$$

Model results after the updates remained in good agreement with experimental data. Figure 9.2 shows the agreement in Fuel Power, a proxy for fuel flow rate, and onset of EGAI obtained with both GT-Power TPA and SITurb models. Slightly larger discrepancies are observed in the onset of EGAI using chemical kinetics compared to using the induction time correction from Equation 8.1 due to the greater sensitivity to variations in the boundary conditions and end-gas temperature. However, model agreement is still satisfactory with most cases agreeing within ± 3 crank-angle degrees. Agreement in nIMEP, calculated over the entire cycle, and nITE also remained excellent, with most cases witin $\pm 1\%$ of experimental values. Figure 9.3 shows the results for (a) nIMEP and (b) ITE. Model fine tuning was performed using 10 different operating conditions, reserving the remaining operating conditions for model validation.

9.2 C-EGAI Under a Wide Range of Operating Conditions

The updated GT-Power SITurb model presented in Section 9.1 was utilized to study the behavior of EGAI, marked by f-EGAI, under a wide range of engine operating conditions. This study

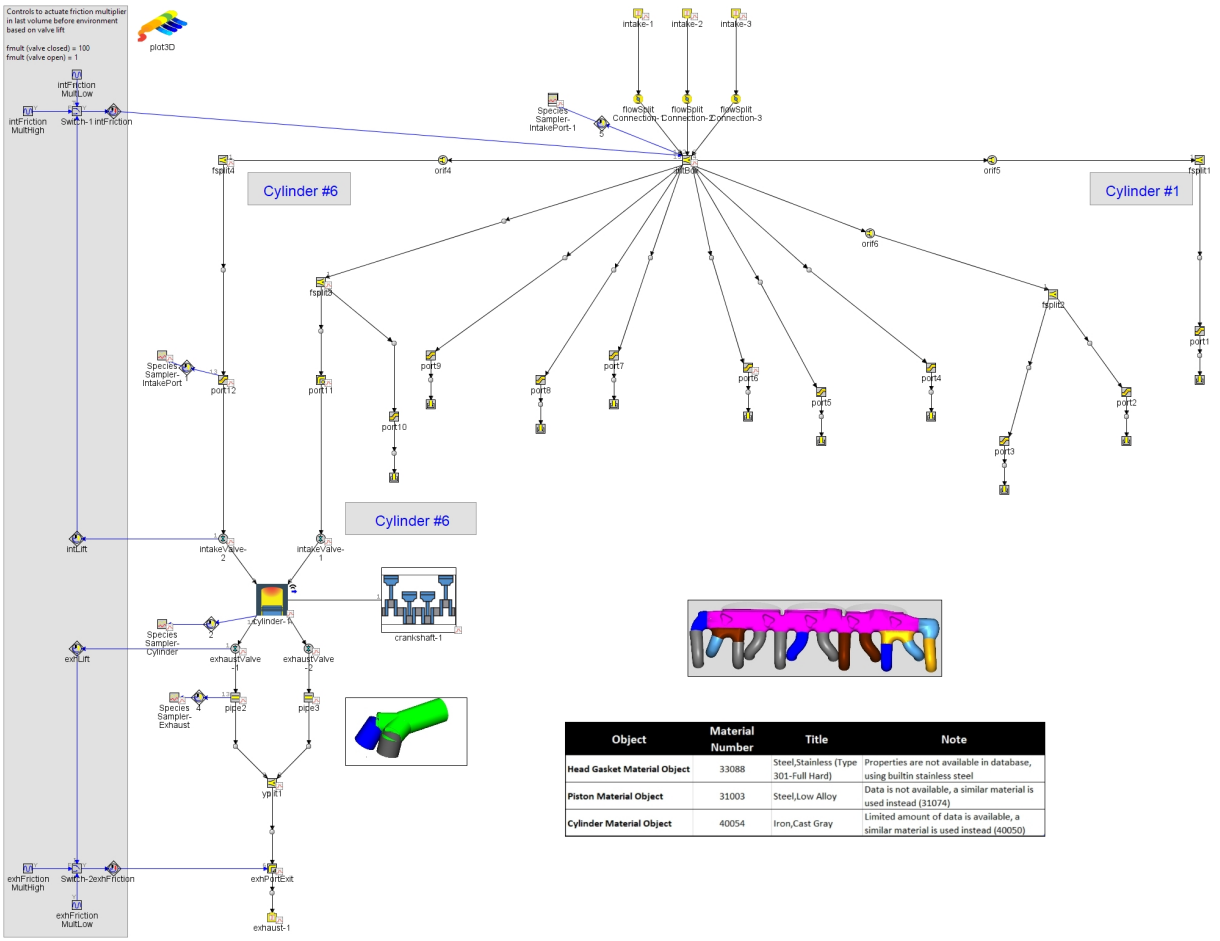

Figure 9.1: Updated Cummins X15 GT-Power Model. Expanded intake system ensures flow rates are accurately captured and correctly respond to changing boost pressures.

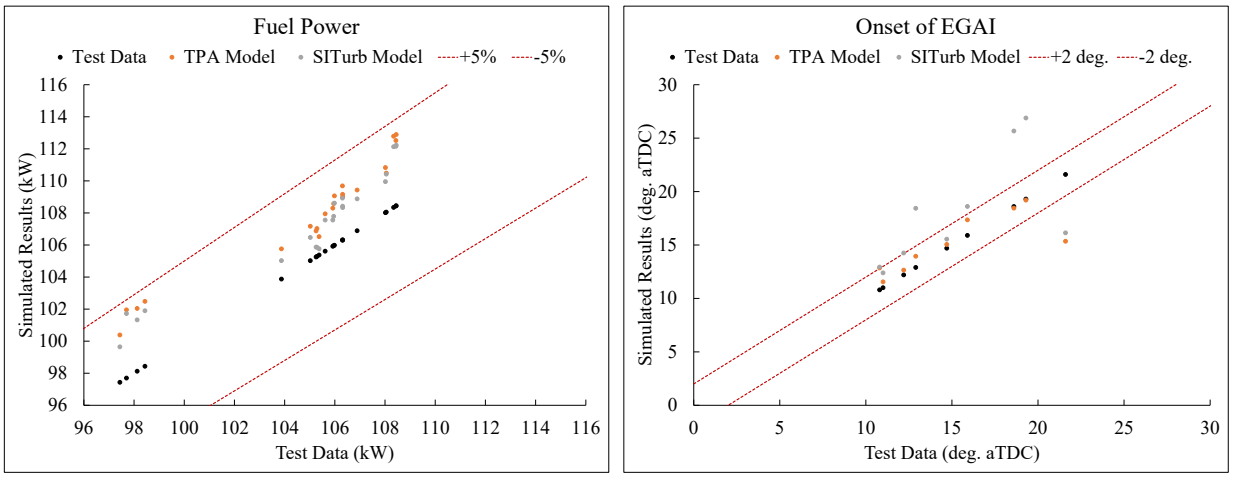

(a) Predicted Fuel Power.

(b) Predicted Onset of EGAI

Figure 9.2: Predicted versus experimental for (a) Fuel Power and (b) Onset of EGAI. Good agreement with experimental data is again observed. Data shown contains both calibration and validation cases.

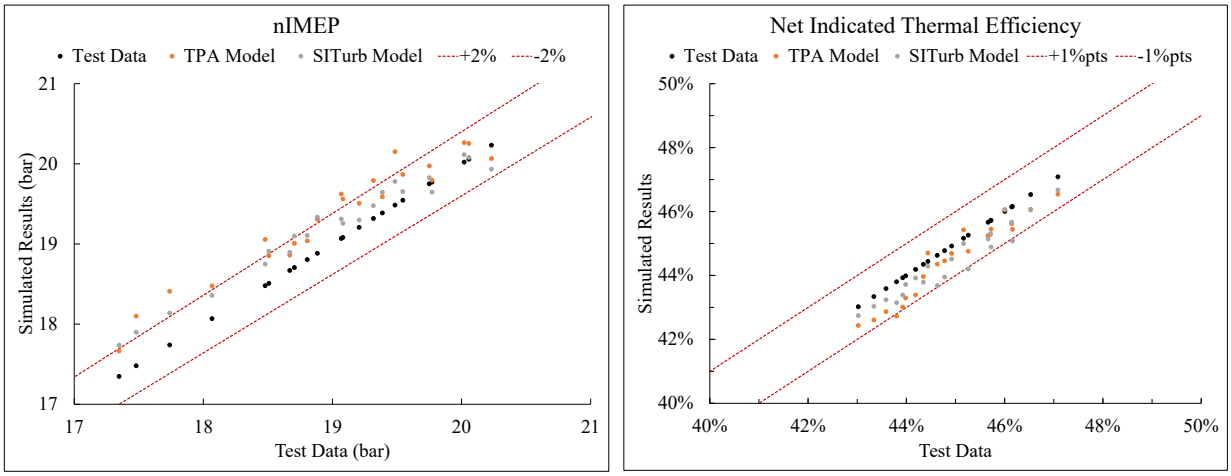

(a) Predicted nIMEP.

(b) Predicted nITE

Figure 9.3: Predicted versus experimental for (a) nIMEP and (b) nITE. Excellent agreement with experimental data showcases the model suitability to perform studies for a wide range of operating conditions.

Table 9.1: Engine control variables' ranges and increments used in the DOE for EGAI study.

Variable	Min	Max	Increments
EGR Ratio	0%	40%	10%
Engine Speed (RPM)	1000	1800	200
CA50 (deg. aTDC)	5.0	12.0	1.0
IMP (bar)	1.5	2.5	0.1

aimed at assessing the influence of EGAI on the engine's thermal efficiency and how it responds to engine control variables (e.g., boost pressure, engine speed, CA50, EGR, etc.). Additionally, the study aimed at understanding the mechanisms responsible for triggering EGAI and increasing thermal efficiency under a C-EGAI operation. To perform this study, a Design of Experiments (DOE) was set up in the GT-Power environment varying the main control parameters analyzed so far: EGR, Engine Speed, CA50, and Intake Manifold Pressure (IMP). Table 9.1 shows the variables' ranges and increments. Fuel composition and lambda were left out of the DOE to allow for a realizable DOE size; however, their influence was also analyzed with a reduced number of cases and is presented later in this chapter. A total of 2200 different operating conditions were simulated in approximately 21 hours using a standard workstation.

Before discussing simulation results, it is important to highlight the model limitations. As it currently stands, the predictive SITurb GT-Power model cannot predict misfire or structural damage to the engine hardware. Therefore, engineering judgement has been used to select realizable operating conditions. To this goal, it was assumed that conditions with a burn duration (10-90%) longer than 30 crank-angle degrees have misfired. Similarly, conditions with a maximum cylinder pressure greater than 200 bar have been assumed too dangerous for the engine hardware integrity and discarded from the analysis.

The first important outcome of this study is to confirm that EGAI can actually improve thermal efficiency as seen in previous studies (Chapter 5) with a more limited dataset. Figure 9.4 shows Brake Thermal Efficiency (BTE) of all realizable operating conditions plotted versus f-EGAI. As is clearly seen on the plot, increasing f-EGAI, thus the EGAI contribution to the combustion event, increases BTE for all simulated EGR ratios. In fact, an operation at $\geq$44% is possible for all EGR ratios experiencing EGAI. Also clear on Figure 9.4 is the well-known, strong influence of EGR on BTE. Interesting to note on Figure 9.4 that EGR ratio still has a stronger influence on BTE than f-EGAI. By analyzing Figure 9.4 it is clear that an increase of $10\%_{\text{abs}}$ in EGR ratio results in an $1\%_{\text{abs}}$ increase in BTE, whereas, to achieve the same BTE increase, f-EGAI needs to be increased by 20-30$\%_{\text{abs}}$.

Since BTE can be considerably enhanced by increasing f-EGAI, it is of interest to see the influence of engine control variables on f-EGAI. Figure 9.5 shows the trends of f-EGAI as a function of EGR ratio, Engine Speed, IMP, and CA50. The trends in Figure 9.5 follows the expected behavior of EGAI discussed in Chapter 5, where increasing EGR ratio and retarding CA50 decreases f-EGAI by lowering the end-gas temperature. Increasing engine speed also decreases f-EGAI due to reduced induction time for autoignition to take place. On the other hand, increasing IMP leads to higher f-EGAI as shown in Figure 9.5b. Although these trends are expected from well-documented knowledge, knowing them is important for engine-specific combustion optimization. For example, Figure 9.5a shows that f-EGAI has its highest intensity at 0% EGR and decreases with increasing EGR ratio; however, Figure 9.5a also shows that the number of realizable operating conditions at

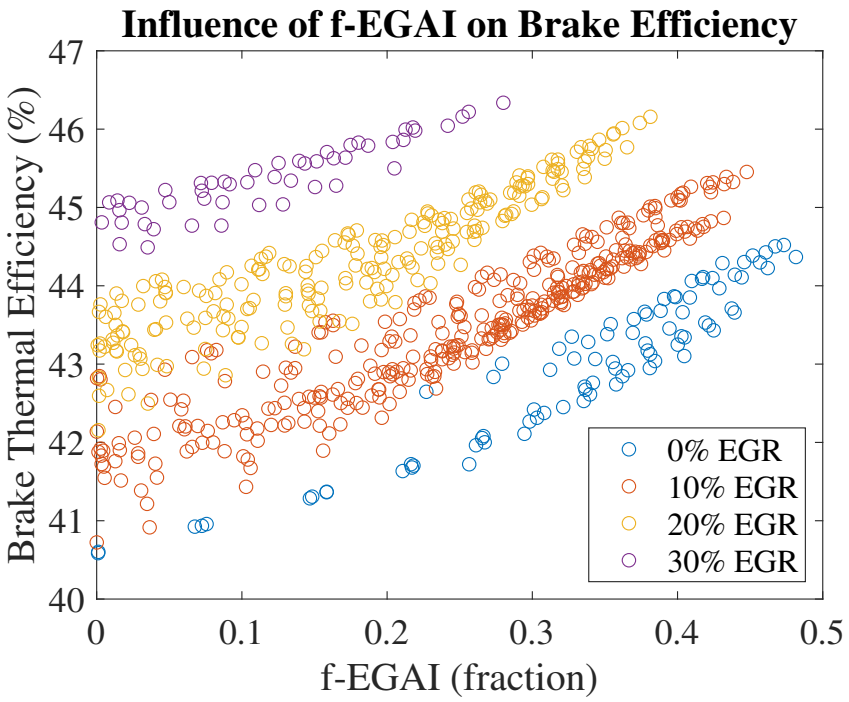

Figure 9.4: Effect of f-EGAI and EGR on BTE. Increasing f-EGAI clearly allows improved BTE; however, BTE still seems to be more sensitivity to EGR ratio.

0% EGR is smaller than that of larger EGR ratios, implying that an operation with constant EGR flow is likely necessary. Additionally, Figure 9.6a shows the influence of Lambda (λ), defined as the inverse of equivalence ratio (ϕ), and intake charge temperature on f-EGAI when targeting the same power density (i.e., BMEP), CA50, EGR ratio, and engine speed. As a result, IMP was increased with increasing λ. Contrary to expected, increasing λ while keeping the same BMEP increases f-EGAI. The reason for this increase lies in the fact that, to keep a constant BMEP, IMP has to be increased, which increases in-cylinder pressures and temperatures. Figure 9.6c shows the expected behavior of decreasing f-EGAI with leaner λ when a constant IMP is targeted instead of BMEP. Also shown in Figure 9.6a is the expected strong influence of intake charge temperature on f-EGAI, where a 10 °C increase in intake charge temperature can increase f-EGAI in approximately $5\%_{\text{abs}}$. Finally, Figure 9.6b shows there is an opportunity to improve BTE even further by operating at leaner conditions while maintaining a C-EGAI combustion. By leaning λ from 1.0 to 1.4-1.6, BTE approached the 50% BTE mark.

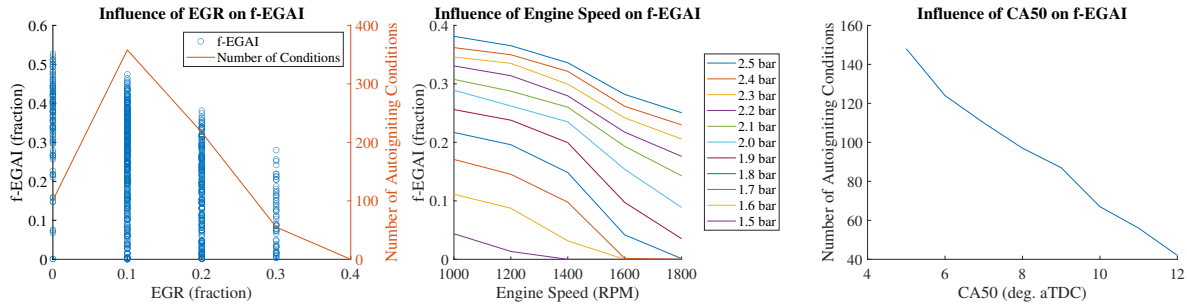

(a) Influence of EGR. **(b)** Influence of Eng. Spd. and IMP. **(c)** Influence of CA50.

Figure 9.5: Influence of engine control variables on f-EGAI. As expected, increasing EGR ratio, engine speed, and CA50 decreases f-EGAI. Conversely, increasing IMP increases f-EGAI

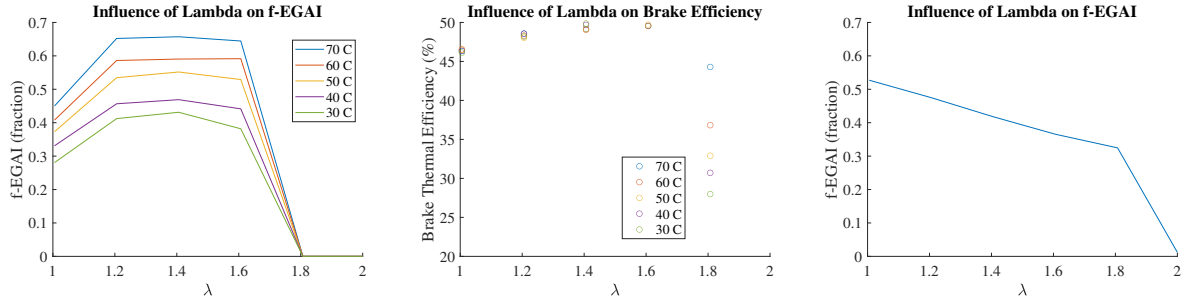

(a) Influence of λ at const. BMEP. **(b)** Impact on BTE at const. BMEP. **(c)** Impact on BTE at const. IMP.

Figure 9.6: Influence of λ on f-EGAI. Leaning λ at constant BMEP leads to higher f-EGAI due increase IMPs. Sudden drop in f-EGAI and BTE beyond λ=1.6 is caused by misfire/poor combustion.

9.3 Mechanisms for High Efficiencies

To have a complete understanding of the physical mechanisms by which EGAI is increasing thermal efficiency, this section provides a discussion on the effects of having a C-EGAI operation on different engine efficiencies/inefficiencies, energy losses, and combustion behavior.

All IC engines have energy losses throughout the cycle that greatly affect their final BTE. Being able to decrease them by changing combustion modes, materials or energy/exhaust gases re-utilization can have a positive impact on engine efficiency. At the same time, analyzing how these losses respond to these changes can shine light on the mechanisms by which engine efficiency is increased. Therefore, to understand how C-EGAI operation improves BTE, the following energy losses will be assessed:

1. Combustion losses due to incomplete combustion, quantified by the Combustion Efficiency;
2. Heat losses to the engine structure due to large temperature gradients between the hot gases and walls;
3. And exhaust losses due to not-fully-expanded gases.

Mechanical losses due to friction were assumed to be dependent only on engine speed and, thus, left out of the analysis since measured friction data from the manufacturer was available.

Starting with the analysis of how EGAI affects combustion efficiency, the experimental combustion efficiency was plotted versus f-EGAI and is shown in Figure 9.7. As expected, increasing the percentage of energy release by the EGAI event, i.e., f-EGAI, leads to an increased combustion efficiency. This was expected since autoignition consumes the fuel/air mixture that would not have been consumed otherwise due to flame quenching. However, the observed increase in combustion efficiency, although significant at approximately $1\%_{abs}$, is too small to be the sole mechanism responsible for the considerable increase in BTE observed during a C-EGAI operation.

Figure 9.8a shows the average heat transfer rate to the engine structure for all simulated cases as a function of f-EGAI. Clearly, increased levels of EGAI increase heat losses due to the higher in-cylinder temperatures and pressures experienced by the cylinder contents during the rapid heat

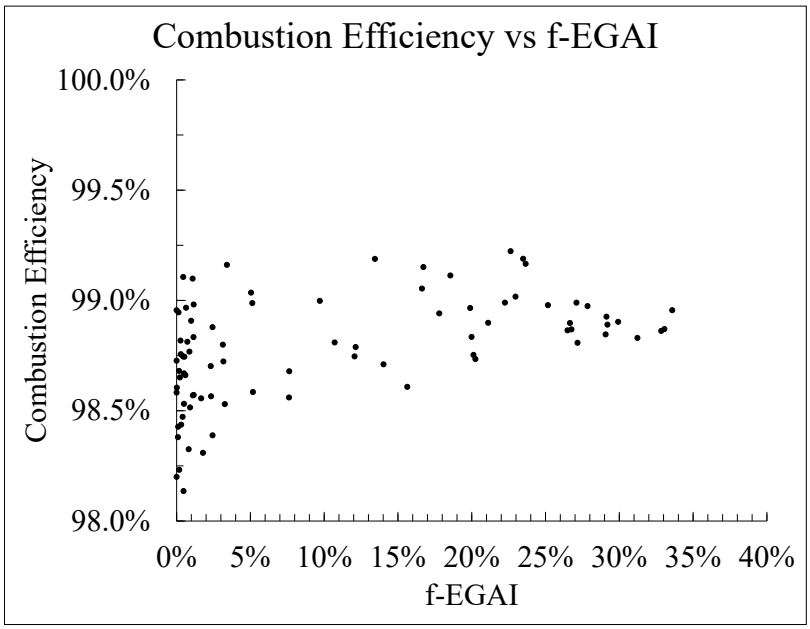

Figure 9.7: Effect of f-EGAI on Combustion Efficiency. Increase in Combustion Efficiency due to f-EGAI is significant but does not seem to be the sole mechanism responsible for the considerable increase in BTE.

release autoignition event, shown in Figure 9.9. Figure 9.8b shows that there is a somewhat constancy in the percentage of the total energy lost due to heat transfer since the data spread is relatively constant as f-EGAI is increased. Thus, the minimum influence observed on heat losses should not play a role in increasing BTE, especially because this minimum influence decreases BTE with increasing f-EGAI.

Finally, Figure 9.10 shows how EGAI affects exhaust losses. Figure 9.10 shows that increasing f-EGAI results in reduced exhaust losses, which is a consequence of more work being done during the expansion stroke. Figure 9.11 shows this increased work by plotting gIMEP, defined as the work done during the closed portion of the cycle normalized by the displaced volume, as a function of f-EGAI. As can be clearly seen, gIMEP considerably increases with increasing f-EGAI.

To further understand the causes for this increased work, Figure 9.12 shows the (a) Burn Duration, defined as the crank-angle interval from 10% to 90% mass fraction burned, versus f-EGAI, and (b) the crank-angle interval from 0-50% and 0-90% mass fraction burned versus f-EGAI. Figure 9.12a clearly shows that with increasing the intensity of EGAI (i.e., increase in f-EGAI), burn duration considerably decreases. Figure 9.12b shows that the first half of the burn duration (0-

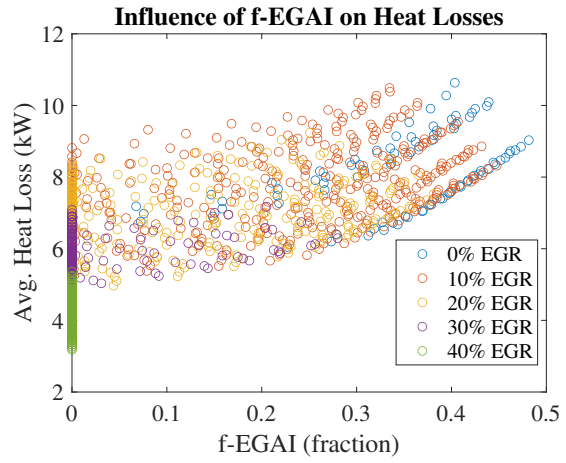

(a) Avg. Heat Losses.

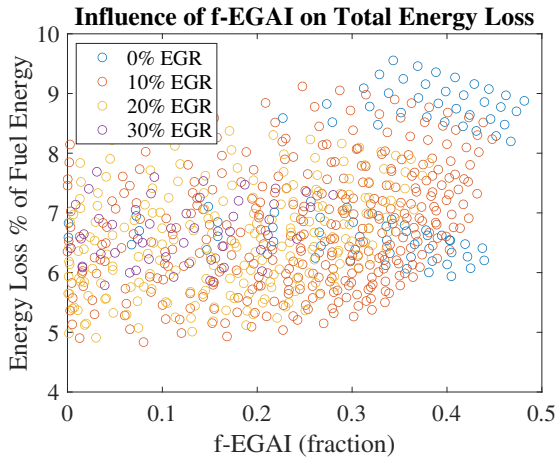

(b) Total Energy Loss % Fuel Energy.

Figure 9.8: Influence of f-EGAI on the Average Heat Loss (a) and Total Energy Loss as a percentage of Fuel Energy (b).

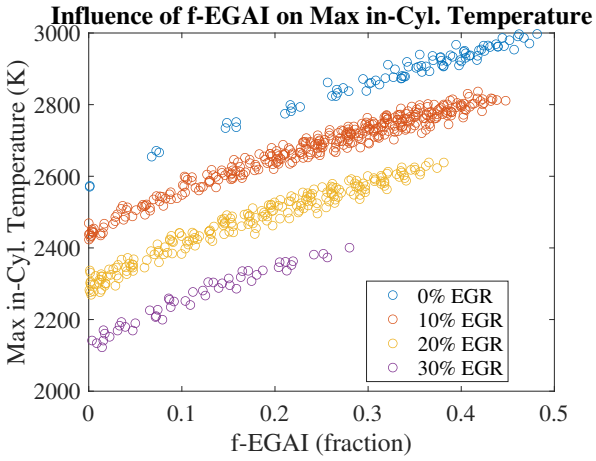

(a) Max in-Cyl. Temperature.

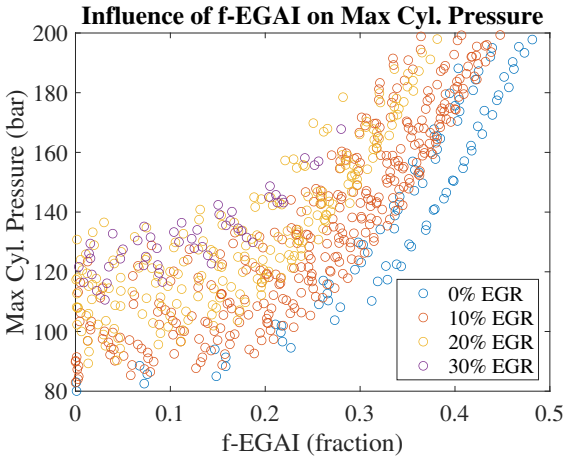

(b) Max in-Cyl. Pressure.

Figure 9.9: Influence of f-EGAI on the maximum in-cylinder Temperature (a) and Pressure (b). Increases in f-EGAI lead to higher in-cylinder temperatures and pressures.

50%) is nearly unaffected by the presence of EGAI; however, the crank-angle interval from 0-90% mass fraction burned considerably decreases, indicating that the second half (50-90%) of the overall combustion duration is considerably shortened by the presence of EGAI, being the responsible cause for the overall burn duration decrease.

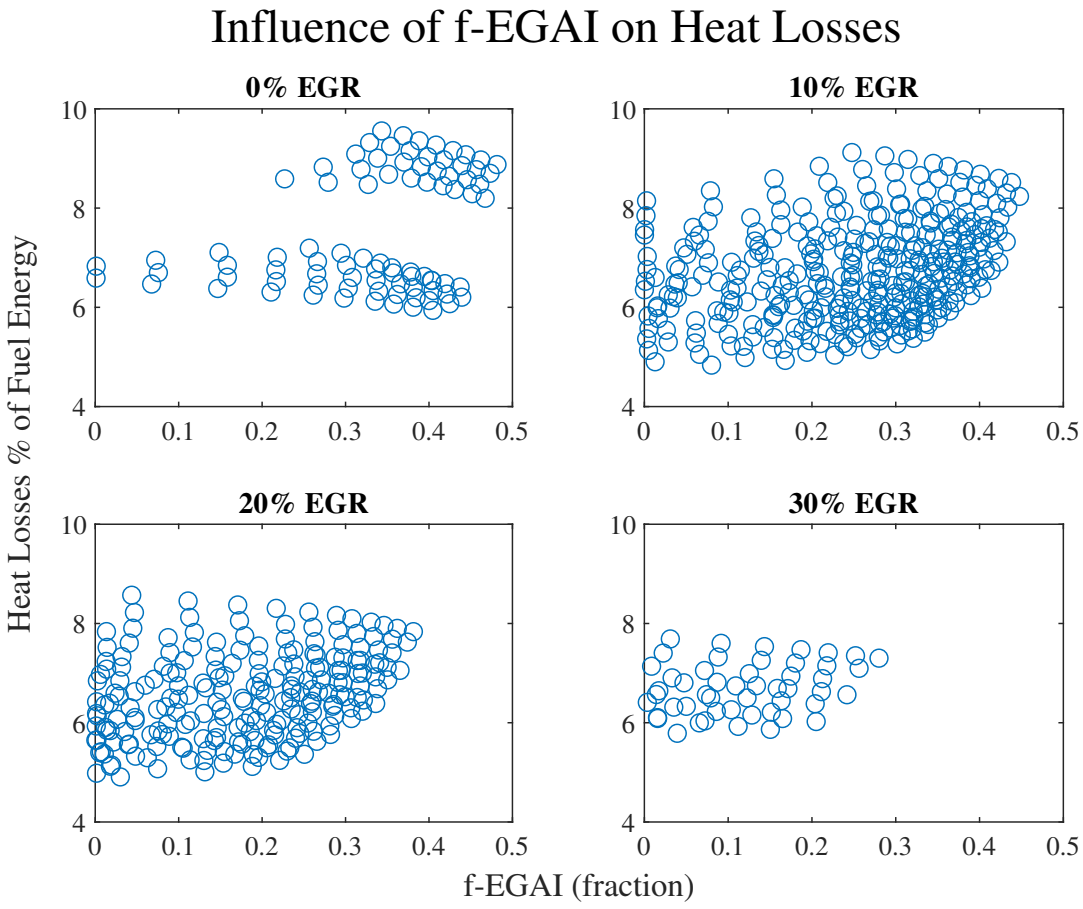

Figure 9.10: Effect of f-EGAI on Exhaust Losses. Exhaust Losses considerably decreases with increasing f-EGAI, indicating that work done increases with f-EGAI.

As a result of the shorter burn duration, energy is released earlier in the cycle when the cylinder volume is small and temperatures are high. From the Ideal Gas Law solved for pressure, Equation 9.2, one can see that the cylinder pressure rise will be greater when heat is released earlier in the cycle as opposed to later since the denominator (cylinder volume) is smaller and the numerator, dominated by the temperature variable, is larger. Thus, an increase in temperature earlier in the

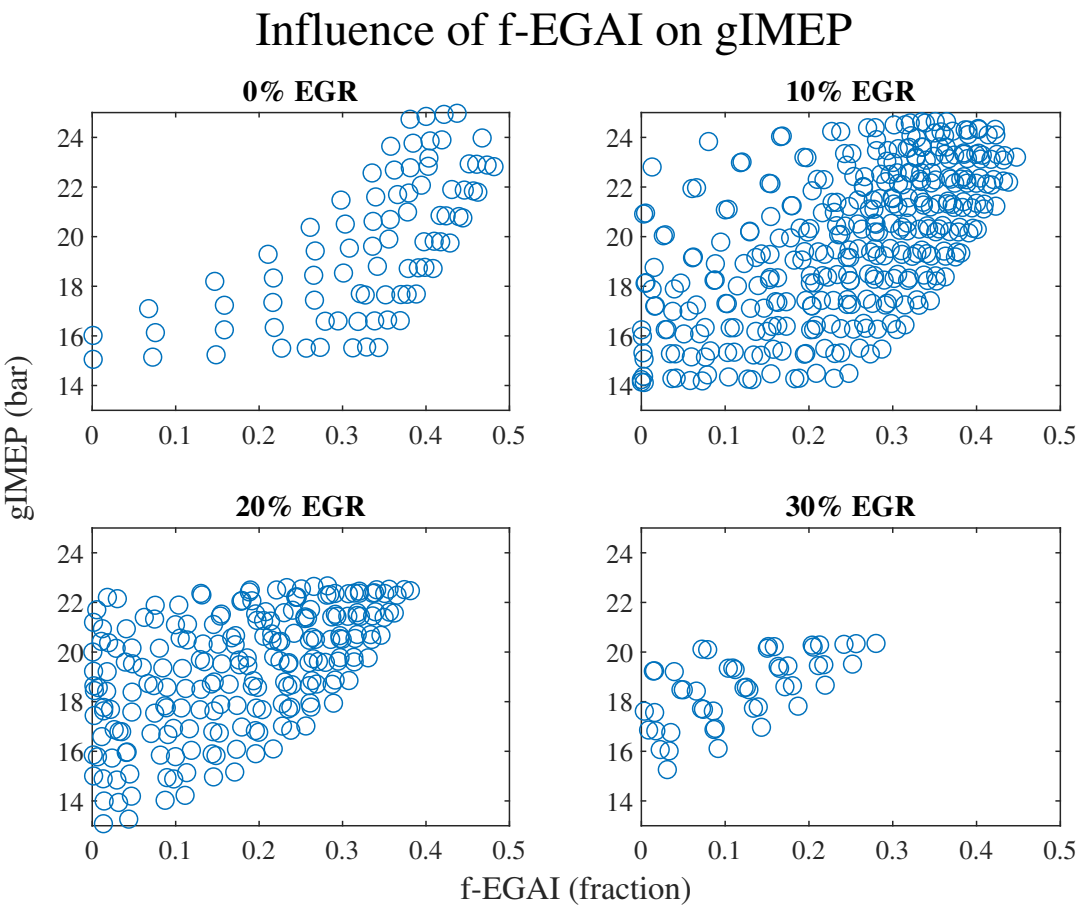

Figure 9.11: Effect of f-EGAI on gIMEP. gIMEP, as a proxy for work done, considerably increases with increases in f-EGAI, agreeing with decrease in Exhuast Losses shown in Figure 9.10.

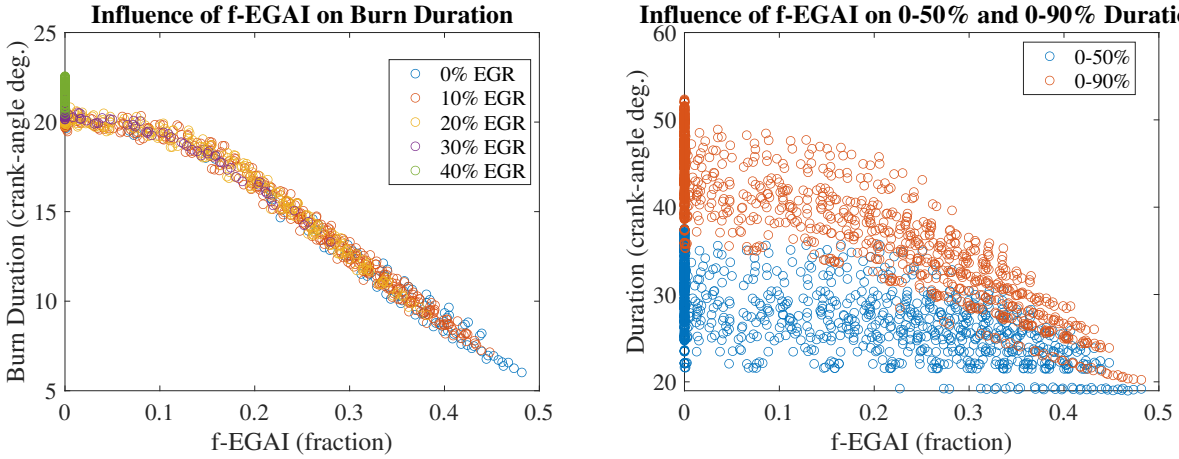

(a) Overall Burn Duration (10-90%)

(b) 0-50% and 0-90% interval

Figure 9.12: Influence of f-EGAI on the crank-angle interval between 0-50% and 0-90% mass fraction burned. Sharp decrease in 0-90% interval shows that EGAI considerably decreases the second half of the combustion event.

Table 9.2: Cummins X15 Engine operating conditions to trigger EGAI.

Variable	Min	Max
EGR Ratio	0%	30%
Engine Speed (RPM)	1000	1800
CA50 (deg. aTDC)	5	12
IMEP (bar)	13	25
BMEP (bar)	12	24

cycle, in this case, caused by the EGAI event, will have a larger effect on cylinder pressure than a later increase in temperature due to normal flame propagation, when temperatures have already dropped and volume, the denominator, is larger. Clearly, with higher cylinder pressures, more work is done via Equation 9.3, decreasing exhaust losses and, ultimately, increasing the engine's thermal efficiency.

$$P = \frac{mRT}{V} \tag{9.2}$$

$$W_{g,i} = \int_{-180}^{180} PdV \tag{9.3}$$

9.4 Mechanisms Enabling C-EGAI

Having discussed the mechanism by which a C-EGAI operation increases BTE, this section focuses on discussing the mechanisms by which EGAI is triggered. Starting from the engine's control variables, Table 9.2 shows the necessary range of engine operating conditions to trigger EGAI on the Cummins X15 engine. As can be seen on Table 9.2 and previously discussed in Section 9.3, EGAI can be triggered under a wide range of operating conditions except at 40% EGR ratio, where the high levels of dilution suppress EGAI.

Although the knowledge of the engine operating conditions that lead to EGAI is important for engine optimization, autoignition is a phenomenon controlled by the mixture's thermody-

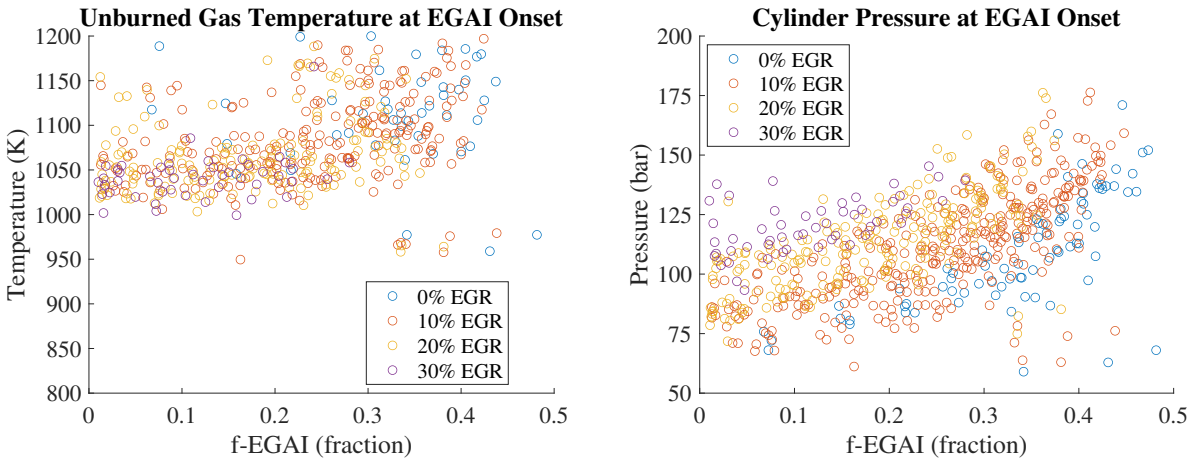

(a) End-Gas Temperature at EGAI Onset

(b) Pressure at EGAI Onset

Figure 9.13: Unburned End-Gas Temperature (a) and Pressure (b) at the onset of EGAI. As expected, increasing EGR ratio requires higher temperatures and pressures to ignite the unburned gases. Minimum required temperature and pressure to ignite the end-gas is show in Table 9.3.

namic states, properties, and reactivity, which are a result of the engine operating conditions and air/fuel/EGR mixture properties. Therefore, understanding how these factors are affecting and being affected by EGAI is of great importance if one aims at implementing C-EGAI combustion on different engine platforms. Starting from the unburned end-gas temperature and pressure at the onset of EGAI, Figure 9.13 shows the increasing requirement for both end-gas temperatures and pressures to trigger EGAI with increasing EGR ratio. Also clear on Figure 9.13 is the decreasing end-gas temperature and pressure with increasing EGR ratio. Table 9.3 shows the minimum required unburned end-gas temperature and pressure required to trigger EGAI with the NG composition tested and simulated in this work (MN=80). As expected, with increasing EGR ratios, the unburned end-gas temperature at which EGAI occurs increases.

In-cylinder gas temperature is largely controlled by the intake charge temperature, pressure, and EGR ratio. However, heat transfer to the cylinder walls decreases charge temperatures and pressures during combustion. For this reason, to analyze the EGAI sensitivity to cylinder walls, the model was run with increased wall temperatures from 500 K to 800 K in 50 K increments, while targeting the same operating conditions across all cases. Figure 9.14 shows that f-EGAI increases on average 2.6%$_{abs}$ for every 50 K increase in the cylinder walls, i.e., 0.52%$_{abs}$/K. As

Table 9.3: Minimum required end-gas Temperature and Pressure to trigger EGAI with simulated NG composition (MN=80).

EGR Ratio	Min $T_u(K)$	Min $P_u(bar)$
0%	781.5	59
10%	949.6	61.2
20%	958.3	71.8
30%	999.3	93.3

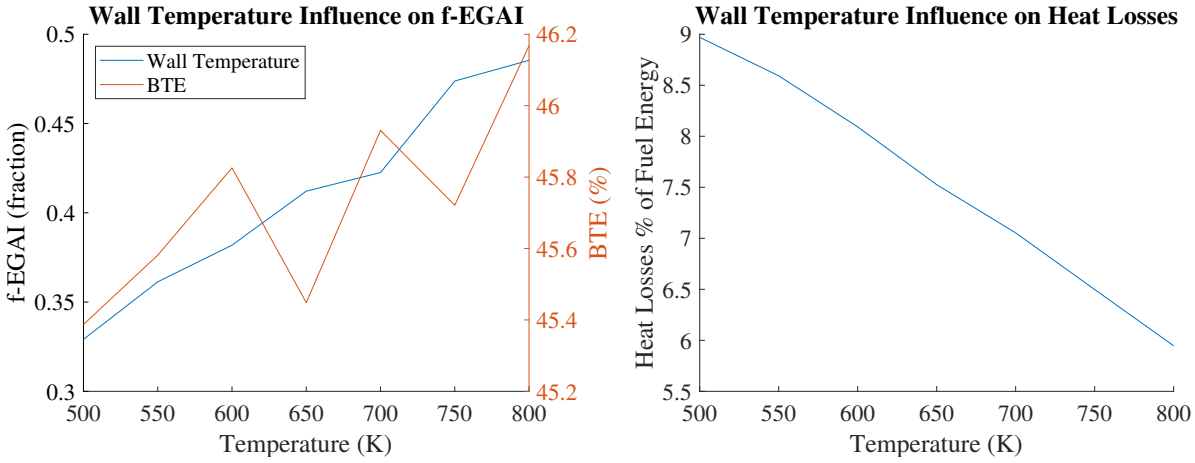

(a) Wall Temperature influence on f-EGAI and BTE

(b) Wall Temperature influence on Heat Losses

Figure 9.14: f-EGAI shows to be sensitive to wall temperatures. A 50 K increase in the wall temperature might result in a 2.5% increase in f-EGAI. Due to reduced heat losses and increased f-EGAI, BTE is increased with wall temperatures.

expected, increased cylinder walls result in an increased BTE due to reduced heat losses and increased unburned end-gas temperatures, as shown in Figure 9.14 and Figure 9.15. Note that the simulated cases shown in Figures 9.14 and 9.15 may have higher-than-realistic wall temperatures used only for exploration purposes.

As it is well known, fuel properties also play an important role in the propensity to EGAI [7,22]. Figure 9.16 shows the influence of Laminar Flame Speeds, S_L, measured at TDC conditions, on f-EGAI. As expected, higher S_L decreases f-EGAI by decreasing the induction time, i.e., a larger portion of the air/fuel/EGR mixture is consumed by the main propagating flame before EGAI takes

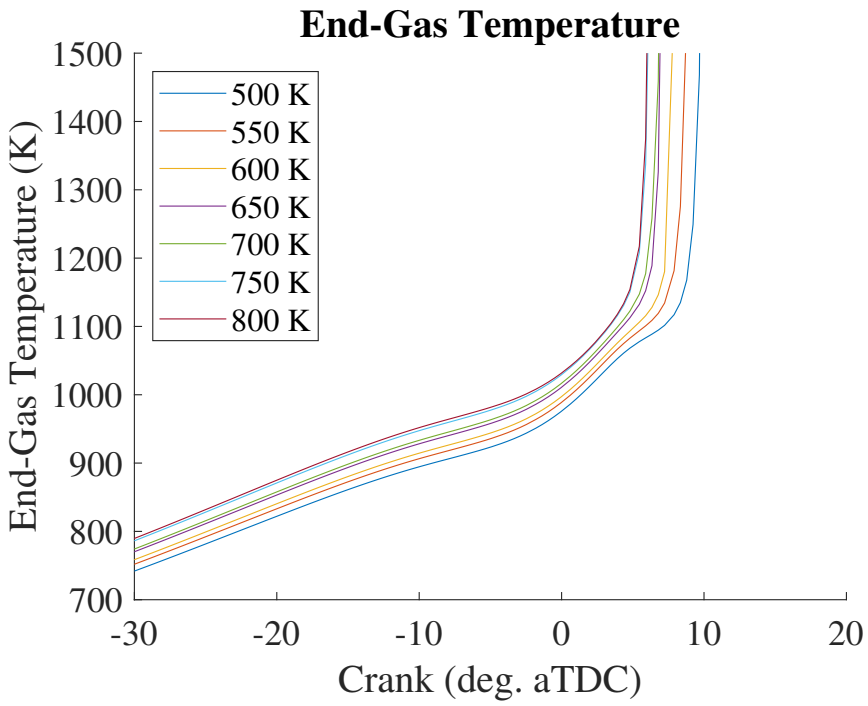

Figure 9.15: As expected, higher wall temperatures lead to higher unburned end-gas temperatures, causing an increase in f-EGAI. Legend temperatures are wall temperatures.

place. Also clear on Figure 9.16 is the strong EGR influence on S_L, which dilutes the reactive mixtures, reducing its reactivity and, consequently, its S_L.

As discussed in Chapter 7, a NG fuel's propensity to autoignite is strongly dependent on its Methane Number (MN). To analyze the f-EGAI's sensitivity to MN in real-world engine platform and conditions, simulations were run with all fuel compositions discussed in this dissertation, Tables 4.2 and 4.4, and pure CH_4, while targeting the same engine operating conditions (BMEP: 20 bar, CA50: 5 deg. aTDC, EGR: 20%, Eng. Spd.: 1000 RPM). As expected, fuels with higher MN, i.e., with smaller amounts of larger hydrocarbons (>C_2), result in a lower f-EGAI. The results from this analysis, shown in Figure 9.17, show that for every MN unit increase, there is a corresponding 0.6% decrease in f-EGAI. Additionally, Figure 9.17 clearly shows the decrease in BTE with a decreasing f-EGAI, as a consequence of the necessary increased fuel flow rates to achieve the same BMEP.

Finally, Figure 9.18 shows the influence of flow properties on f-EGAI. Increasing Turbulent Kinetic Energy (TKE) and Swirl Ratio decreases f-EGAI. This relationship is expected since in-

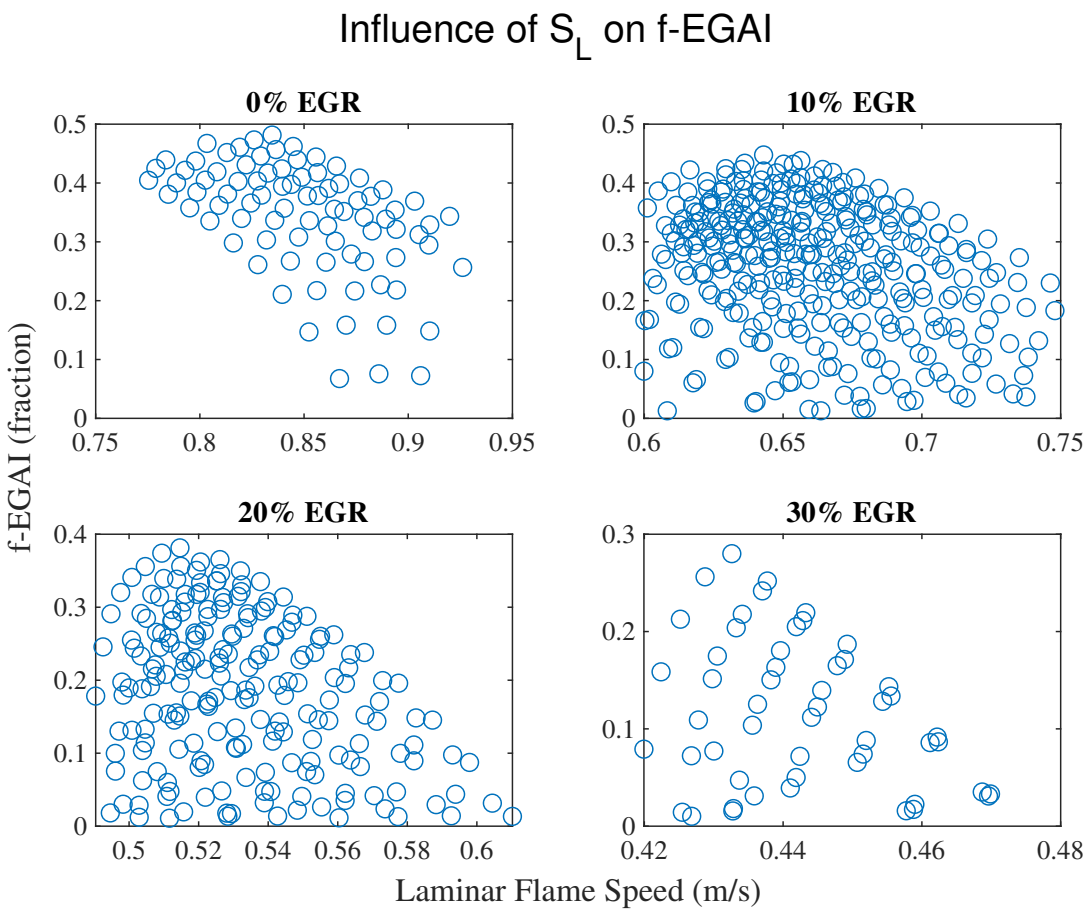

Figure 9.16: S_L measured at TDC. As expected, increasing S_L causes a reduction in f-EGAI due to the reduced induction time for EGAI to take place.

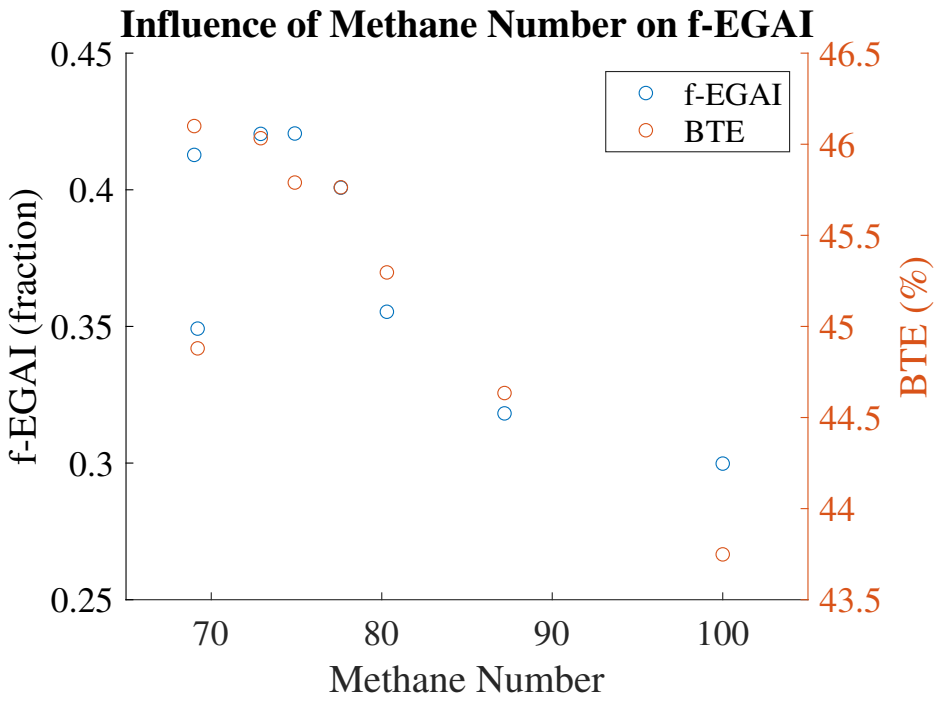

Figure 9.17: Fuel's Methane Number influence on f-EGAI. f-EGAI decreases by 0.6% for every 1 MN unit increase. More reactive NG fuels (lower MNs) result in higher BTE due to increased f-EGAI and, consequently, lower required fuel flow rates to achieve the same BMEP.

creased Swirl, when broken up, leads to increased TKE. Higher TKE, flow velocities, and S_L result in a faster flame propagation, quantified by the Turbulent Flame Speed, S_T, decreasing the induction time for EGAI to take place, as previously discussed. On the other hand, having larger Turbulent Length Scales as a consequence of swirls not breaking up into smaller swirls, decreases TKE, causing a reduction in S_T, which ultimately leaves more room for EGAI occur. Similarly to Engine Speed, one of the main in-cylinder turbulence controlling factors, flow properties' influence on EGAI is also dependent on IMP and other operating condition variables.

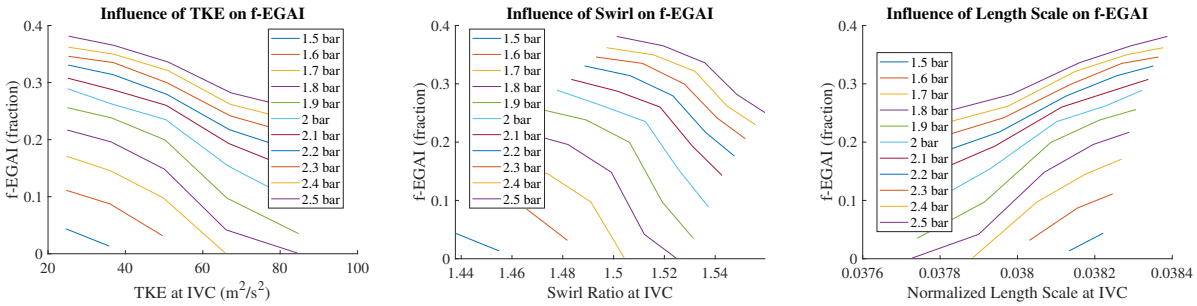

(a) TKE influence on f-EGAI **(b)** Swirl Ratio influence on f-EGAI **(c)** Length Scale influence on f-EGAI

Figure 9.18: Flow properties influence on f-EGAI. Swirl Ratio is defined as the ratio of the flow rotation speed to the Engine Speed (ω_f/ω_{engine}). Normalized Length Scale is defined as the ratio of the turbulent length scale to the engine bore diameter.

Chapter 10

Conclusions and Future Work

10.1 Conclusions

Detection, modeling, and control variables of EGAI have been thoroughly analyzed and discussed in this dissertation. In this last chapter, the main takeaways from each piece of this work is presented.

In order to study EGAI processes in IC engines, one needs to be able to detect its presence and quantify its intensity. Literature review and engine testing experience on this subject revealed that, although current detection methods can be appropriate to detect EGAI under a C-EGAI operation, quantification methods of EGAI still lacked accuracy, especially if the f-EGAI metric is to be used. Additionally, detection and quantification are often engine and operating-conditions dependent, relying on calibrations from an experienced operator or engineer. For this reason, a novel EGAI detection and onset determination method was developed to reliably quantify EGAI for data analysis, engine modeling, and engine control. This new method, named the 'CECL method,' is solely based on the AHRR curve profile, completely eliminating the need for engine- and operating-conditions-specific calibration. This method proved successful to capture the local minimum points or points of rapid increase in the AHRR curve slope that identifies and onset of EGAI as well as proved successful to detect the presence of EGAI. Additionally, the algorithm ran in under 2 milliseconds on a standard workstation, indicating the possibility of being implemented in real-time, closed-loop control systems.

Having been able to detect and quantify EGAI, computational models of the CFR engine running on NG were developed to study the engine/fuel interactions that lead to NG EGAI and its performance benefits. These models, although appropriate to capture EGAI in SI NG engines, showed the need to account for NO_x chemistry when predicting NG EGAI. Moreover, simulation

results showed that increasing levels of f-EGAI enhances Indicated Thermal Efficiencies (ITE) up to a maximum, where combustion instability overweights the increased efficiency due to EGAI.

Since NO_x chemistry showed to be essential at accurately capturing EGAI in NG engine simulations and due to the lack of a reduced chemical mechanism developed for real NG compositions including NO_x chemistry in the literature, a study was conducted to generate a reduced, NO_x-chemistry-containing, NG reduced mechanism with suitable size for multi-dimensional engine simulations. To this goal, NO_x chemistry was incorporated into the ARIES82 mechanism developed by Mohr et al. [48,49]. With the newly developed NG/NO_x mechanism, ARIES82NOx_x, simulated onset of EGAI agreed within ± 1 crank-angle degree for all simulated cases using the CONVERGE CFD models of the CFR engine. Additionally, using the newly developed ARIES82NO_x mechanism, key reaction pathways were analyzed to shine light on the impact of NO_x chemistry on NG combustion. Mechanism results for IDTs and S_L as well as sensitivity analysis were compared to state-of-the-art detailed mechanisms such as ARAMCO 3.0 and NUIG Mech1.2 to confirm its accuracy and robustness. A remarkably good agreement was found with overall deviations being $\leq 1\%$.

The CFR engine models were then used to study the role of NG composition on EGAI. The in-cylinder combustion behavior between the NG fuels and their MN reference CH_4/H_2 blends revealed to be remarkably similar, even when tested at more extreme engine-like conditions and varying knock intensity levels. Laminar flame speeds for NG fuels and their reference blends are very similar; however, differences in the IDTs were noticed, with the wetter NG fuels, i.e., more reactive fuels, exhibiting shorter IDTs than their reference blends. With slightly faster S_L and longer IDTs for the same temperature and pressure, the reference CH_4/H_2 fuel should theoretically have a lower propensity to autoignite than its NG counterpart, as all of the unburned gas would be consumed before any autoignition could take place. However, the remarkably similar autoignition behavior can be explained by understanding that turbulent combustion dominates under engine conditions, eliminating the differences in flame propagation, and that the MN reference fuels have higher specific heats ratio, causing unburned gas temperatures to be higher, which, in turn, shortens

IDTs. The outcomes of this study confirm again that the KI is linked to the f-EGAI and, when coupled with a 0-D homogeneous batch reactor simulation, might allow one to quickly predict the propensity of a fuel to knock if reliable engine specific information (e.g., pressure/temperature history) from an experiment or CFD simulation is available to be used as an input.

The modeling strategies developed with the CFR engine and the chemical mechanism developed in Chapter 6 were used to model the Cummins X15 engine converted to SI NG operation. A new piston was designed to allow for a high-efficiency, C-EGAI operation while being fueled with NG. The engine's geometrical compression ratio was optimized using a predictive GT-Power model. At the optimum compression ratio, new piston bowl geometries were design and simulated to enhance turbulence and improve efficiency. The final design was selected based on the highest number of operating points allowing for an operation at $\geq$44%, and with the widest margin for a C-EGAI. The final piston had a compression ratio of 14:1 with a squish-area ratio of 71%. Testing results from the optimized piston reached Brake Thermal Efficiencies $\geq$45%, exceeding that of the baseline Diesel Cummins X15 engine (44%).

Finally, a GT-Power model of the Cummins X15 was created to predict engine results when running with the optimized piston design in order to assess how a C-EGAI operation perform under a wide range of operating conditions, and to study the mechanisms by which efficiency is enhanced and EGAI triggered. This study showed that EGAI is achievable under a wide range of conditions except when EGR ratio is >30% due to excessive dilution. Nonetheless, an operation at $\geq$44% showed to be possible at all levels of EGR ratio; however, due to increased EGAI intensity and possibility of hardware damage, EGR is likely necessary for stable and safe C-EGAI operation. The study also informed that, for even further improvements in the Brake Thermal Efficiency, leaner mixtures and slower Engine Speeds should be used, which could allow Brake Thermal Efficiencies to approach the 50% BTE mark. The model also informed that a C-EGAI operation increases Combustion Efficiency and Heat Losses but decreases Exhaust Losses. The reduced burn duration caused by the EGAI event results in higher cylinder pressures earlier in the cycle, being closer to an ideal Otto cycle, resulting in more work being transferred to the piston, increasing

thermal efficiency. An end-gas temperature of 781.5 K at 59 bar was found to be the minimum to trigger EGAI on the Cummins X15 engine, with the temperature increasing depending on the engine operating conditions and NG's Methane Number. Finally, contrary to knock-free SI NG engines, more reactive compositions of NG, i.e., lower Methane Numbers, showed to be beneficial to engine performance under a C-EGAI operation since, due to EGAI, less fuel is required to achieve the same BMEP levels, increasing the engine's Brake Thermal Efficiency.

10.2 Future Work

To take this research work further and prove its suitability to be applied in a real world context, the following work should be performed:

1. The CECL method for detection and quantification of EGAI should be applied in a closed-loop control system to prove its suitability to detect and quantify EGAI in real time. Additionally, the method should be tested with lower resolution, lower cost sensors to ensure it would still be able to capture the characteristic profiles of the AHRR required by the newly developed technique.

2. Although ARIES82NO$_x$ mechanism has a suitable size for multi-dimensional engine simulations, its size could be a bottle-neck depending on the size of the engine being simulated and should be further reduced. ARIES50NO$_x$ is a good further-reduced version of ARIES82NO$_x$ but lacks good S_L agreement with state-of-the-art detailed mechanisms. Thus, a new mechanism reduction on ARIES82NO$_x$, targeting S_L, would be beneficial for multi-dimension engine simulation computational performance.

3. It would be of great benefit to expand the analysis of mechanisms for higher efficiencies and C-EGAI operation to different NG compositions, λ, and other fuels. Additionally, a thorough statistical analysis on the expanded DOE could allow a more precise understanding of the most influential variables leading to EGAI and higher efficiencies, informing where to focus with the engine optimization.

4. Finally, full engine testing, using a variety of fuel compositions, and under transient operation should be studied to validate the potential of the C-EGAI operation to be deployed in a real-world application. Additionally, to ensure a low cost of deployment, different control methods, with lower cost sensors such as knock sensors or the use of different control variables/feedback, should be explored as means to control EGAI.

Bibliography

[1] Rolf D Reitz. Directions in internal combustion engine research. *Combustion and Flame*, 160(1):1–8, 2013.

[2] Gautam T Kalghatgi. The outlook for fuels for internal combustion engines. *International Journal of Engine Research*, 15(4):383–398, 2014.

[3] GT Kalghatgi. Developments in internal combustion engines and implications for combustion science and future transport fuels. *Proceedings of the Combustion Institute*, 35(1):101–115, 2015.

[4] Robert H Mitchell and Daniel B Olsen. Extending substitution limits of a diesel–natural gas dual fuel engine. *Journal of Energy Resources Technology*, 140(5), 2018.

[5] Arvind Thiruvengadam, Marc Besch, Vishnu Padmanaban, Saroj Pradhan, and Berk Demirgok. Natural gas vehicles in heavy-duty transportation-a review. *Energy Policy*, 122:253–259, 2018.

[6] A Das and HC Watson. Development of a natural gas spark ignition engine for optimum performance. *Proceedings of the Institution of Mechanical Engineers, Part D: Journal of Automobile Engineering*, 211(5):361–378, 1997.

[7] John B Heywood. *Internal Combustion Engine Fundamentals*, volume 1. McGraw-Hill Education, 1988.

[8] U.S. Department of Energy. Alternative Fuels Data Center: Natural Gas Fuel Basics. https://afdc.energy.gov/fuels/natural_gas_basics.html, October 2020.

[9] Bradley E Anderson and Veysel Uz. Compressed natural gas as a feasible replacement fuel for us transportation. *The Journal of Defense Modeling and Simulation*, 12(1):67–78, 2015.

[10] ASTM Standard et al. Standard test method for research octane number of spark-ignition engine fuel. *D2699, Rev. December*, 2004.

[11] M Leiker, CHRISTOP. K, CARTELLI. W, U Pfeifer, and M Rankl. Evaluation of antiknocking property of gaseous fuels by means of methane number and its practical application to gas engines. In *Mechanical Engineering*, volume 94, page 55. ASME-AMER SOC MECHANICAL ENG 345 E 47TH ST, NEW YORK, NY 10017, 1972.

[12] Daniel M Wise. *Investigation into producer gas utilization in high performance natural gas engines*. PhD thesis, Colorado State University. Libraries, 2013.

[13] Hui Xu, Axel O zur Loye, and Robin J Bremmer. An alternative calculation for methane number for lean burn spark ignited engines operating on low energy content gaseous fuels. In *Internal Combustion Engine Division Fall Technical Conference*, volume 58318, page V001T03A006. American Society of Mechanical Engineers, 2017.

[14] R Turns Stephen. An introduction to combustion, 2000.

[15] Norbert Peters. Fifteen lectures on laminar and turbulent combustion. *Ercoftac Summer School*, 1428:245, 1992.

[16] Nicolo Cavina, Nahuel Rojo, Lorella Ceschini, Eleonora Balducci, Luca Poggio, Lucio Calogero, and Ruggero Cevolani. Investigation of knock damage mechanisms on a gdi tc engine. Technical report, SAE Technical Paper, 2017.

[17] RJ Nates and ADB Yates. Knock damage mechanisms in spark-ignition engines. *SAE transactions*, pages 1970–1980, 1994.

[18] Roy J Nates. Thermal stresses induced by knocking combustion in spark-ignition engines. Technical report, SAE Technical Paper, 2000.

[19] Scott Michael Bayliff. Evaluation of controlled end gas auto ignition with exhaust gas recirculation in a stoichiometric, spark ignited, natural gas engine. *2020-CSU Theses and Dissertations*, 2020.

[20] Gregory J Hampson. High efficiency natural gas engine combustion using controlled auto-ignition. In *Internal Combustion Engine Division Fall Technical Conference*, volume 59346, page V001T03A019. American Society of Mechanical Engineers, 2019.

[21] Diego Bestel, Scott Bayliff, Anthony Marchese, Daniel Olsen, Bret Windom, and Hui Xu. Multi-dimensional modeling of the cfr engine for the investigation of si natural gas combustion and controlled end-gas autoignition. In *Internal Combustion Engine Division Fall Technical Conference*, volume 84034, page V001T06A012. American Society of Mechanical Engineers, 2020.

[22] Diego Bestel, Scott Bayliff, Hui Xu, Anthony Marchese, Daniel Olsen, and Bret Windom. Investigation of the end-gas autoignition process in natural gas engines and evaluation of the methane number index. *Proceedings of the Combustion Institute*, 2020.

[23] Dennis Robertson and Robert Prucka. A review of spark-assisted compression ignition (saci) research in the context of realizing production control strategies. Technical report, SAE Technical Paper, 2019.

[24] Andrew John Zdanowicz. *End-Gas Autoignition Propensity and Flame Propagation Rate Measurements in Laser-Ignited Rapid Compression Machine Experiments*. PhD thesis, Colorado State University. Libraries, 2019.

[25] Angelo Onorati and Gianluca Montenegro. *1D and Multi-D Modeling Techniques for IC Engine Simulation*, volume 1. SAE, 2020.

[26] Gamma Technologies. Gt-power: User's manual and tutorial, 2018.

[27] K. J. Richards, P. K. Senecal, and E. Pomraning. Converge 2.4, 2020.

[28] K. J. Richards, P. K. Senecal, and E. Pomraning. Converge 3.0, 2020.

[29] SD Hires, RJ Tabaczynski, and JM Novak. The prediction of ignition delay and combustion intervals for a homogeneous charge, spark ignition engine. *SAE transactions*, pages 1053–1067, 1978.

[30] Norman C Blizard and James C Keck. Experimental and theoretical investigation of turbulent burning model for internal combustion engines. *SAE Transactions*, pages 846–864, 1974.

[31] Thomas Morel, Charles I Rackmil, Rifat Keribar, and Mark J Jennings. Model for heat transfer and combustion in spark ignited engines and its comparison with experiments. *SAE transactions*, pages 348–362, 1988.

[32] Mohamad Metghalchi and James C Keck. Burning velocities of mixtures of air with methanol, isooctane, and indolene at high pressure and temperature. *Combustion and flame*, 48:191–210, 1982.

[33] SY Liao, DM Jiang, and Q Cheng. Determination of laminar burning velocities for natural gas. *Fuel*, 83(9):1247–1250, 2004.

[34] Juan J Hernandez, Magin Lapuerta, Clara Serrano, and Andres Melgar. Estimation of the laminar flame speed of producer gas from biomass gasification. *Energy & fuels*, 19(5):2172–2178, 2005.

[35] K. J. Richards, P. K. Senecal, and E. Pomraning. Converge 2.4 manual, 2020.

[36] Eric Pomraning, Keith Richards, and PK Senecal. Modeling turbulent combustion using a rans model, detailed chemistry, and adaptive mesh refinement. Technical report, SAE Technical Paper, 2014.

[37] Otto Redlich and Joseph NS Kwong. On the thermodynamics of solutions. v. an equation of state. fugacities of gaseous solutions. *Chemical reviews*, 44(1):233–244, 1949.

[38] Giorgio Soave. Equilibrium constants from a modified redlich-kwong equation of state. *Chemical engineering science*, 27(6):1197–1203, 1972.

[39] Ding-Yu Peng and Donald B Robinson. A new two-constant equation of state. *Industrial & Engineering Chemistry Fundamentals*, 15(1):59–64, 1976.

[40] Stephen B. Pope. *Turbulent Flows*, volume 1. Cambridge University Press, 2000.

[41] PK Senecal, E Pomraning, KJ Richards, TE Briggs, CY Choi, RM McDavid, and MA Patterson. Multi-dimensional modeling of direct-injection diesel spray liquid length and flame lift-off length using cfd and parallel detailed chemistry. *SAE transactions*, pages 1331–1351, 2003.

[42] Norbert Peters. *Turbulent Combustion*, volume 1. Cambridge University Press, 2000.

[43] Pierre Pelce and Paul Clavin. Influence of hydrodynamics and diffusion upon the stability limits of laminar premixed flames. *Journal of Fluid Mechanics*, 124:219–237, 1982.

[44] Moshe Matalon and Bernard J Matkowsky. Flames as gasdynamic discontinuities. *Journal of Fluid Mechanics*, 124:239–259, 1982.

[45] Pinaki Pal, Christopher Kolodziej, Seungmok Choi, Sibendu Som, Alberto Broatch, Josep Gomez-Soriano, Yunchao Wu, Tianfeng Lu, and Yee Chee See. Development of a virtual cfr engine model for knocking combustion analysis. *SAE International Journal of Engines*, 11(6):1069–1082, 2018.

[46] Zongyu Yue and Sibendu Som. Fuel property effects on knock propensity and thermal efficiency in a direct-injection spark-ignition engine. *Applied Energy*, page 114221, 2019.

[47] Zongyu Yue, K Dean Edwards, C Scott Sluders, and Sibendu Som. Prediction of cyclic variability and knock-limited spark advance in a spark-ignition engine. *Journal of Energy Resources Technology*, 141(10), 2019.

[48] Jeffrey Thomas Mohr. The effect of fuel reactivity and exhaust gas recirculation on knock propensity of natural gas. *2020-CSU Theses and Dissertations*, 2020.

[49] Jeffrey Mohr, Bret Windom, Daniel B Olsen, and Anthony J Marchese. Homogeneous ignition delay, flame propagation rate and end-gas autoignition fraction measurements of natural gas and exhaust gas recirculation blends in a rapid compression machine. In *Internal Combustion Engine Division Fall Technical Conference*, volume 84034, page V001T03A012. American Society of Mechanical Engineers, 2020.

[50] Kai J Morganti, Michael J Brear, Gabriel da Silva, Yi Yang, and Frederick L Dryer. The autoignition of liquefied petroleum gas (lpg) in spark-ignition engines. *Proceedings of the Combustion Institute*, 35(3):2933–2940, 2015.

[51] Tien Mun Foong, Michael J Brear, Kai J Morganti, Gabriel da Silva, Yi Yang, and Frederick L Dryer. Modeling end-gas autoignition of ethanol/gasoline surrogate blends in the cooperative fuel research engine. *Energy & Fuels*, 31(3):2378–2389, 2017.

[52] YL Chan, JH Bromly, AA Konnov, and DK Zhang. The comparative and combined effects of nitric oxide and higher alkanes in sensitizing methane oxidation. *Combustion science and technology*, 184(1):114–132, 2012.

[53] Deng Fuquan, Zhao Ningbo, Wu Yingtao, Yang Jialong, Tang Chenglong, Li Zhiming, Zheng Hongtao, and Zuohua Huang. Experimental and kinetic study of the promoting-effect of nitrogen dioxide on the ethane autoignition in a rapid compression machine. *Energy & Fuels*, 2020.

[54] Zhongyuan Chen, Peng Zhang, Yi Yang, Michael J Brear, Xin He, and Zhi Wang. Impact of nitric oxide (no) on n-heptane autoignition in a rapid compression machine. *Combustion and Flame*, 186:94–104, 2017.

[55] Zhongyuan Chen. *Impact of nitric oxide on autoignition of hydrocarbon fuels*. PhD thesis, The University of Melbourne, 2018.

[56] Hugo Ajrouche, Ob Nilaphai, Camille Hespel, and Fabrice Foucher. Impact of nitric oxide on n-heptane and n-dodecane autoignition in a new high-pressure and high-temperature chamber. *Proceedings of the Combustion Institute*, 37(3):3319–3326, 2019.

[57] Hao Zhang, Steffen Schmitt, Lena Ruwe, and Katharina Kohse-Höinghaus. Inhibiting and promoting effects of no on dimethyl ether and dimethoxymethane oxidation in a plug-flow reactor. *Combustion and Flame*, 2020.

[58] S Gersen, AV Mokhov, JH Darmeveil, HB Levinsky, and Peter Glarborg. Ignition-promoting effect of no2 on methane, ethane and methane/ethane mixtures in a rapid compression machine. *Proceedings of the Combustion Institute*, 33(1):433–440, 2011.

[59] Christian Lund Rasmussen, Anja Egede Rasmussen, and Peter Glarborg. Sensitizing effects of nox on ch4 oxidation at high pressure. *Combustion and Flame*, 154(3):529–545, 2008.

[60] Olivier Mathieu, John M Pemelton, Gilles Bourque, and Eric L Petersen. Shock-induced ignition of methane sensitized by no2 and n2o. *Combustion and Flame*, 162(8):3053–3070, 2015.

[61] Fuquan Deng, Feiyu Yang, Peng Zhang, Youshun Pan, John Bugler, Henry J Curran, Yingjia Zhang, and Zuohua Huang. Towards a kinetic understanding of the nox promoting-effect on ignition of coalbed methane: A case study of methane/nitrogen dioxide mixtures. *Fuel*, 181:188–198, 2016.

[62] Arvind V Menon, Seong-Young Lee, Milton J Linevsky, Thomas A Litzinger, and Robert J Santoro. Addition of no2 to a laminar premixed ethylene–air flame: effect on soot formation. *Proceedings of the Combustion Institute*, 31(1):593–601, 2007.

[63] Fuquan Deng, Honghao Xu, Xiao Liu, Yingtao Wu, Honghao Zheng, and Zhiming Li. Effect of nitrogen dioxide addition on ethane auto-ignition at different pressures and equivalence ratios: Experiments and chemical kinetic modeling. *Fuel*, 285:119042, 2021.

[64] Fahd E Alam, Francis M Haas, Tanvir I Farouk, and Frederick L Dryer. Influence of trace nitrogen oxides on natural gas oxidation: Flow reactor measurements and kinetic modeling. *Energy & Fuels*, 31(3):2360–2369, 2017.

[65] X Zhang, W Ye, JC Shi, XJ Wu, RT Zhang, and SN Luo. Shock-induced ignition of methane, ethane, and methane/ethane mixtures sensitized by no2. *Energy & Fuels*, 31(11):12780–12790, 2017.

[66] Ponnuthurai Gokulakrishnan, Casey C Fuller, Michael S Klassen, Richard G Joklik, Yash N Kochar, Sarah N Vaden, Timothy C Lieuwen, and Jerry M Seitzman. Experiments and modeling of propane combustion with vitiation. *Combustion and Flame*, 161(8):2038–2053, 2014.

[67] AA Burluka, K Liu, CGW Sheppard, AJ Smallbone, and R Woolley. The influence of simulated residual and no concentrations on knock onset for prfs and gasolines. *SAE transactions*, pages 1873–1889, 2004.

[68] PJ Roberts and CGW Sheppard. The influence of residual gas no content on knock onset of iso-octane, prf, trf and ulg mixtures in si engines. *SAE International Journal of Engines*, 6(4):2028–2043, 2013.

[69] Zhongyuan Chen, Hao Yuan, Yi Yang, and Michael Brear. The effect of nitric oxide on knock onset of iso-octane in a cfr spark-ignition engine. In *10th Asia Pacific Conference on Combustion*, 2015.

[70] Fubai Li, Changpeng Liu, Heping Song, and Zhi Wang. Improving combustion and emission characteristics in heavy-duty natural-gas engine by using pistons enhancing turbulence. Technical report, SAE Technical Paper, 2018.

[71] Ahmed Abdul Moiz, Zainal Abidin, Robert Mitchell, and Michael Kocsis. Development of a natural gas engine with diesel engine-like efficiency using computational fluid dynamics. Technical report, SAE Technical Paper, 2019.

[72] PG Hill and D Zhang. The effects of swirl and tumble on combustion in spark-ignition engines. *Progress in energy and combustion science*, 20(5):373–429, 1994.

[73] Mahmut Kaplan. Influence of swirl, tumble and squish flows on combustion characteristics and emissions in internal combustion engine-review. *International Journal of Automotive Engineering and Technologies*, 8(2):83–102, 2019.

[74] A Nagao. The effect of swirl control on combustion improvement of spark ignition engine. *I. Mech. E.*, 54, 1983.

[75] Richard C Belaire, George C Davis, JC Kent, and Rodney J Tabaczynski. Combustion chamber effects on burn rates in a high swirl spark ignition engine. *SAE transactions*, pages 1130–1138, 1983.

[76] Kern-Yong Kang, Seung-Mook Oh, Jin-Wook Lee, Ki-Hyung Lee, and Choong-Sik Bae. The effects of tumble flow on lean burn characteristics in a four-valve si engine. *SAE transactions*, pages 981–989, 1997.

[77] O Hadded and Ingemar Denbratt. Turbulence characteristics of tumbling air motion in four-valve si engines and their correlation with combustion parameters. *SAE transactions*, pages 741–759, 1991.

[78] Tomonori Urushihara, Taichi Murayama, Yasuo Takagi, and Ki-Hyung Lee. Turbulence and cycle-by-cycle variation of mean velocity generated by swirl and tumble flow and their effects on combustion. *SAE transactions*, pages 1382–1389, 1995.

[79] Ahmet Selamet, S Rupal, Y He, and PS Keller. An experimental study on the effect of intake primary runner blockages on combustion and emissions in si engines under part-load conditions. Technical report, SAE Technical Paper, 2004.

[80] Bowen Yan, Laihui Tong, Hu Wang, Zunqing Zheng, Yufeng Qin, and Mingfa Yao. Experimental and numerical investigation of the effects of combustion chamber reentrant level

on combustion characteristics and thermal efficiency of stoichiometric operation natural gas engine with egr. *Applied Thermal Engineering*, 123:1473–1483, 2017.

[81] Bowen Yan, Hu Wang, Zunqing Zheng, Yufeng Qin, and Mingfa Yao. The effect of combustion chamber geometry on in-cylinder flow and combustion process in a stoichiometric operation natural gas engine with egr. *Applied Thermal Engineering*, 129:199–211, 2018.

[82] Anh Tuan Le, Dang Quoc Tran, Thanh Tam Tran, Anh Tuan Hoang, and Van Viet Pham. Performance and combustion characteristics of a retrofitted cng engine under various piston-top shapes and compression ratios. *Energy Sources, Part A: Recovery, Utilization, and Environmental Effects*, pages 1–17, 2020.

[83] Juan Felipe Rodriguez, Hui Xu, Greg Hampson, Brent Windom, Anthony Marchese, and Daniel B Olsen. Heavy duty natural gas single cylinder research engine installation, commissioning, and baseline testing. *Energy and Power Engineering*, 14(6):217–232, 2022.

[84] Waukesha Engine. Waukesha cfr f-1 & f-2 research method (f-1) motor method (f-2) octane rating units operation & maintenance, 1998.

[85] Diego Bernardi Bestel, Juan Rodriguez, Anthony Marchese, Daniel Olsen, and Bret Windom. Detection and onset determination of end-gas autoignition on spark-ignited natural gas engines based on the apparent heat release rate. Technical report, SAE Technical Paper, 2022.

[86] Andrew Zdanowicz, Jeffrey Mohr, Jessica Tryner, Kara Gustafson, Bret Windom, Daniel B Olsen, Gregory Hampson, and Anthony J Marchese. End-gas autoignition fraction and flame propagation rate in laser-ignited primary reference fuel mixtures at elevated temperature and pressure. *Combustion and Flame*, 234:111661, 2021.

[87] Scott Bayliff, Bret Windom, Anthony Marchese, Greg Hampson, Jeffrey Carlson, Domenico Chiera, and Daniel Olsen. Controlled end gas auto ignition with exhaust gas recirculation

on a stoichiometric, spark ignited, natural gas engine. In *Internal Combustion Engine Division Fall Technical Conference*, volume 84034, page V001T03A011. American Society of Mechanical Engineers, 2020.

[88] MD Checkel and JD Dale. Computerized knock detection from engine pressure records. *SAE transactions*, pages 221–231, 1986.

[89] Daniel M Wise, Daniel B Olsen, and Myoungjin Kim. Characterization of methane number for producer gas blends. In *Internal Combustion Engine Division Fall Technical Conference*, volume 56109, page V002T02A015. American Society of Mechanical Engineers, 2013.

[90] Seungmok Choi, Christopher P Kolodziej, Alexander Hoth, and Thomas Wallner. Development and validation of a three pressure analysis (tpa) gt-power model of the cfr f1/f2 engine for estimating cylinder conditions. Technical report, SAE Technical Paper, 2018.

[91] Kai J Morganti. *A study of the knock limits of liquefied petroleum gas (LPG) in spark-ignition engines*. PhD thesis, The University of Melbourne, 2013.

[92] Gerhard Woschni. A universally applicable equation for the instantaneous heat transfer coefficient in the internal combustion engine. Technical report, SAE Technical paper, 1967.

[93] Shawn D Givler, Mandhapati Raju, Eric Pomraning, PK Senecal, Nameer Salman, and Ronald Reese. Gasoline combustion modeling of direct and port-fuel injected engines using a reduced chemical mechanism. Technical report, SAE Technical Paper, 2013.

[94] Riccardo Scarcelli, Keith Richards, Eric Pomraning, Peter K Senecal, James M Sevik, and Thomas Wallner. Cycle-to-cycle variations in multi-cycle engine rans simulations. Technical report, Argonne National Lab.(ANL), Argonne, IL (United States), 2016.

[95] Anthony A Amsden, Peter J O'Rourke, and T Daniel Butler. Kiva-ii: A computer program for chemically reactive flows with sprays. Technical report, Los Alamos National Lab.(LANL), Los Alamos, NM (United States), 1989.

[96] Chong-Wen Zhou, Yang Li, Ultan Burke, Colin Banyon, Kieran P Somers, Shuiting Ding, Saadat Khan, Joshua W Hargis, Travis Sikes, Olivier Mathieu, et al. An experimental and chemical kinetic modeling study of 1, 3-butadiene combustion: Ignition delay time and laminar flame speed measurements. *Combustion and Flame*, 197:423–438, 2018.

[97] Rg G Abdel-Gayed and D Bradley. A two-eddy theory of premixed turbulent flame propagation. *Philosophical transactions of the royal society of London. Series A, Mathematical and physical sciences*, 301(1457):1–25, 1981.

[98] Amrit B Sahu, A Abd El-Sabor Mohamed, Snehasish Panigrahy, Chiara Saggese, Vaibhav Patel, Gilles Bourque, William J Pitz, and Henry J Curran. An experimental and kinetic modeling study of nox sensitization on methane autoignition and oxidation. *Combustion and Flame*, 238:111746, 2022.

[99] Philippe Dagaut and Guillaume Dayma. The high-pressure reduction of nitric oxide by a natural gas blend. *Combustion and flame*, 143(1-2):135–137, 2005.

[100] Yingtao Wu, Snehasish Panigrahy, Amrit B Sahu, Chaimae Bariki, Joachim Beeckmann, Jinhu Liang, Ahmed AE Mohamed, Shijun Dong, Chenglong Tang, Heinz Pitsch, et al. Understanding the antagonistic effect of methanol as a component in surrogate fuel models: A case study of methanol/n-heptane mixtures. *Combustion and Flame*, 226:229–242, 2021.

[101] Ajoy Ramalingam, Snehasish Panigrahy, Yann Fenard, Henry Curran, and Karl Alexander Heufer. A chemical kinetic perspective on the low-temperature oxidation of propane/propene mixtures through experiments and kinetic analyses. *Combustion and Flame*, 223:361–375, 2021.

[102] Mohammadreza Baigmohammadi, Vaibhav Patel, Shashank Nagaraja, Ajoy Ramalingam, Sergio Martinez, Snehasish Panigrahy, Ahmed Abd El-Sabor Mohamed, Kieran P Somers, Ultan Burke, Karl A Heufer, et al. Comprehensive experimental and simulation study of the ignition delay time characteristics of binary blended methane, ethane, and ethylene over

a wide range of temperature, pressure, equivalence ratio, and dilution. *Energy & Fuels*, 34(7):8808–8823, 2020.

[103] Shashank S Nagaraja, Jinhu Liang, Shijun Dong, Snehasish Panigrahy, Amrit Sahu, Goutham Kukkadapu, Scott W Wagnon, William J Pitz, and Henry J Curran. A hierarchical single-pulse shock tube pyrolysis study of c2–c6 1-alkenes. *Combustion and Flame*, 219:456–466, 2020.

[104] Snehasish Panigrahy, Jinhu Liang, Shashank S Nagaraja, Zhaohong Zuo, Gihun Kim, Shijun Dong, Goutham Kukkadapu, William J Pitz, Subith S Vasu, and Henry J Curran. A comprehensive experimental and improved kinetic modeling study on the pyrolysis and oxidation of propyne. *Proceedings of the Combustion Institute*, 38(1):479–488, 2021.

[105] A Abd El-Sabor Mohamed, Snehasish Panigrahy, Amrit Bikram Sahu, Gilles Bourque, and Henry J Curran. An experimental and kinetic modeling study of the auto-ignition of natural gas blends containing c1–c7 alkanes. *Proceedings of the Combustion Institute*, 38(1):365–373, 2021.

[106] Shashank S Nagaraja, Jennifer Power, Goutham Kukkadapu, Shijun Dong, Scott W Wagnon, William J Pitz, and Henry J Curran. A single pulse shock tube study of pentene isomer pyrolysis. *Proceedings of the Combustion Institute*, 38(1):881–889, 2021.

[107] Shijun Dong, Kuiwen Zhang, Peter K Senecal, Goutham Kukkadapu, Scott W Wagnon, Stephen Barrett, Nitin Lokachari, Snehasish Panigaphy, William J Pitz, and Henry J Curran. A comparative reactivity study of 1-alkene fuels from ethylene to 1-heptene. *Proceedings of the Combustion Institute*, 38(1):611–619, 2021.

[108] Haoran Hu and James Keck. Autoignition of adiabatically compressed combustible gas mixtures. *SAE transactions*, pages 592–604, 1987.

[109] Chih-Jen Sung and Henry J Curran. Using rapid compression machines for chemical kinetics studies. *Progress in Energy and Combustion Science*, 44:1–18, 2014.

[110] Inc. Ansys. Chemkin pro 2018, 2018.

Appendix A

A total of 12 different piston designs have been simulated with varying degrees of compression ratios (CR), squish areas, and piston crown designs to induce swirl, tumble, and squish flows. Figure A.1 shows the 12 piston designs simulated.

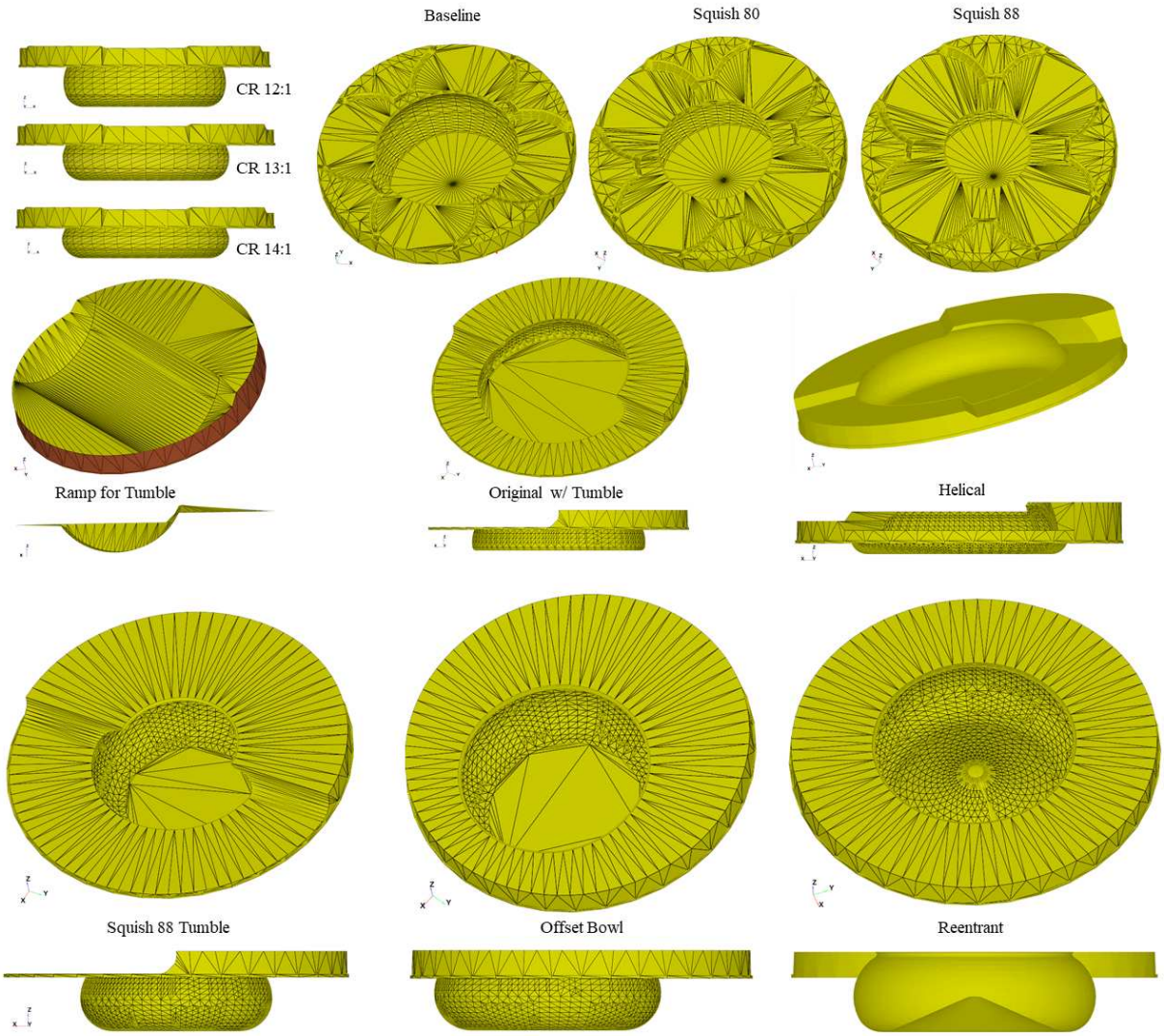

Figure A.1: Piston designs used in the simulations to improve ITE.

To analyze the influence of each design on ITE, simulations were run at two distinct conditions: constant CA50 and at the Knock Limited Spark Advance (KLSA). Simulations at constant CA50

allow the analysis of how a piston design performs at the same combustion phasing, however, various designs underwent EGAI under this condition, blurring the analysis of their influence on ITE. Thus, KLSA conditions were simulated to assess which design can offer the largest gain in ITE while still maintaining an EGAI-free operation. The influence of TKE, swirl, and tumble about the X- and Y-axis on ITE was then assessed as well as how each design increased/decreased heat losses. Figure A.2 shows a schematic of the Cummins SCE firing cylinder and the axes of rotation considered in this study. Lastly, a Linear Regression Analysis was performed to understand which of the parameters is the most influential in enhancing ITE, ignition delay (ST-CA10), burn duration (CA10-CA90), and heat flux.

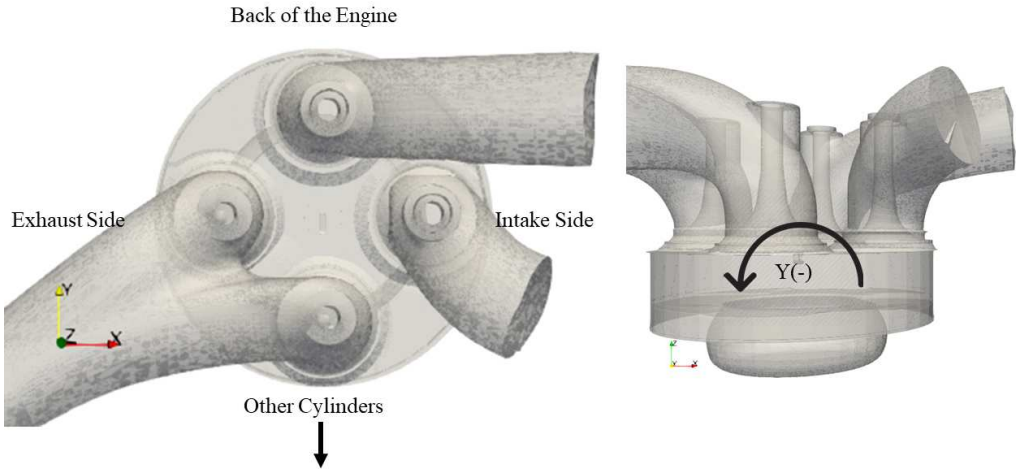

Figure A.2: CFD axis schematic of the SCE CFD model.

A.1 Results and Discussion

Starting from the simulation results for the constant CA50 condition, Figure A.3 shows a similar trend to that observed in the CFR engine testing and modeling, where EGAI can increase ITE. This is noticeable by looking at the cases with increased ITE relative to the baseline piston design, where 6 out 8 designs with increased ITE experienced EGAI. However, for Squish 80 and Squish 88 designs, even the presence of EGAI was not sufficient to increase ITE, but rather, these designs resulted in a decreased ITE.

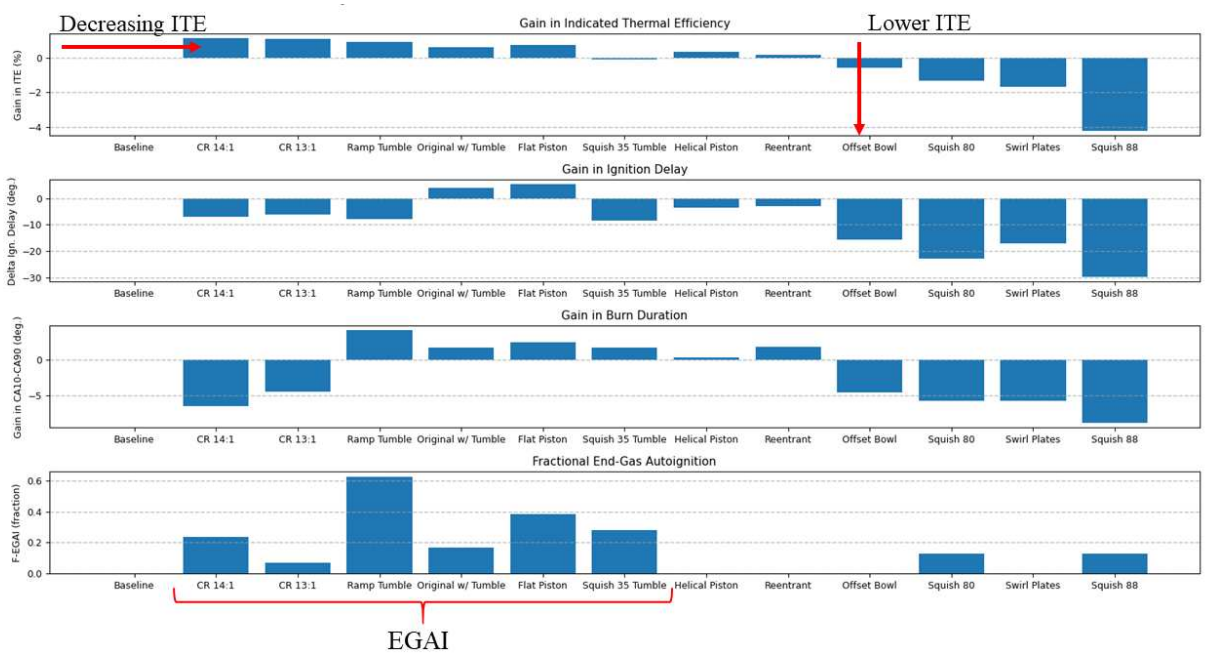

Figure A.3: Effects of Piston Designs on ITE: Constant CA50. EGAI is increasing ITE.

The probable reason for the decreased ITE despite the presence of EGAI is the increased heat losses. Figure A.4 shows the ITE versus Heat Flux (left) and ITE versus Piston Surface Area (right). From this figure, it is clear that heat flux and piston surface area have a strong influence on ITE, where all cases with higher heat fluxes and surface areas than the baseline design experience a decrease ITE. The same trend was observed in the KLSA conditions.

The same strong influence was not observed when looking at the flow variables from the KLSA condition. Figure A.5 shows plots of ITE versus TKE, swirl ratio, tumble ratio about the X-axis, and tumble ratio about the Y-axis. As can be seen, except for the tumble ratio about the Y-axis, it is not possible to draw a clear trend. However, for the tumble ratio about the Y-axis, it seems that more negative ratios, i.e. flow towards the exhaust side or counterclockwise flow in Figure A.2 right, benefit ITE. Although a clear trend was not possible to be drawn for the swirl ratio, it seems that increasing it leads to decreased ITE. Therefore, there might be a competition between flow velocities, that increase swirl and tumble ratios and, thus, burn rates, and heat fluxes, which result in increased heat losses. Figure A.6 shows two plots of these two competing effects due to increased flow velocities. As can be seen in Figure A.6 left, steadily decreasing burn duration causes a steady

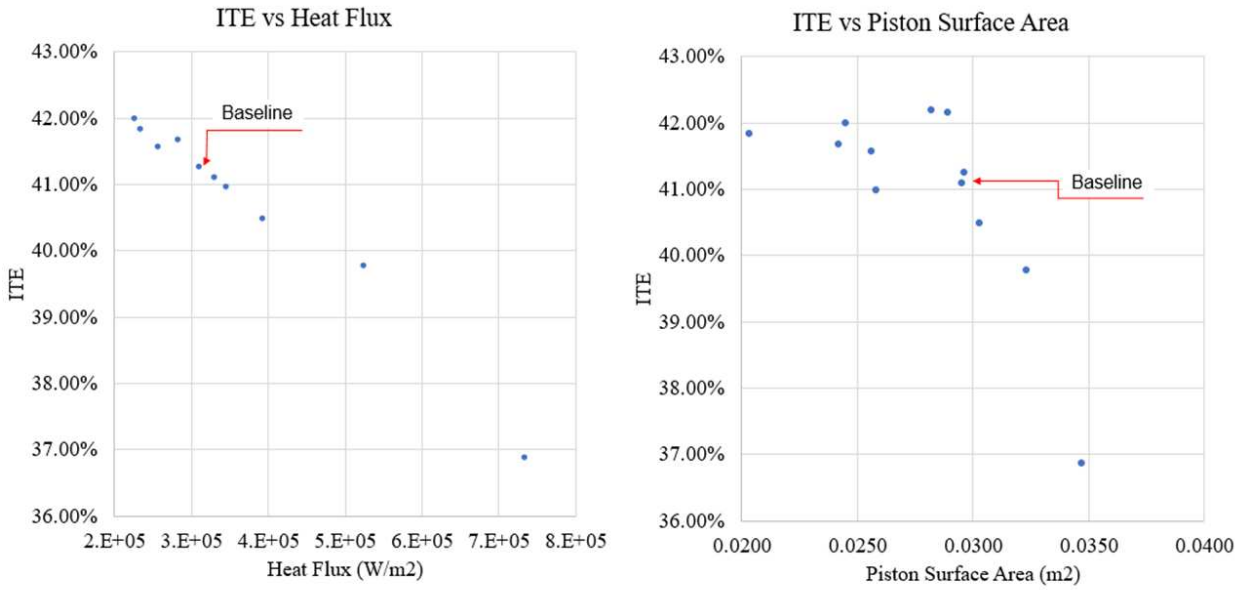

Figure A.4: ITE versus Heat Flux (left) and Piston Surface Area (right). Heat Fluxes and Surface Areas have a strong influence on ITE.

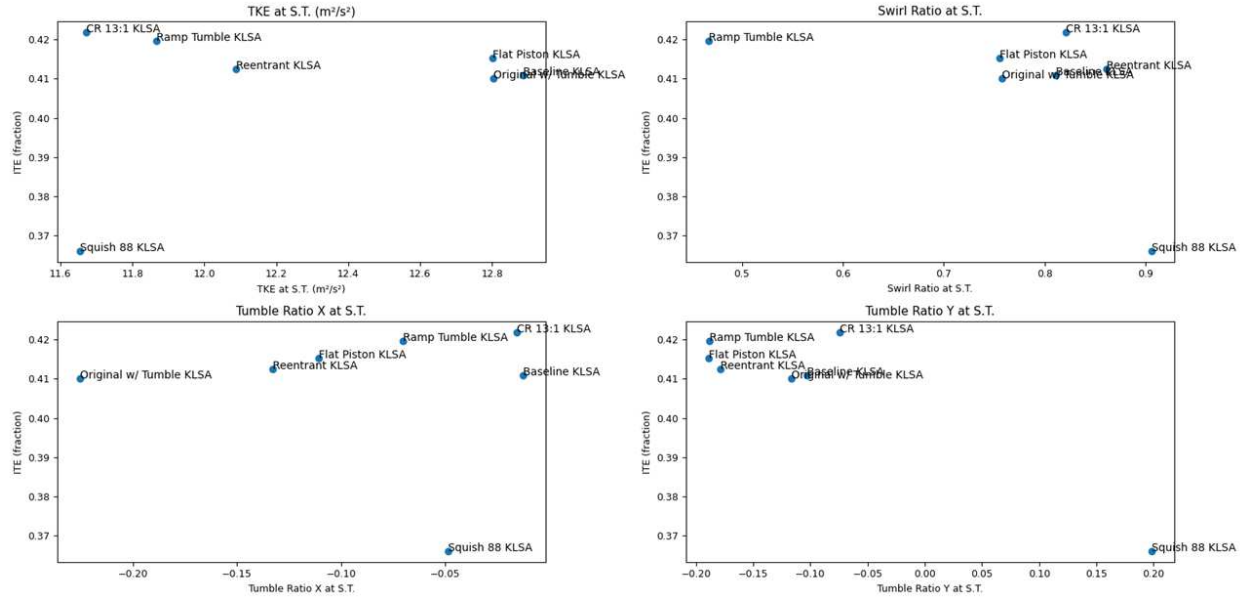

Figure A.5: Flow parameters effect on ITE. Tumble Ratio about the Y-axis shows the clearest correlation with ITE.

increase in heat flux. Similarly, steadily decreasing burn duration causes a steady increase in ITE up to a maximum, where ITE steeply falls, which coincides with the point where heat flux steeply increases.

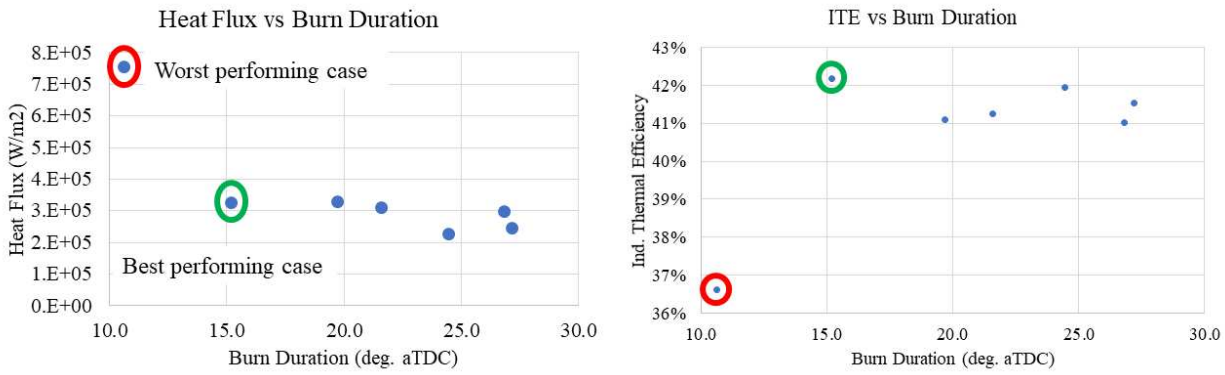

Figure A.6: Steadily decreasing burn duration due to increasing flow velocities increases ITE up to a maximum where heat losses are exacerbated.

Lastly, the Linear Regression Analysis reveals that the single most influential parameter on the ITE is the tumble ratio about the Y-axis, followed by the piston surface area (Table A.1). The likely reason for the tumble about the Y-axis being the most influential parameter is again how it correlates to heat transfer, as shown in Table A.2. Physically, increasing tumble in the negative Y direction forces the flame to initially develop closer to the exhaust side, where wall temperatures are high, decreasing the temperature gradient between the wall and the gas and, thus, decreasing heat fluxes. Additionally, the tumble ratio about the Y-axis is also the single most influential parameter affecting ignition delay and burn duration, as shown in Tables A.3 and A.4.

These preliminary results show that, in order to increase ITE, a piston needs to be designed for the shortest burn duration possible while still maintaining lower or equal heat fluxes and surface area. In order to achieve this, the in-cylinder flow has to be initially directed towards the exhaust side to lower the temperature gradient between the walls and gas, decreasing, therefore, heat fluxes. These results corroborate with Nagao's [74] observations where increased swirl ratio increases ITE up to a maximum, exacerbating heat losses beyond that point.

Table A.1: Influence of Flow and Piston Design Parameters on ITE.

Parameters	R^2
Tumble Ratio Y	0.837
Piston Surface Area	0.451
Surface to Volume Ratio at TDC (SVR)	0.419
Swirl Ratio	0.245
Turbulent Kinetic Energy (TKE)	0.088
Tumble Ratio X	0.011

Table A.2: Influence of Flow and Piston Design Parameters on Heat Flux.

Parameters	R^2
Tumble Ratio Y	0.955
Max Velocity at ST	0.922
Piston Surface Area	0.630
Surface to Volume Ratio at TDC (SVR)	0.572
Swirl Ratio	0.331
Turbulent Kinetic Energy (TKE)	0.204

Table A.3: Influence of Flow and Piston Design Parameters on Ignition Delay.

Parameters	R^2
Tumble Ratio Y	0.688
TKE	0.631
Tumble Ratio X	0.248
Swirl Ratio	0.028

Table A.4: Influence of Flow and Piston Design Parameters on Burn Duration.

Parameters	R^2
Tumble Ratio Y	0.708
TKE	0.455
Tumble Ratio X	0.433
Swirl Ratio	0.305